Since 1955

Strojniški vestnik
Journal of Mechanical Engineering

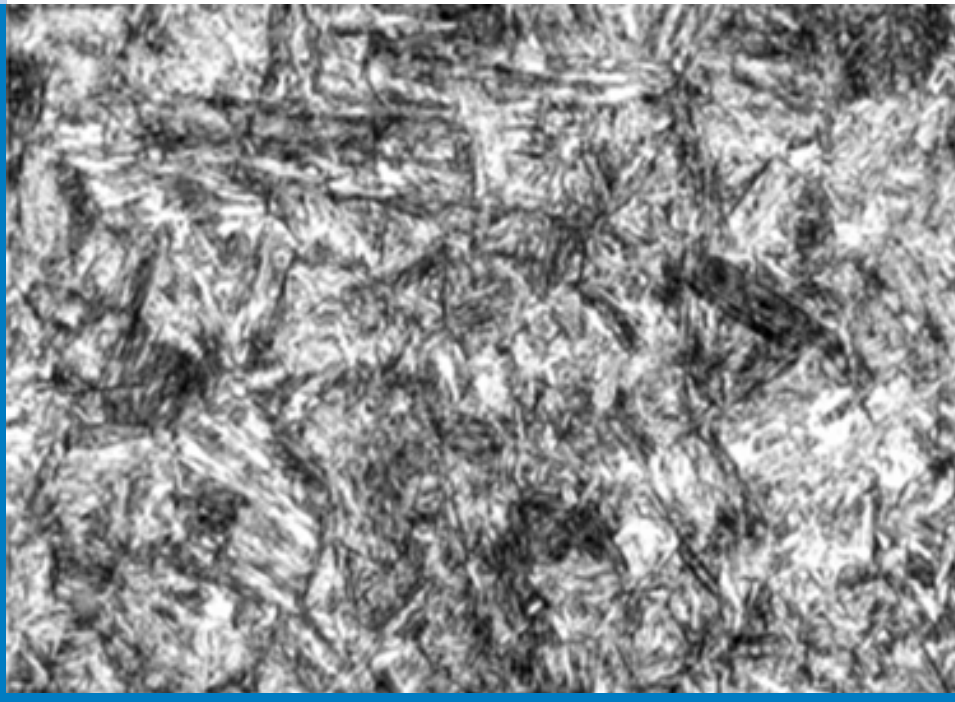

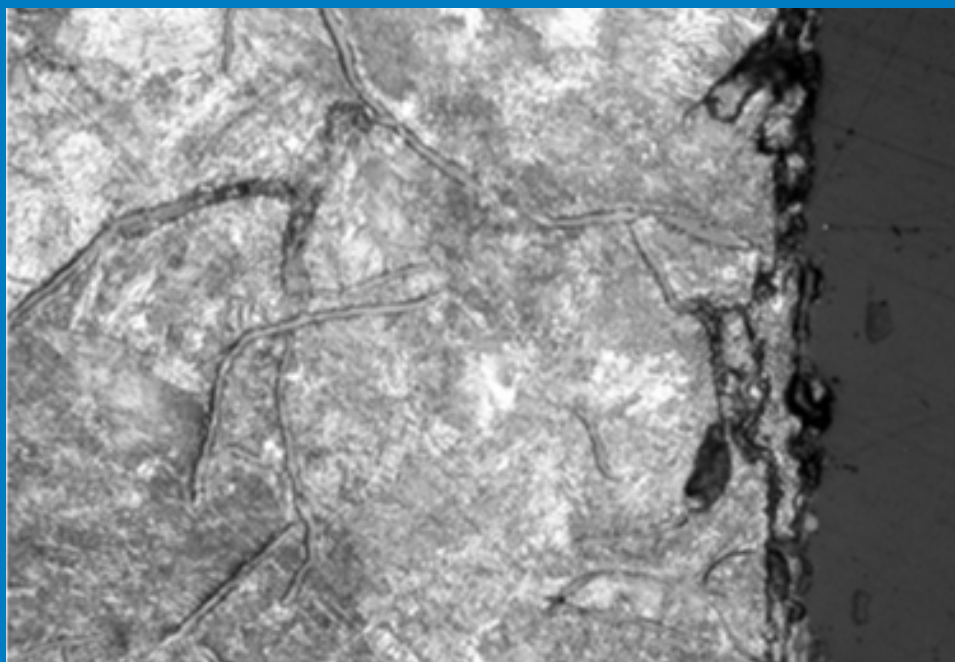

no. 3
year 2019
volume 65

Strojniški vestnik – Journal of Mechanical Engineering (SV-JME)

Aim and Scope
The international journal publishes original and (mini)review articles covering the concepts of materials science, mechanics, kinematics, thermodynamics, energy and environment, mechatronics and robotics, fluid mechanics, tribology, cybernetics, industrial engineering and structural analysis.
The journal follows new trends and progress proven practice in the mechanical engineering and also in the closely related sciences as are electrical, civil and process engineering, medicine, microbiology, ecology, agriculture, transport systems, aviation, and others, thus creating a unique forum for interdisciplinary or multidisciplinary dialogue.
The international conferences selected papers are welcome for publishing as a special issue of SV-JME with invited co-editor(s).

Editorial Office
University of Ljubljana, Faculty of Mechanical Engineering
SV-JME, Aškerčeva 6, SI-1000 Ljubljana, Slovenia
Phone: 386 (0)1 4771 137
Fax: 386 (0)1 2518 567
info@sv-jme.eu, http://www.sv-jme.eu

Print: Papirografika, printed in 300 copies

Founders and Publishers
University of Ljubljana, Faculty of Mechanical Engineering, Slovenia
University of Maribor, Faculty of Mechanical Engineering, Slovenia
Association of Mechanical Engineers of Slovenia
Chamber of Commerce and Industry of Slovenia, Metal Processing Industry Association

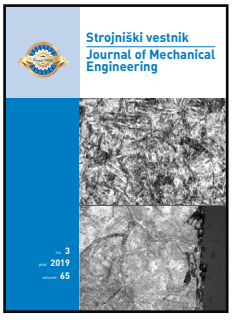

Cover:
The microstructure of the hydraulic control valve components: valve spool – made of steel with martensite microstructure and average surface hardness 927 HV; and valve body – made of grey cast iron with perlite microstructure and average surface hardness 244 BHN.

Image courtesy:
Velibor Karanović and University of Novi Sad.

General information
Strojniški vestnik – Journal of Mechanical Engineering is published in 11 issues per year (July and August is a double issue).

Institutional prices include print & online access: institutional subscription price and foreign subscription €100,00 (the price of a single issue is €10,00); general public subscription and student subscription €50,00 (the price of a single issue is €5,00). Prices are exclusive of tax. Delivery is included in the price. The recipient is responsible for paying any import duties or taxes. Legal title passes to the customer on dispatch by our distributor. Single issues from current and recent volumes are available at the current single-issue price. To order the journal, please complete the form on our website. For submissions, subscriptions and all other information please visit: *http://www.sv-jme.eu.*

You can advertise on the inner and outer side of the back cover of the journal. The authors of the published papers are invited to send photos or pictures with short explanation for cover content.

We would like to thank the reviewers who have taken part in the peer-review process.

ISSN 0039-2480, ISSN 2536-2948 (online)

The journal is subsidized by Slovenian Research Agency.

Strojniški vestnik - Journal of Mechanical Engineering is available on *https://www.sv-jme.eu*.

Contents

Strojniški vestnik - Journal of Mechanical Engineering
volume 65, (2019), number 3
Ljubljana, March 2019
ISSN 0039-2480

Published monthly

Papers

Strojniški vestnik - Journal of Mechanical Engineering 65(2019)3, 139-147

DOI:10.5545/sv-jme.2018.5856 Original Scientific Paper
Received for review: 2018-11-14
Received revised form: 2019-01-23
Accepted for publication: 2019-02-22

Impact of Contaminated Fluid on the Working Performances of Hydraulic Directional Control Valves

Velibor Karanović[1,*] – Mitar Jocanović[1] – Sebastian Baloš[1] – Darko Knežević[2] – Ivan Mačužić[3]
[1]University of Novi Sad, Faculty of Technical Sciences, Serbia
[2]University of Banja Luka, Faculty of Mechanical Engineering, Bosnia and Herzegovina
[3]University of Kragujevac, Faculty of Engineering, Serbia

The study aims to investigate the impact of solid particles on the directional hydraulic valve operation. Experiments have been performed for a certain number of operating cycles to measure the impact of the working fluid cleanliness level on the intensity of the wear on contact surfaces as well as on other failures in the operation of the directional control valve. For experimental purposes, a mechanically actuated control valve 4/2 is used. The wear intensity of working elements was determined for different levels of oil contamination by solid particles. Also, experimental results have shown that there are differences between theoretically calculated and the measured flow through the radial clearance. By measuring pressure drop values during the fluid flow through the valve, it was found that oils with the lowest cleanliness level have a greater dispersion of the measured values. The results will contribute to better understanding the impact of working fluid cleanliness on possible defects and failures happening inside hydraulic system components.
Keywords: hydraulic systems, condition monitoring, tribology, wear

Highlights
- *Hydraulic fluid contamination influence on directional valve performances has been experimentally investigated.*
- *System pressure, flow, and temperature are controlled within tolerated limits, and the solid particle contamination level is varied.*
- *Experimental measurements involve pressure drop across the valve, radial clearance between the piston and housing, and contaminated fluid flow through the clearance.*
- *Oil with higher contamination level increases the wear intensity, decreases measurement precision of pressure drop values, and slightly decreases leakage across clearances.*

0 INTRODUCTION

It is very difficult to predict and precisely determine the impact of fluid cleanliness on the system operation or its components, due to many factors and a variety of hydraulic system applications. The hydraulic fluid contamination is an issue that can shorten the working life of hydraulic components, which has a direct impact on maintenance costs **[1]** to **[3]**. Also, contamination can be considered as a hydraulic system "intruder", which has a direct or indirect influence on system behaviour and parameters such as precision, response time, repeatability, controllability, etc. **[4]** and **[5]**.

Many well-regarded companies and other institutions dealing with manufacturing, maintenance and testing of hydraulic systems and equipment, based on their own experience from practice and experimental research, claim that the working fluid contamination represents the main cause of failures in 70 % to 80 % cases **[2]** and **[6]** to **[9]**. Additionally, the requirements for more precise control and higher efficiency of hydraulic systems, have resulted in the decreased clearances between working elements of hydraulic components and the increased working pressure values **[10]**. Due to the decreased clearance size, the adverse impact of micron-size solid contaminants becomes evident. Although it is well-known that solid contaminants are destructive to hydraulic system components, as well as to the working fluid itself, there was no internationally accepted method for objectively determination of contamination tolerance for systems or each component separately **[11]**, until 2017. In 2013, was initiated and consequently published ISO 12669:2017 standard, developed for determining the required cleanliness level (RCL) for a system **[12]**. This standard is now under review for five years period.

Due to the lack of a standard procedure, the RCL choice is based on the system designer experience or on the third person recommendation (such as components manufacturer) and his experience. This doesn't mean that optimal cleanliness level was selected for the specific system operation.

The RCL selection by this method is strongly subjective, for which reason it does not provide consistency. Consequently, many system designers, as well as the users of hydraulic systems, are unsure and confused about the appropriate cleanliness level

*Corr. Author's Address: University of Novi Sad, Faculty of Technical Sciences, Trg Dositeja Obradovica 6, 21000 Novi Sad, Serbia, velja_82@uns.ac.rs

selection for a specific hydraulic system. Often, stricter requirements are applied regarding the working fluid cleanliness level, which produces a positive impact on the working life of the equipment but also a negative impact in terms of the increased maintenance costs (Fig. 1).

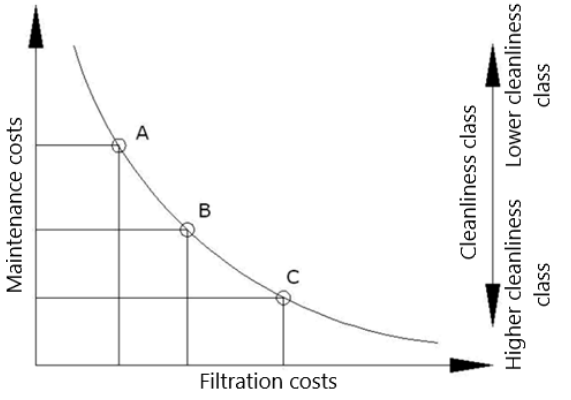

Fig. 1. *Maintenance costs in relation to filtration costs depending on mineral oil cleanliness level (maintenance costs/filtration costs), in relation to the required oil cleanliness: A – low cleanliness of oil/low filtration costs/high maintenance costs; B – optimal cleanliness of oil/optimal filtration and maintenance costs; C – high cleanliness of oil/high filtration costs/ low maintenance costs*

This study presents the research results regarding the impact of solid particles in oil on the wear intensity of contact surfaces of working elements in a hydraulic directional control valve, as well as on the leakage through clearances dependent on cleanliness levels of hydraulic oil.

1 EXPERIMENTAL

1.1 Experimental Installation

For the experiment, an installation according to the schematic shown in Fig. 2 was used.

As an object of experimental measurement, a mechanically actuated directional control valve 4/2 is used within the installation. It has l = 4 mm axial working stroke, flow rate Q = 20 l/min and maximum working pressure p = 320 bar.

1.2 Measuring Instrumentation Used for Annular Gap Monitoring and Starting Values

Measurement of the contact rings' diameters on the piston and in the valve body/housing was performed with a Carl Zeiss Contura G2 coordinate measuring

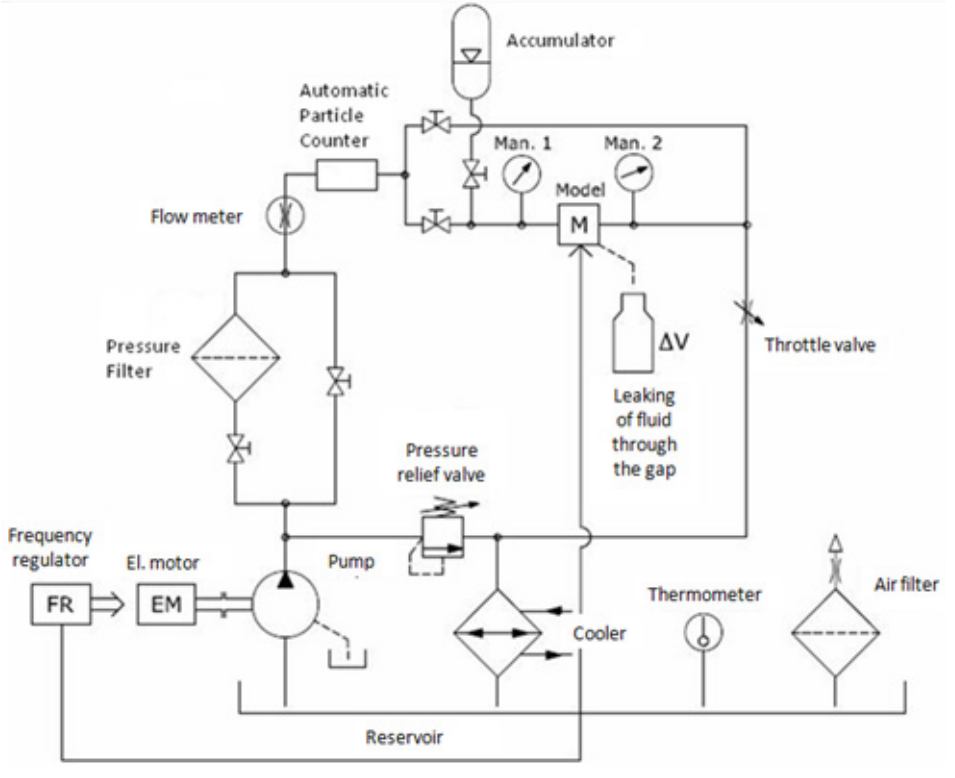

Fig. 2. *Scheme of the experimental installation*

machine. Fig. 3 shows a cross-section of the directional control valve with indicated piston contact rings and cylinders within the valve body, which form the radial clearances observed in the experiment. The measurement results of piston contact ring diameters and cylinders within the valve body show that the original clearance values in the tested directional control valves are within tolerances for standard directional control valves. Table 1 shows the measured original radial clearance values for all three tested valves used in the experiment.

The following formula determines clearance values:

$$Z_i = \frac{D_i - d_i}{2}, \tag{1}$$

where Z_i stands for clearance value, D_i the value of cylinder diameter in the valve body and d_i the value of piston ring diameter.

Table 1. *Starting values of the radial clearance between the piston and the valve body*

Valve	Z_1 [μm]	Z_2 [μm]	Z_2 [μm]	Z_2 [μm]
RV1	8.30	5.95	5.05	5.90
RV2	6.15	4.95	5.40	5.45
RV3	6.05	6.45	5.90	5.30

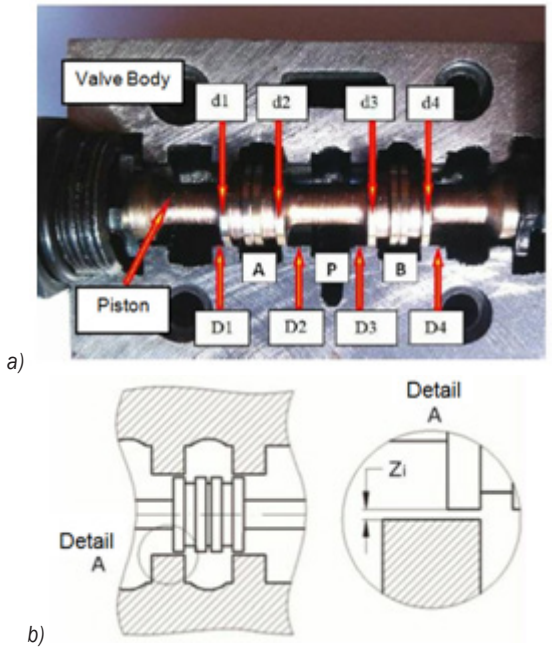

Fig. 3. *A cross-sectional view of the tested directional control valve; a) Integral valve elements and diameters of the rings being monitored, and b) The surfaces in relation to which the radial gap is obtained by measuring*

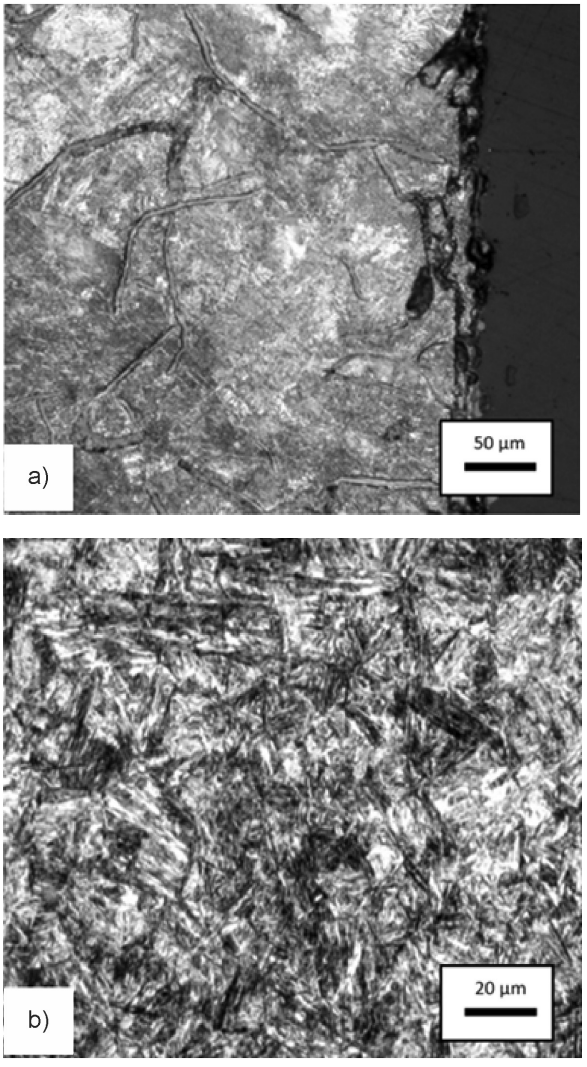

Fig. 4. *The microstructure of the contact surface in the valve body and piston: a) pearlite microstructure (at 200× magnification) near the contact surface in the valve body; b) martensite microstructure (at 500× magnification) of the piston*

The valve bodies are made of grey cast iron with pearlite matrix (Fig. 4a). The contact surface hardness, measured with *Wolpert DIA Testor Z Brinell*, is in the range of 240 BHN to 248 BHN. The piston, made of martensitic stainless steel (Fig. 4b) is surface-hardened to approximately 0.3 mm depth, with the average surface hardness 927 HV.

The directional control valve, used in the experimental installation, has two working positions:

1. Neutral position (with closed flow paths);
2. Working position (fluid flow through the valve is enabled, from connection P towards connection A).

1.3 Measuring Instrumentation for Oil Cleanliness

For experimental purposes, mineral hydraulic oil HM 46 was used. Each valve has its specified oil cleanliness level (Table 2).

Table 2. *Hydraulic oil cleanliness level for the experiment*

Valve	Cleanliness level of oil for particles $\geq 4\mu m_{(c)}$ according to ISO 4406:2017 [13]
RV1	22
RV2	21
RV3	20

The oil contamination level during the operation was monitored with HIAC PM 4000 and maintained on the preset level. When particle concentration increases in relation to the preset level, the fluid filtrate through an installed pressure filter (HYDAC Betamicron) of absolute filtration fineness, with beta ratio $\beta_5 = 200$.

1.4 Measuring Instrumentation for Pressure and Temperature Monitoring

The pressure and temperature monitoring were performed with hand-held datalogger Hydrotechnik Multi-Handy 3010, pressure sensor - measuring range from 0 bar to 400 bar (±0.5 % of final value) and temperature sensor - measuring range from –50 °C to 200 °C (with the error limit < ±0.1 % of final value).

1.5 Instrumentation for Spool Surface Scanning

In addition to the above-mentioned measurements, contact surfaces of piston rings were examined by using a JEOL JSM 6460LV microscope.

1.6 Experiment Working Parameters' Setup Values

The experiment was conceived as the testing of three new directional control valves produced by the same manufacturer and of the same operating characteristics. During the experiment, installation worked with pressure p = 150 bar, flow Q = 9.5 l/min and temperature T = 45 °C. All three valves were monitored up to $n = 10^6$ working cycles.

During the operation of the system, the parameters such as pressure, flow, temperature and hydraulic oil cleanliness were monitored and maintained. The gap size between contact surfaces of piston rings and cylinders in the valve body was also monitored, as well as the changes of the fluid leakage through the clearance, weight change of the piston and the valve body due to wear, and changes of pressure drop values during the fluid flow through the open valve.

2 RESULTS AND DISCUSSION

Indicators that show the wear intensity of the valve contact pairs are the radial clearances values and the values of the fluid flow volume through the clearances. Tables 3 to 5 show the measured values of radial clearances between the contact surfaces of the

Table 3. *Values of the radial clearance between the piston and the cylinder in the valve body RV1 (used oil cleanliness level ISO 22* [13] *for particles ≥ 4 μm$_{(c)}$)*

Valve	Radial clear. [μm]	Number of working cycles											
		0	10^5	$2{\cdot}10^5$	$3{\cdot}10^5$	$4{\cdot}10^5$	$5{\cdot}10^5$	$6{\cdot}10^5$	$7{\cdot}10^5$	$8{\cdot}10^5$	$9{\cdot}10^5$	10^6	$K_{(Zi)}$
RV1	Z_1	8.30	8.50	10.40	10.80	11.90	13.90	16.15	17.55	18.50	19.95	22.35	2.69
	Z_2	5.95	6.10	7.50	8.20	9.80	14.00	19.15	19.70	25.80	31.05	32.50	5.46
	Z_3	5.05	5.10	5.10	5.50	6.10	6.50	6.70	6.75	6.85	7.45	7.60	1.51
	Z_4	5.90	6.05	6.55	6.85	6.90	7.00	7.05	7.30	7.55	7.70	7.70	1.31

Table 4. *Values of the radial clearance between the piston and the cylinder in the valve body RV2 (used oil cleanliness level ISO 21* [13] *for particles ≥ 4 μm$_{(c)}$)*

Valve	Radial clear. [μm]	Number of working cycles											
		0	10^5	$2{\cdot}10^5$	$3{\cdot}10^5$	$4{\cdot}10^5$	$5{\cdot}10^5$	$6{\cdot}10^5$	$7{\cdot}10^5$	$8{\cdot}10^5$	$9{\cdot}10^5$	10^6	$K_{(Zi)}$
RV2	Z_1	6.15	6.70	7.25	7.75	7.95	8.40	10.45	10.90	11.40	12.05	12.05	1.96
	Z_2	4.95	5.20	5.25	5.70	7.45	7.85	9.15	9.30	10.00	10.15	11.00	2.22
	Z_3	5.40	5.50	5.85	6.05	6.05	6.35	6.55	6.80	7.15	7.30	7.45	1.38
	Z_4	5.45	5.45	5.65	6.05	6.15	6.25	6.40	6.45	6.50	6.65	6.85	1.25

Table 5. *Values of the radial clearance between the piston and the cylinder in the valve body RV3 (used oil cleanliness level ISO 20* **[13]** *for particles ≥ 4 μm$_{(c)}$)*

Valve	Radial clear. [μm]	Number of working cycles											
		0	10^5	$2{\cdot}10^5$	$3{\cdot}10^5$	$4{\cdot}10^5$	$5{\cdot}10^5$	$6{\cdot}10^5$	$7{\cdot}10^5$	$8{\cdot}10^5$	$9{\cdot}10^5$	10^6	$K_{(Zi)}$
RV3	Z_1	6.05	6.10	6.15	6.40	6.60	6.80	6.90	7.00	7.25	7.30	7.70	1.27
	Z_2	6.40	6.45	7.75	8.75	8.85	8.90	9.10	9.20	9.50	10.55	11.00	1.72
	Z_3	5.75	5.90	6.10	6.15	6.30	6.60	6.75	6.90	6.95	7.30	7.55	1.31
	Z_4	5.30	5.55	5.60	5.65	5.95	6.05	6.05	6.15	6.20	6.35	6.50	1.23

piston and body of the valve. The intensity of wear is interpreted with the value of the coefficient $K_{(Zi)}$, which is determined as follows:

$$K_{(Zi)} = \frac{x_{10^6}}{x_0}, \tag{2}$$

$x_{10}{}^6$ stands for the value of radial clearance after 10^6 working cycles; x_0 the start value of the radial clearance, *Zi* the radial clearance being monitored for the specific valve.

Based on the coefficient $K_{(Zi)}$ from Tables 3 to 5, it can be noticed that the wear intensity is drastically decreased with the increase of oil cleanliness. The largest values of the coefficient $K_{(Zi)}$ were obtained for the radial clearance Z_2 with all three tested valves. Regarding that at the time of switching of the valve into operating position, the piston ring, and cylinder, which form the clearance Z_2, were at the front of the fluid stream impact. Intensive wearing in this section was expected, but the intensity of the clearance change could not be anticipated.

Turbulent movement of the fluid carrying solid particles produces an aggressive impact on the edges of the piston ring, and on the rim surfaces that provide non-contact sealing. The longitudinal scratches over the piston rings' contact surfaces, which are in Fig. 5, indicate the presence of high abrasive wear. At the front side of the piston, in Fig. 5c, some parts of the frontal surface have been broken off, which points to another wear mechanism, i.e. erosion combined with fatigue.

The wear process, as a process that by definition represents a progressive removing of material from the contact surfaces which are mutually sliding one against another **[14]**, in this case gradually causes an increase in the size of radial clearance, resulting in the increase of volume losses. The volume loss results from the decrease of the actuators' operating speed. In the valve, the losses cause pressure drop increase during the fluid flow through the valve, as well as the fluid temperature increase, which causes viscosity to decrease. The occurrences above decrease the energy efficiency as well as the dynamic performance of the entire system **[15]** and **[16]**.

To graphically present the wear intensity in the performed experiments and define it as a specific mathematical model, the Least Square fitting method and MATLAB software were used. The result of the analysis showed that the second order polynomial function was the most representative for the interpretation of the experimental, numerical data because it had the highest values of determination coefficient and the minimal sum of the squares of residuals. In addition to the polynomial function, other mathematical models were analyzed, with the results shown in Table 6.

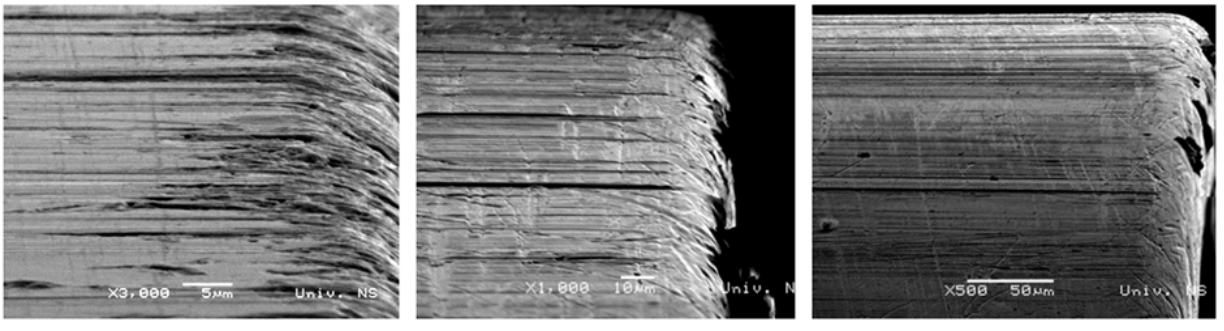

Fig. 5. *SEM images of the damaged piston edge that forms the radial clearance Z2 under various magnitudes*

Table 6. *Determination coefficient values for different functions derived from collected radial clearance data*

Function	Valve RV1	Valve RV2	Valve RV3
	Determination coefficient / Sum of the squares of residuals		
Linear	0.9376 / 61.92	0.9628 / 1.880	0.9067 / 1.962
Second order polynomial	0.9838 / 16.05	0.9629 / 1.876	0.9154 / 1.780
Exponential	0.9753 / 24.50	0.9458 / 2.744	0.8924 / 2.263

The mathematical model of radial clearance change (s) for the RV1 valve, which was operating with ISO 22 oil cleanliness level for particles ≥4 $\mu m_{(c)}$.

$$s_{RV1} = 2.312 \cdot 10^{-11} \cdot n^2 + 5.949 \cdot 10^{-6} \cdot n + 5.273. \quad (3)$$

The n stands for a number of working cycles. The mathematical model of radial clearance change (s) for the RV2 valve, which was operating with ISO 21 oil cleanliness level for particles ≥4 $\mu m_{(c)}$.

$$s_{RV2} = -2.098 \cdot 10^{-13} \cdot n^2 + 6.864 \cdot 10^{-6} \cdot n + 4.459. \quad (4)$$

The mathematical model of radial clearance change (s) for the RV3 valve, which was operating with ISO 20 oil cleanliness level for particles ≥4 $\mu m_{(c)}$.

$$s_{RV3} = -1.457 \cdot 10^{-12} \cdot n^2 + 5.621 \cdot 10^{-6} \cdot n + 6.468. \quad (5)$$

A similar study was conducted by Liu et al. **[17]**, in order to define the valve service life model.

Theoretical capacity in Table 7 has been determined by the calculation formula for flow through the annular clearance **[18]**:

$$\Delta Q_t = \frac{\pi \cdot d \cdot \Delta p \cdot s^3}{12 \cdot \eta \cdot L}, \quad (6)$$

where d stands for piston diameter, Δp pressure drop, s clearance, η dynamic viscosity and L clearance length.

In addition to the clearance size, solid particles contained in the working fluid cause a considerable impact on the size of volume losses. Their impact is opposite to the impact of the clearance size, i.e. if the increase in the clearance size causes the increase in volume losses, the increase in the number of solid particles causes the decrease in volume losses. It occurs because solid particles aggregate at the clearance location, forming in this way deposits that temporarily decrease or obstruct the fluid flow through the clearance. The probability of formation of solid particle deposits is higher in case of static conditions of operation when the piston within the valve does not move **[19]** to **[21]**.

Table 7 shows the values of annular leakage (ΔQ_e), measured after each 10^5 working cycles under static conditions of valve operation (which means that there is no spool position change in axial direction), for all three valves. It should be noted that under static conditions of operation the directional control valve is in the neutral position (Fig. 6). Leakage flow is determined as a captured volume (ΔV [l]) per time unit (t [min]).

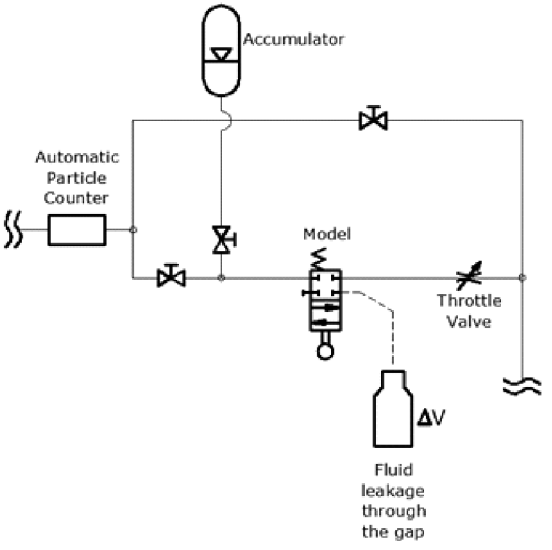

Fig. 6. *Valve position during the measurement of the annular leakage*

Table 8 shows the results of the experimental data set analysis by the least square fitting method. According to the results, the following mathematical models of annular fluid leakage are derived. For the RV1 valve, which was operating with ISO 22, the oil cleanliness level for particles ≥4 $\mu m_{(c)}$.

$$\Delta Q_{RV1} = -2.063 \cdot 10^{-12} \cdot n^2 + 8.054 \cdot 10^{-6} \cdot n + 7.65. \quad (7)$$

The n stands for a number of working cycles. The mathematical model of annular fluid leakage (ΔQ) for the RV2 valve, which was operating with ISO 21 oil cleanliness level for particles ≥4 $\mu m_{(c)}$.

$$\Delta Q_{RV2} = 4.615 \cdot 10^{-13} \cdot n^2 + 4.018 \cdot 10^{-6} \cdot n + 6.942. \quad (8)$$

The mathematical model of annular fluid leakage (ΔQ) for the RV3 valve, which was operating with ISO 20 oil cleanliness level for particles ≥4 $\mu m_{(c)}$.

$$\Delta Q_{RV3} = 7.271 \cdot e^{\left(5.003 \cdot 10^{-7} \cdot n\right)}. \quad (9)$$

Additionally, it should be noted that the formed deposits of solid particles are exposed to a constant impact of pressure that, under certain conditions,

Table 7. *A comparative overview of theoretically calculated (ΔQ_t) and experimentally measured (ΔQ_e) flow values through the annular clearance Z3 in static operating conditions*

Number of working cycles	RV1 (ISO 22 for 4 $\mu m_{(c)}$)			RV2 (ISO 21 for 4 $\mu m_{(c)}$)			RV3 (ISO 20 for 4 $\mu m_{(c)}$)		
	ΔQ_t [ml/min]	ΔQ_e [ml/min]	Δ_{RV1}*	ΔQ_t [ml/min]	ΔQ_e [ml/min]	Δ_{RV2}*	ΔQ_t [ml/min]	ΔQ_e [ml/min]	Δ_{RV3}*
0	10.08	7.10	2.98	12.33	6.40	5.93	14.88	6.80	8.08
10^5	10.38	8.40	1.98	13.02	7.70	5.32	16.08	8.00	8.08
2×10^5	10.38	9.70	0.68	15.67	8.10	7.57	17.77	8.40	9.37
3×10^5	13.02	10.50	2.52	17.34	8.60	8.74	18.21	8.40	9.81
4×10^5	17.77	11.00	6.77	17.34	8.50	8.84	19.57	8.80	10.77
5×10^5	21.50	10.80	10.70	20.04	8.70	11.34	22.51	9.20	13.31
6×10^5	23.54	11.10	12.44	22.00	9.40	12.60	24.08	10.00	14.08
7×10^5	24.08	11.90	12.18	24.61	9.94	14.67	25.72	10.30	15.42
8×10^5	25.16	12.80	12.36	28.61	10.50	18.11	26.28	10.60	15.68
9×10^5	32.37	13.20	19.17	30.45	10.70	19.75	30.45	11.30	19.15
10^6	34.36	14.00	20.36	32.37	11.70	20.67	33.69	12.20	21.49

can break through the barrier, which causes a sudden increase in the fluid flow through the clearance together with the particles **[19]**.

Table 8. *Determination coefficient values for different functions derived from collected annular fluid leakage data*

Function	Valve RV1	Valve RV2	Valve RV3
	Determination coefficient / Sum of the squares of residuals		
Linear	0.9439/2.347	0.9560/1.016	0.9700/0.754
Second order polynomial	0.9526/1.982	0.9568/0.998	0.9733/0.671
Exponential	0.9263/3.084	0.9561/1.014	0.9738/0.660

Table 9. *A comparative display of the mass loss for all three valves*

Valve	Percentage of mass loss	
	Valve body [%]	Piston [%]
RV1	0.0350	0.0031
RV2	0.0066	0.0014
RV3	0.0055	0.0015

Weighing of the valve body and piston mass confirms that both of the components had losses in the mass (Table 9), where the valve body lost more mass in regards to the piston, which fulfils the expectation, taking into account the hardness of the contact surfaces of the valve body and piston.

As the mass loss is very small, this impact on the performances of the directional control valve can be neglected. Nevertheless, it shows how much the valve is worn in terms of mass. However, it should be noted that the removed material from the contact surfaces of working elements produces new particles that are distributed within the fluid through the system and influence other system components' performance with the non-contact sealing mechanism. These particles have significant influence were abrasive, and erosive wear is present.

In order to observe the intensity of disturbances during the oil flow through the open valve due to oil contamination, the pressure drop was measured. In this case, the valve is in working position in order to enable full fluid flow from port P towards port A. The comparative pressure drop diagram in Fig. 6 shows that in all three cases, the pressure drop has a tendency to increase, which decreases with a higher cleanliness level of the working fluid.

By decreasing solid particles' concentration in the working fluid (observed from experiment No. 1 towards experiment No. 3), the intensity of the pressure drop change decreases during the exploitation of the directional control valve. An interesting observation, based on the diagrams from Fig. 7, is a deviation of measured pressure drop values. Diagrams in Fig. 8 interpret experimental results by the normal distribution function, with the purposed of expressing more clearly the differences in terms of deviation of the results around the mean value. Table 10 shows the values of standard deviations for all three valves. These deviations partly represent the result of the pressure sensor measuring uncertainty, but it also is shown that the cleanliness level of working fluid produces an impact on the pressure drop value.

Due to the occurrence of pressure drop, as well as volume losses, the efficiency of hydraulic systems decreases. Less efficient hydraulic systems will have lower competitiveness compared to other drive systems. For this reason, with sophisticated hydraulic

systems, one should pay considerable attention regarding the conditioning of working fluid, which has multiple important effects.

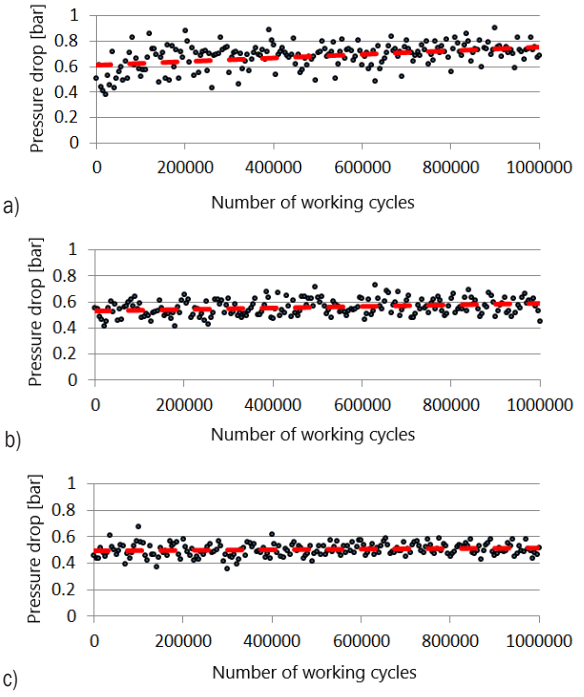

Fig. 7. *Pressure drop diagrams for all three valves: a) for RV1; b) for RV2; c) for RV3, and flow rate Q = 9.5 l/min*

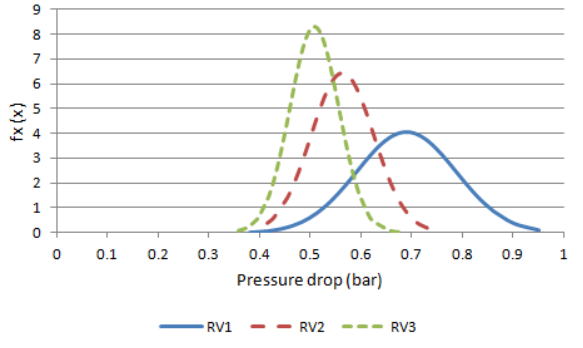

Fig. 8. *Comparison of normal distribution diagrams for pressure drop values*

Table 10. *Pressure drop deviation values for all three valves*

	RV1	RV2	RV3
-	ISO 22 for 4 $\mu m_{(c)}$	ISO 21 for 4 $\mu m_{(c)}$	ISO 20 for 4 $\mu m_{(c)}$
$\sigma = \sqrt{\frac{1}{n}\sum_{i=1}^{n}\left(x_i - \bar{x}\right)^2}$	0.09811	0.06187	0.04790

3 CONCLUSIONS

Based on the experimental results and performed analyses, in this study, it has been confirmed that solid particles produce an impact on working performances of the hydraulic control valve. The particles which come into a clearance intensify the wear process on contact surfaces and the change in their topology, generating new particles, and under certain conditions, they may form deposits resulting in mechanical and flow blockage. Such consequences are particularly present in the components with precise control and regulation elements with non-contact sealing, which are especially sensitive to solid particles' impact due to small clearances.

The obtained experimental results show differences in the wear intensity that were expected. In the case of increased cleanliness level from ISO 22 (for particles ≥4μm $_{(c)}$) to ISO 21 (for particles ≥4 $\mu m_{(c)}$), the achieved decrease of the wear intensity was $K_{Z2(RV1)}/K_{Z2(RV2)}=2.5$ times, and with the decrease from ISO 22 (for particles ≥4 $\mu m_{(c)}$) to ISO 20 (for particles ≥4 $\mu m_{(c)}$), the decrease of the wear intensity was $K_{Z2(RV1)}/K_{Z2(RV3)}=3$ times.

In terms of volume losses, if the last measured value and the first measured value of the flow through a clearance are taken into account, the results show that in the case of using oil cleanliness level ISO 22 (for particles ≥4 $\mu m_{(c)}$), the ratio is equal to $\Delta Q_{e(10^6)}/\Delta Q_{e(0)}=1.97$, and in case of using oil cleanliness level ISO 21 (for particles ≥4 $\mu m_{(c)}$) the ratio is equal to $\Delta Q_{e(10^6)}/\Delta Q_{e(0)}=1.83$, and in case of using oil cleanliness level ISO 20 (for particles ≥4 $\mu m_{(c)}$) the ratio is $\Delta Q_{e(10^6)}/\Delta Q_{e(0)}=1.79$.

Additionally, it is evident that between theoretically calculated and experimentally measured values of the flow through the clearance, there are differences which increase with the increase of the value of clearance, but the experimental values have much lower growth in comparison to theoretically calculated values of the flow.

By measuring pressure drop values during the experiment, it was found that the oil cleanliness level has an impact on the pressure drop increase. Due to the pressure drop increase, more heat is generated which decreases overall system efficiency.

4 REFERENCES

[1] Parker Hannifin Ltd. (2010). Hydraulic fluids: Controlling contamination in hydraulic fluids. *Filtration & Separation*, vol. 47, no. 3, p. 28-30, **DOI:10.1016/s0015-1882(10)70127-0**.

[2] Hydac International (2012). Filtration Handbook. *from http://www.hydac.com.tr/download.html?path=templates%2Fhydac%2Fupload%2Ffile%2Fproducts%5CFiltrasyon%5Fbrosur1%2Epdf*, accessed on 23-11-2017.

[3] Ng, F., Harding, J.A., Glass, J. (2017). Improving hydraulic excavator performance through in line hydraulic oil contamination monitoring. *Mechanical Systems and Signal Processing*, vol. 83, p. 176-193, **DOI:10.1016/j.ymssp.2016.06.006**.

[4] Kovari, A. (2009). Influence of cylinder leakage on dynamic behavior of electrohydraulic servo system. *7th International Symposium on Intelligent Systems and Informatics*, p. 375-379, **DOI:10.1109/SISY.2009.5291129**.

[5] Strmčnik, E., Majdič, F. (2017). Comparison of leakage level in water and oil hydraulics. *Advances in Mechanical Engineering*, vol. 9, no, 11, p. 1-12, **DOI:10.1177/1687814017737723**.

[6] Battat, B., Babcock, W. (2003). Understanding and reducing the effects of contamination on hydraulic fluids and systems. *The Advanced Materials & Processes Technology Information Analysis Center Quarterly*, vol. 7, no. 1, p. 11-15.

[7] Nash, T. (2006). Filtration: It's the little things that get you, *Hydraulics and Pneumatics*, no. 5, p. 29-31.

[8] Bosch Rexroth AG (2011). Rexroth Oil Cleanliness Booklet, from *http://www.hksm.com.tr/Images/dosya/rexroth-oil-clean.pdf*, accessed on 28-08-2018.

[9] Kumar, M., Mukherjee, P.S., Misra, N.M. (2013). Advancement and current status of wear debris analysis for machine condition monitoring: a review. *Industrial Lubrication and Tribology*, vol. 65, no. 1, p. 3-11, **DOI:10.1108/00368791311292756**.

[10] Karanović, V., Jocanović, M., Jovanović, V. (2014). Review of development stages in the conceptual design of an electro-hydrostatic actuator for robotics. *Acta Polytechnica Hungarica*, vol. 11, no. 5, p. 59-79, **DOI:10.12700/APH.11.05.2014.05.4**.

[11] Johnson, J.L. (2010). Q&A about servo and proportional valves. *Hydraulics and Pneumatics*, no. 7, p. 30-39.

[12] ISO 12669:2017. *Hydraulic Fluid Power — Method for Determining the Required Cleanliness Level (RCL) for a System*. International standardization organization, Geneva.

[13] ISO 4406:2017. *Hydraulic fluid power — Fluids — Method for coding the level of contamination by solid particles*. International standardization organization, Geneva.

[14] Rabinowicz, E. (1995). *Friction and Wear of Materials*. John Wiley and Sons, New York.

[15] An, L., Sepehri, N. (2005). Hydraulic actuator leakage fault detection using extended Kalman filter. *International Journal of Fluid Power*, vol. 6, no, 1, p. 41-51, **DOI:10.1080/14399776.2005.10781210**.

[16] Kovari, A. (2015). Effect of leakage in electrohydraulic servo systems based on complex nonlinear mathematical model and experimental results. *Acta Polytechnica Hungarica*, vol. 12, no. 3, p. 129-146, **DOI:10.12700/APH.12.3.2015.3.8**.

[17] Liu, Y., Ma, B., Zheng, C., Zhang, S. (2015). Degradation modeling and experiment of electro-hydraulic shift valve in contamination circumstances. *Advances in Mechanical Engineering*, vol. 7, no. 5, p. 1-9, **DOI:10.1177/1687814015585925**.

[18] Basta, T.M. (1971). Engineering Hydraulics. *Mashinostroenie*, Moscow.

[19] Jocanović, M. (2010). *Approach to Research and Define the Model for the Calculation of Flow of Solid Particles with a Mass of Mineral Oil through the Gaps in a Function of the Constructive Operating Parameters of Hydraulic Components*. Ph.D. thesis, University of Novi Sad, Novi Sad.

[20] Fitch, E.C., Hong, I.T. (2004). *Hydraulic System Design for Service Assurance*, BarDyne Inc, Stillwater.

[21] Casey, B. (2012). How Silt Lock Can Destroy Hydraulic Valves, from *http://www.machinerylubrication.com/Read/28853/silt-lock-hydrauli*, accessed on 03.09.2018.

Strojniški vestnik - Journal of Mechanical Engineering 65(2019)3, 148-160

DOI:10.5545/sv-jme.2018.5802 Original Scientific Paper
Received for review: 2018-10-18
Received revised form: 2019-01-28
Accepted for publication: 2019-02-27

Motion Planning for Highly Automated Road Vehicles with a Hybrid Approach Using Nonlinear Optimization and Artificial Neural Networks

Ferenc Hegedüs[1] - Tamás Bécsi[2,*] - Szilárd Aradi[2] - Péter Gáspár[3]
[1]Robert Bosch, Hungary
[2]Budapest University of Technology and Economics, Department of Control for Transportation and Vehicle Systems, Hungary
[3]Hungarian Academy of Sciences, Computer and Automation Research Institute, Hungary

Over the last decade, many different algorithms were developed for the motion planning of road vehicles due to the increasing interest in the automation of road transportation. To be able to ensure dynamical feasibility of the planned trajectories, nonholonomic dynamics of wheeled vehicles must be considered. Nonlinear optimization based trajectory planners are proven to satisfy this need, however this happens at the expense of increasing computational effort, which jeopardizes the real-time applicability of these methods. This paper presents an algorithm which offers a solution to this problematic with a hybrid approach using artificial neural networks (ANNs). First, a nonlinear optimization based trajectory planner is presented which ensures the dynamical feasibility with the model-based prediction of the vehicle's motion. Next, an artificial neural network is trained to reproduce the behavior of the optimization based planning algorithm with the method of supervised learning. The generation of training data happens off-line, which eliminates the concerns about the computational requirements of the optimization-based method. The trained neural network then replaces the original motion planner in on-line planning tasks which significantly reduces computational effort and thus run-time. Furthermore, the output of the network is supervised by the model based motion prediction layer of the original optimization-based algorithm and can thus always be trusted. Finally, the performance of the hybrid method is benchmarked with computer simulations in terms of dynamical feasibility and run-time and the results are investigated. Examinations show that the computation time can be significantly reduced while maintaining the feasibility of resulting vehicle motions.

Keywords: automated driving, motion planning, trajectory planning, vehicle control, nonlinear optimization, artificial neural networks

Highlights

- *A model-based, multi-objective, dynamically feasible trajectory planner is introduced, which solves the motion planning problem through online nonlinear optimization.*
- *Although the method has high performance, it also requires major computational effort, which is not acceptable for real-time application.*
- *An ANN based approach is proposed to provide close-to-optimal initial value for the optimization process.*
- *A novell ANN based method is proposed to replace the online optimization process, while also supervising the output of the ANN.*
- *Training benchmarks, behavior comparison and simulation prove the performance of the developed solutions.*

0 INTRODUCTION

Highly automated and autonomous driving is expected to contribute to the quality of road transportation in multiple ways. The most important impact can be the improvement of road safety. Owing to the spread of passive and active electronic safety systems, the number of fatal road accidents has been reduced by 48 % between 2001 and 2015 in the European Union [**1**]. Higher degree of automation could further increase road safety as human factors are still responsible for the majority the remaining incidents. Energy efficiency and environmental friendliness is also an increasing social requirement. Researches show that automated vehicles could save up to 10 % to 30 % fuel by utilizing optimized route finding and driving strategies [**2**] and [**3**]. Road traffic parameters, such as average travel time and traffic flow capacity are also predicted to improve significantly [**4**].

The numerous expectations make autonomous driving the most important research field for both industrial and academic institutions concerning road transportation. Although there are many technical challenges to solve, one of the most important aspects is navigating the automated vehicle in the dynamic traffic environment. The decision making process generally has a hierarchical structure with 3 major levels. The highest level in the hierarchy is called route planning and is responsible for finding an appropriate route through the available road infrastructure from the current position to the required end destination. The middle level - behavior planning - navigates the selected route and interacts with the other traffic participants according to road rules. This paper addresses the lowest layer called motion planning. The

*Corr. Author's Address: Robert Bosch, 2 Stoczek street, 1111 Budapest, Hungary, hegedus.ferenc@mail.bme.hu

motion planning layer is fed by behavior planning with some maneuver primitives (e.g. lane-change or right-turn) and generates the trajectory of the vehicle. The trajectory contains not only the desired path that the vehicle should travel along but it also includes all temporal quantities which describe the vehicle's motion e.g. the associated velocity and acceleration. The collection of these quantities is called the state or the configuration of the vehicle [**5**].

The trajectory of the vehicle must be safe, dynamically feasible, comfortable and customizable according to the preferences of individual passengers. A further requirement against the planning algorithm is that it must be computable fast enough to enable real-time application on state of the art hardware. Over the last decades, many different approaches have been developed to solve the motion planning problem. However, to the best of author's knowledge, no method was provided with the capability of satisfying all above requirements simultaneously. Classical motion planning approaches can be split into four major categories. Namely, there are geometric based methods, graph search based algorithms, incremental search techniques and variational methods. The first three kind of algorithms are rather suitable for path planning only, which path is then later transformed to a trajectory by assigning time information in a further step. Furthermore, the possibility to consider the vehicle's nonholonomic motion is strongly limited.

Geometric methods are composing the vehicle's path from geometric curves like circular arcs, clothoids [**6**], polynomial splines, or polynomial function of time or arc length [**7**]. The parameters of the curves are usually calculated based on geometric boundary conditions (e.g. initial and final positions of the vehicle) considering the limited steering angle and side acceleration of the vehicle along the curve [**8**]. The advantage of these algorithms is that they are computationally cheap. Because of this, a common approach to generate a suboptimal collision-free motion is to evaluate multiple candidates into different terminal configurations and choose the best amongst safe ones for execution according to some cost function [**9**].

Graph search methods have been used for path finding problems since Dijkstra's algorithm have been published [**10**]. These algorithms are using a discretization of the vehicle's spatiotemporal environment and building a graph from the feasible and unoccupied points or motion primitives. The dimension of the state space used [**11**] as well as resolution of the discretization can be set adaptively to balance between computational effort and path quality [**12**]. With the Hybrid A* algorithm it is also possible to associate a continuous state with each discrete cell resulting a much smoother path [**13**].

Instead of a fixed discretization of space time, incremental search techniques such as rapidly-exploring random tree (RRT) and its extensions are building the graph by random sampling [**14**]. The graph begins at the initial configuration of the vehicle and is incremented by randomly sampled new configurations from its unoccupied environment. Some appropriate distance metrics (e.g. Dubins path [**15**]) is used to determine the vertex of the graph that the new point can be connected to. RRT can also be extended by predicting the response of a closed loop controller-vehicle model to the randomly sampled reference and using the resulting response to build the graph [**16**].

Variational methods are formulating the trajectory planning problem as a nonlinear constrained optimization, and often draw ideas from other optimal control techniques such as model predictive control (MPC). The aim is usually to find some appropriate input functions that drive the model of the vehicle into a prescribed end state while minimizing a cost function that represents the quality of the trajectory [**17**]. The problem can be discretized by using a parametrization of the input functions. These methods enable the usage of more complex dynamic models or even real measurements for the prediction of the vehicle's motion an can therefore ensure a dynamical feasibility in a much wider range of driving conditions [**18**]. Obstacle avoidance can also be integrated in the optimization problem formulated in form of additional constraints [**19**].

Beside the classical methods, an emerging interest is shown throughout the field of robotics towards artificial neural networks well known for their outstanding performance in learning, adaptation, generalization and optimization. Additionally, as the required computational time of application of a trained neural network is significantly lower than the run-time required for traditional optimizing algorithms, these networks have high potential for real-time applications. These capabilities make application of such networks worth considering in the assessment of possible solutions for complex problems featuring recognition, learning and decision-making as trajectory planning. Applications for path planning and motion control of multi-joint manipulators [**20**] or servo motor systems [**21**] are target to current researches.

Known researches discussed the problem of collision-free trajectory planning using nonholonomic vehicle model. Some of them were to conduct obstacle avoidance in dynamic environment [22] [23]. Several works included mapless navigation with free- path detection using on-board sensors such as ultrasonic sensors [24] or laser scanner [25]. Reinforcement learning methods were also introduced both utilizing off-line [26] and on-line training [27]. Different artificial neural network aided approaches were presented using nonholonomic vehicle models in the field of control design for automated parking [28], and vehicle motion prediction, where the network is trained to replicate the dynamics of a specific vehicle [29]. However, application of artificial neural networks in safety relevant systems is only possible with post filtering by traditional algorithm.

The paper is organized as follows. Section 1 introduces in details the nonlinear optimization based motion planning algorithm which is the basis of our examinations. In Section 2 the proposed hybrid approach is described which utilizes artificial neural network combined with classical methods to ensure feasible output. The performance of the algorithm is then benchmarked in Section 3, and Section 4 contains conclusion summary and offers future research directions.

1 MOTION PLANNING WITH MODEL-BASED OPTIMIZATION

1.1 The Motion Planning Problem

When planning a trajectory, the objective is to find the inputs (steering angle, driving or braking torque) that drive the vehicle from the current initial state to a desired end state with respect to its nonholonomic dynamics, meanwhile satisfying the requirements described in Section 0, namely; safety, dynamical feasibility, comfort, and the possibility of customization. Safety means that the trajectory must not lead to collision with fellow traffic participants. To reach dynamical feasibility, the vehicle must be able to drive along the planned trajectory with respect to its nonholonomic dynamics. Passenger comfort is strongly subjective, but researches show that it is in correlation with the magnitude of acceleration and jerk along the trajectory [30]. The passengers should also be able to influence motion characteristics within the limits of dynamical feasibility, e.g. to prefer minimal travel time over comfort and vice versa.

Mathematically, the motion planning can be formulated as a constrained nonlinear optimization problem as follows:

$$\min_{p} \; J(X(p,t)) = \sum_{i} w_i z_i(X(p,t)), \tag{1}$$

subject to

$$\dot{X}(p,t) = f(X(p,t),u(p,t)), \tag{2}$$

$$C(X(p,t)) = 0. \tag{3}$$

Firstly, Eq. (1) is the objective function where arbitrary trajectory qualifiers $z_i(X(p,t))$ can be specified depending on the state of the vehicle $X(p,t)$ which are describing the goodness of the generated motion, and the influence of these qualifiers is weighted by factors w_i. The weighting also allows some customization according to individual preferences of passengers. The applied objective function is detailed in Subsection 1.2. Secondly, Eq. (2) represents the dynamics of the vehicle introduced in Subsection 1.3. Finally, Eq. (3) represents that the vehicle must reach the required end state formulated as constraint equation $C(X(p,t))$, which topic is detailed in Subsection 1.4. The optimized variable p is a vector of parameters which are determining the input of the vehicle $u(p,t)$. The input parametrization is described in Subsection 1.5.

1.2 Objective Function

Main contributors to passenger discomfort are acceleration and jerk, because these quantities influence the acting force. In [31] it was shown that the application of the following cost function can effectively be used for optimization based trajectory planning to maintain passenger comfort and minimize travel time at the same time:

$$\begin{aligned} J(X(p,t)) = & w_t t_f + w_j \int_0^{t_f} [\dddot{y}^V(t)]^2 dt + \\ & w_a \int_0^{t_f} [\ddot{y}^V(t)]^2 dt, \end{aligned} \tag{4}$$

where $\dddot{y}^V$ and $\ddot{y}^V$ are the lateral jerk and acceleration of the vehicle, t_f is the travel time along the trajectory, and w_j, w_a, and w_t are weighting constants.

1.3 Model of Dynamics

From the perspective of the optimization problem, the model of the vehicle dynamics can be of any kind. On one hand, to ensure a high level of dynamical feasibility, the model should precisely describe the motion of the vehicle in every governable driving scenarios. On the other hand, calculation of the vehicle's motion comes with a considerable amount of computation effort, which should be obviously kept

as low as possible. The vehicle model applied in this paper is an enhanced version of the nonlinear single track model that is used in [**32**].

The planar multi-body model (Fig. 1) consists of a chassis with mass m and moment of inertia θ about its vertical axis (z^V), and virtual front and rear wheels with moment of inertia θ_f, θ_r about their own rotation axes (y_f^V, y_r^V) representing the complete front and rear axes of the vehicle. The chassis can move longitudinally x and laterally y, and rotate ψ about its vertical axis. The wheels can rotate ρ_f, ρ_r about their axes as well. The center of gravity of the vehicle is considered to be constant. The radii of the wheels are noted with r_f and r_f, the center of gravity height of the vehicle is marked with h, and the horizontal distance between the center of gravity and the front and rear wheel centers are denoted with l_f and l_f respectively. The inputs of the model are the steering angle of the front wheel δ and the total applied driving M_d and braking M_b torques. In the following Subsections 1.3.1 and 1.3.2 superscripts are used to distinguish dynamic quantities in the ground's (no superscript) vehicle's (V) and in the wheel's (W) coordinate system. The coordinate transformations between the different coordinate systems are not detailed due to limited space. Furthermore, all time derivatives are noted with dot ($\dot{}$).

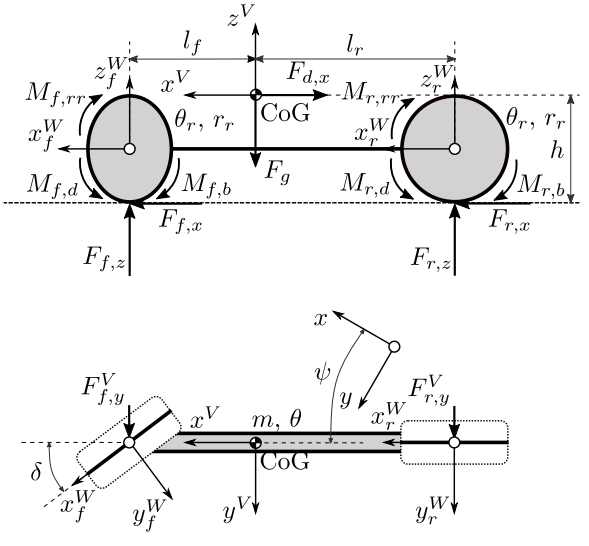

Fig. 1. *Nonlinear single track vehicle model*

1.3.1 Dynamics of the Wheels

A dynamic wheel slip model is introduced based on [**33**] to increase the precision of the simulation in case of near-standstill (drive-off, full braking) situations, and to enable the usage of explicit ordinary differential equation (ODE) solvers and larger step sizes. The dynamic equations for the front wheel are the following:

$$\ddot{\rho}_f = \frac{1}{\theta_f}\left(M_{f,d} - r_f F_{f,x}^W - M_{f,b} - M_{f,rr}\right), \quad (5)$$

$$\dot{s}_{f,x} = \frac{1}{l_{f,x}}\left(r_f\dot{\rho}_f - \dot{x}_f^W - |\dot{x}_f^W|s_{f,x}\right), \quad (6)$$

$$\dot{s}_{f,y} = \frac{1}{l_{f,y}}\left(-\dot{y}_f^W - |\dot{x}_f^W|s_{f,y}\right). \quad (7)$$

Eq. (5) represents the motion of the wheel. In case of driving, the total driving torque is distributed by an arbitrary factor ξ_M between the front $M_{d,f}$ and rear $M_{d,r}$ wheels. In case of braking, ideal break torque distribution (in sense that the longitudinal wheel slip values are equal for the two wheels) is applied to compute the wheel braking torques $M_{b,f}$ and $M_{b,r}$. Eqs. (6) and (7) are used to calculate the dynamic longitudinal and lateral wheel slips. The slip dependent longitudinal relaxation length is:

$$l_{f,x} = max\left(l_{f,x,0}\left(1 - \frac{C_{f,F}}{3D_{f,x}}|s_{f,x}|\right), l_{f,x,min}\right), \quad (8)$$

with $C_{f,F} = B_{f,x}C_{f,x}D_f$, where $l_{f,x,0}$ and $l_{f,x,min}$ are the longitudinal relaxation lengths at standstill and at wheel spin or lock respectively. Eq. (8) is also valid for the lateral direction $l_{f,y}$ as well, with the substitution of subscripts x and y. The tire forces are calculated by the Magic Formula:

$$\begin{aligned} F_{f,x}^W = & D_f \sin\{C_{f,x}\arctan(B_{f,x}\tilde{s}_{f,x} - \\ & E[B_{f,x}\tilde{s}_{f,x} - \arctan(B_{f,x}\tilde{s}_{f,x})])\}, \end{aligned} \quad (9)$$

with $D_f = \mu_f F_{f,z}^W$, where μ_f is the static coefficient of friction between tire and road surfaces, and $B_{f,x}$, $C_{f,x}$, $E_{f,x}$ are parameters. Eq. (9) is valid for the lateral direction $F_{f,y}^W$ as well, with the substitution of subscripts x with y.

To enhance the behavior of the model at very low speeds e.g. when starting from or braking to standstill, a slip damping factor is applied like following:

$$k_{f,x} = \begin{cases} \frac{1}{2}k_{f,x,0}\left(1 + \cos\left(\pi\frac{|\dot{x}_f^W|}{v_{low}}\right)\right), & \text{if } \dot{x}_f^W \le v_{low} \\ 0, & \text{if } \dot{x}_f^W > v_{low} \end{cases}, \quad (10)$$

where $k_{f,x,0}$ is the damping value zero velocity and v_{low} is the velocity at which damping is switched off. The

damping is only applied in the longitudinal direction, the damped slip values are:

$$\tilde{s}_{f,x} = s_{f_x} + \frac{k_{f,x}}{C_{f,F}}(r_f\dot{\rho}_f - \dot{x}_f^W), \tag{11}$$

$$\tilde{s}_{f,y} = s_{f,y}. \tag{12}$$

The rolling resistance torque is calculated as follows:

$$\begin{aligned} M_{f,rr} =& F_{f,z}^W r_f sign(r_f\dot{\rho}_f)\cdot \\ & [A_{rr} + B_{rr}|r_f\dot{\rho}_f| + C_{rr}(r_f\dot{\rho}_f)^2], \end{aligned} \tag{13}$$

where A_{rr}, B_{rr}, and C_{rr} are rolling resistance coefficients. Eqs. (5) to (13) are all valid for the rear wheel with changing the subscripts from f to r.

1.3.2 Dynamics of the Chassis

The dynamics of the chassis is now expressed in the inertial coordinate system of the ground. The equations of motion are:

$$\ddot{x} = \frac{1}{m}(F_{f,x} + F_{r,x} + F_{d,x}), \tag{14}$$

$$\ddot{y} = \frac{1}{m}(F_{f,y} + F_{r,y} + F_{d,y}), \tag{15}$$

$$\ddot{\psi} = \frac{1}{\theta}(l_f F_{f,y}^V - l_r F_{r,y}^V). \tag{16}$$

Aerodynamic drag force is applied to the vehicle according to the following:

$$F_{d,x}^V = \frac{1}{2}c_D A_f \rho_A \dot{x}^V\sqrt{\dot{x}^V + \dot{y}^V}, \tag{17}$$

$$F_{d,y}^V = \frac{1}{2}c_D A_f \rho_A \dot{y}^V\sqrt{\dot{x}^V + \dot{y}^V}, \tag{18}$$

where c_D is the drag coefficient and A_f is the frontal area of the vehicle, and ρ_A is the mass density of air.

1.3.3 Closed Loop Control

Since the developed motion is described by the temporal course of the vehicle's state along the trajectory, a mapping is needed between wheel level inputs (steering angle δ, driving M_d and braking M_b torque) to some of the state variables to facilitate the usage of input functions meaningful from the perspective of vehicle motion. This mapping is reached by applying closed loop trajectory tracking control. From the view of the optimization problem, arbitrary methods can be used to implement the control. In this paper, two independent linear quadratic regulator (LQR) controls are used. The longitudinal controller is responsible for the tracking of longitudinal velocity reference v_{ref} as well as the lateral controller follows a yaw-rate ω_{ref} reference. The selection of controllers is of course in close relationship with the input functions applied in the optimization problem, described in Subsection 1.5.

1.4 Constraints

The required end configuration of the vehicle must be formulated in form of constraints for the optimization problem described in Eq. (3). In this work this is happening with application of nonlinear equality constraints. The minimum feasible set of specified end state variables are position x_f, y_f and orientation ψ_f, however it is also reasonable to define the yaw rate $\dot{\psi}_f$. Accordingly, the applied constraint equation is:

$$C(X) = X_f - X(t_f) = \begin{bmatrix} x_f \\ y_f \\ \psi_f \\ \dot{\psi}_f \end{bmatrix} - \begin{bmatrix} x(t_f) \\ y(t_f) \\ \psi(t_f) \\ \dot{\psi}(t_f) \end{bmatrix} = 0. \tag{19}$$

1.5 Input Functions

In [17] it is shown that longitudinal velocity and yaw rate can efficiently (relatively small number of parameters enables feasible customization) be parametrized to describe the vehicle's motion. In current work, longitudinal velocity is always chosen constant ($v_{ref} = const.$) along the trajectory to reduce the number of free parameters. This choice is not unreasonable because the travel time typically remains in range of a few seconds.

As the yaw-rate input signal, a polynomial spline profile shown in Fig. 2 is used. The spline is parametrized by knot points that are placed equidistantly, and by the time span. In current work,

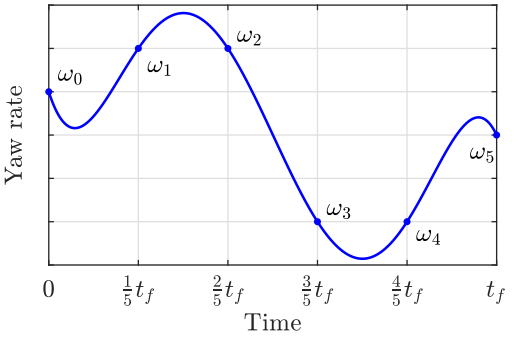

Fig. 2. *Yaw-rate reference signal parametrization*

a cubic spline is used which means 4 knot point parameters and the travel time parameter additionally. The first knot point is however chosen to be exactly the initial value of yaw-rate of the vehicle $\dot{\psi}_i$ to avoid jumps in control inputs. Accordingly, the reduced parameter vector is:

$$p_\omega = \begin{bmatrix} \omega_1 & \omega_2 & \omega_3 & t_f \end{bmatrix}^T. \tag{20}$$

1.6 Solution of the Planning Problem

Fig. 3 shows the architecture of how the solution $\hat{p}$ of the optimization problem represented by Eqs. (1) to (3) is found. The inputs of the optimization process are the current initial state X_i, and the required terminal state X_f of the vehicle, and an initial guess on the input function parameters p_0. The initial guess is chosen to the parameters of straight drive, namely:

$$p_0 = \begin{bmatrix} 0 & 0 & 0 & x_f/v_{ref} \end{bmatrix}. \tag{21}$$

The iteration step begins with the evaluation of the input function (the polynomial spline yaw rate reference) based on the parameter values. The response of the controller-vehicle system is then calculated by the following equation:

$$X(p,t) = X_i + \int_0^t f(X(p,\tau),u(p,\tau)d\tau, \tag{22}$$

which can be solved numerically with the 4$^{\text{th}}$ Runge-Kutta method for instance. Knowing the trajectory, the objective function (Eq. (4)) and the constraint function (Eq. (19)) are evaluated, and the optimization solver checks if a feasible solution is found. If so, the motion planning is solved. Otherwise, the optimization solver calculates a correction of the parameters based on the objective and constraint values and starts a new iteration step with these corrected values.

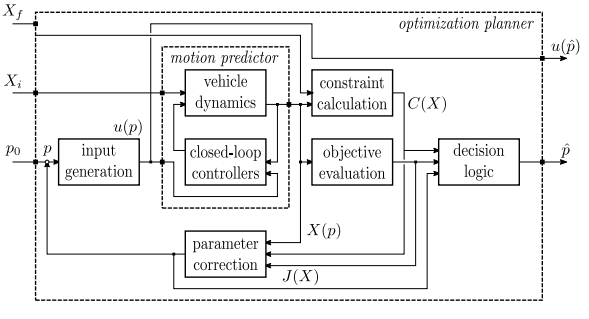

Fig. 3. *Optimization planner architecture*

As an optimization solver, interior point methods, trust region methods or sequential quadratic programming methods can be used.

2 HYBRID APPROACH USING ARTIFICIAL NEURAL NETWORKS

2.1 Basic Concept

The nonlinear optimization based trajectory planning method presented in Section 1 introduces a sophisticated vehicle dynamics-focused approach. This comes at the price of significant computational requirements, which makes the current implementation unable to fulfill real-time applicability. Artificial neural networks have been used for function approximation since a long time. During planning, the optimization planner performs a mapping from the initial and terminal configurations of the vehicle to the appropriate input function parameters that will drive the vehicle accordingly. With the training of an artificial neural network via supervised learning to approximate this mapping, the optimization motion planning algorithm could be substituted. However, the trained neural network will always behave as a black box system. As such, it cannot be applied as a standalone algorithm, because there is no guarantee that it will produce a feasible output in all scenarios. In this paper, two possible applications of an artificial neural network are described, which are operating the network together with the classical model based methods to provide feasible motions with faster computation times.

2.2 Initial Value Generator

The computation time of the optimization planner can be greatly decreased, if the initial guess of the optimized variable p_0 is already close to the optimal solution. The initial value chosen in Eq. (21) is however obviously not near the optimum. The first idea is to use the neural network to provide a better initial guess instead. As the neural network is trained to provide the optimal solution, its output is expected to be at least close to the optimum considering also the estimation error. The output of the network flows through the whole original optimization loop (Fig. 3, 3$^{\text{rd}}$ input), which means that the process will correct a potential infeasible result. In the following, this approach will be referred to as *initialized optimization planner*.

2.3 Hybrid Neural Network Planner

Another possibility is to completely substitute the on-line optimization with the neural network as shown in Fig. 4. The plausibility of the network's output is in this case checked with the motion predictor which is the core of the optimization algorithm. The end

state of the vehicle actually reached when driven by the input signals provided by the neural network estimator is compared with the required end state. In case the magnitude of error is not permissible, an emergency trajectory can be used. This solution will be referred to as *hybrid nn planner*.

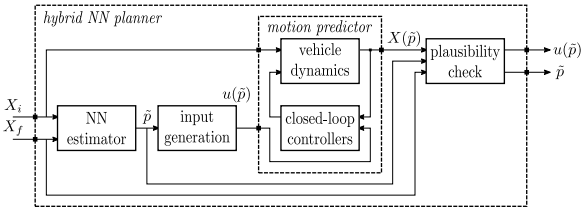

Fig. 4. *Hybrid NN planner architecture*

2.4 Training of Networks

As described in Subsections 2.2 and 2.3, our goal here is to create a network that can substitute the above mentioned trajectory planning algorithm, or at least provide a sufficient initial value guess for the optimizer. Numerous artificial neural networks with different parameter sets were trained to fulfill these tasks.

The network's input consists of the vehicle's state variables selected as constraints for the optimization problem in Eq. (19) both at the initial and at the target configurations. Additionally, the initial and final state vectors are both containing the selected constant travel velocity v_{ref} described in Subsection 1.5. The network's output contains the parameters of the third-order yaw-rate reference spline defined in Eq. (20).

A data set of 16000 lane changing and curved lane keeping trajectory samples for training was generated with the model-based optimization proposed in Section 1. From the start configuration of:

$$\begin{aligned} X_i &= \begin{bmatrix} x_i & y_i & \psi_i & \dot{\psi}_i & v_i \end{bmatrix}^T \\ &= \begin{bmatrix} 0 & 0 & 0 & 0 & v_{ref} \end{bmatrix}^T, \end{aligned} \tag{23}$$

the target state vectors are defined by the following equations and ranges:

$$X_f = \begin{bmatrix} x_f \\ y_f \\ \psi_f \\ \dot{\psi}_f \\ v_f \end{bmatrix} = \begin{bmatrix} 50 \ldots 100 & \text{m} \\ -0.15x_f \ldots 0.15x_f & \text{m} \\ -0.1\psi_C \ldots 1.2\psi_C & \text{rad} \\ v_{ref}\frac{\sin(\psi_f)}{x_f} & \text{rad/s} \\ v_{ref} & \text{m/s} \end{bmatrix}, \tag{24}$$

where $\psi_C = 2\arctan(\frac{y_f}{x_f})$ is the yaw angle of circular path, and v_{ref} is chosen to 20 m/s. The ranges were determined by vehicle simulations to cover the whole dynamically feasible region ahead of the vehicle, and the edges are selected to reach even extreme dynamical parameters (e.g. lateral acceleration up to near 1g). A portion of the generated sample trajectories is shown in Fig. 5. In Section 3, all the figures will show the results regarding to these trajectories, in the ascending order of maximal lateral acceleration.

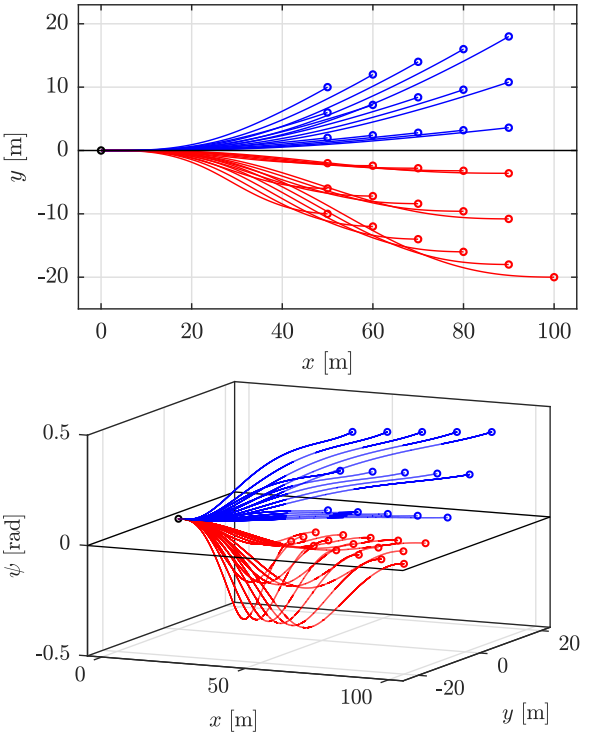

Fig. 5. *Sample trajectories*

The core of the complex problem of computing dynamically feasible motions is irrelevant from the perspective of the training of an artificial neural network. The problem that the network is needed to provide a solution for is handled as a general function approximation. In order to explore the benefits of different networks to reach the best regression possible, several parameters defining the training or the network itself were used in every possible combinations. Although Levenberg-Marquandt algorithm is well-known for its superior performance in function approximation, in order to perform a more comprehensive study on the training process, Broyden–Fletcher–Goldfarb–Shanno (BFGS) and resilient back-propagation algorithms were also targets of examination.

Regarding network architecture two variants defining the connection of the adjacent layers differently were tested: feed-forward and cascade structures.

The input layer defined by the input vectors consists of 10 neurons, while the output layer using linear transfer function is of 4 neuron size, corresponding to the output vector defining the planned yaw-rate reference. Hidden layers use tangent sigmoid transfer function were examined in seven different structures: one layer sized [10] and [20], two layers sized [10; 8], [20; 8], [30; 10], three layers sized [10; 20; 8], [20; 10; 8]. The decomposition of the training data set for train, validation and test sets is also a factor worth consideration regarding the result of the training. Five different ratios were tested: [80:10:10], [70:15:15], [60:25:15], [60:15:25] and [50:25:25]. Every network with different parameter sets were trained five times with different initial values and were saved with the weights and biases culminating in the best test results, in order to exclude the effect of the potentially occurring error of finding local extremes instead of the global minimum of the error function during the training process. As it was expected, the training algorithm resulting in the fastest convergence was the Levenberg-Marquandt method, which resulted the networks to reach the performance goal in an order of magnitude faster than the networks trained with either BFGS or resilient back-propagation algorithm. Based on the test results, one hidden layer sized cascade networks and networks with multiple hidden layers provided the best performance on the test data set, while no major difference was occurring regarding the number of neurons.

In respect to regression, the trained networks perform the function approximation task with mean squared error values around 10^{-2} on the test data set.

3 TESTING AND BENCHMARKING

3.1 Comparison of Run-time

Fig. 6 shows the run-time of the motion planning algorithms normalized to the run-time of the *optimization planner*:

$$k_t(i) = \frac{t^j_{calc}(i)}{t^{opt}_{calc}(i)}, \tag{25}$$

where i is the index of the trajectory, $t^{opt}_{calc}(i)$ is the calculation time of the i^{th} trajectory with the *optimization planner*, and $t^j_{calc}(i)$ is the calculation time with planner j. The average planning time of the *initialized optimization planner* is decreased significantly by 51 %. The speed-up is even more essential in case of the *hybrid nn planner*, the average planning time is here decreased by 96.63 %.

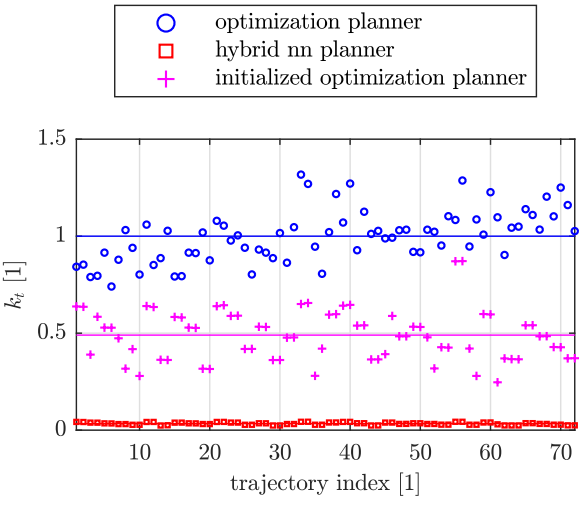

Fig. 6. *Normalized run-times*

As the run-time of the optimization planner is in the magnitude of 1 s, the results show, that even the current MATLAB based implementation of the *hybrid nn planner* may be suitable for real-time application from the perspective of planning time.

3.2 Comparison of Performance

3.2.1 Performance of Reference Parameter Estimation

The deviation between the planned reference parameters normalized to the output parameters of the *optimization planner* shown in Fig. 7 is calculated by:

$$k_p(i) = \left\| \frac{p^j(i) - p^{opt}(i)}{p^{opt}(i)} \right\|, \tag{26}$$

where $p^{opt}(i)$ is the parameter vector generated by the *optimization planner* in case of the i^{th} trajectory, and $p^j(i)$ is the parameter vector in case of planner j.

As expected, the deviation of the input function parameters is negligible in case of the *initialized optimization planner*. On the other hand, the *hybrid nn planner* produces a deviation of 4.35 % in average, that even reaches 14.76 % maximally. The values show how well neural network could be trained. It can be declared, that the goodness of the estimation is not in correspondence with the dynamical complexity of the trajectory, as it is not increasing or decreasing with growing lateral accelerations. Although the deviations are not very small, the main point is the influence of the estimation error to the motion of the vehicle.

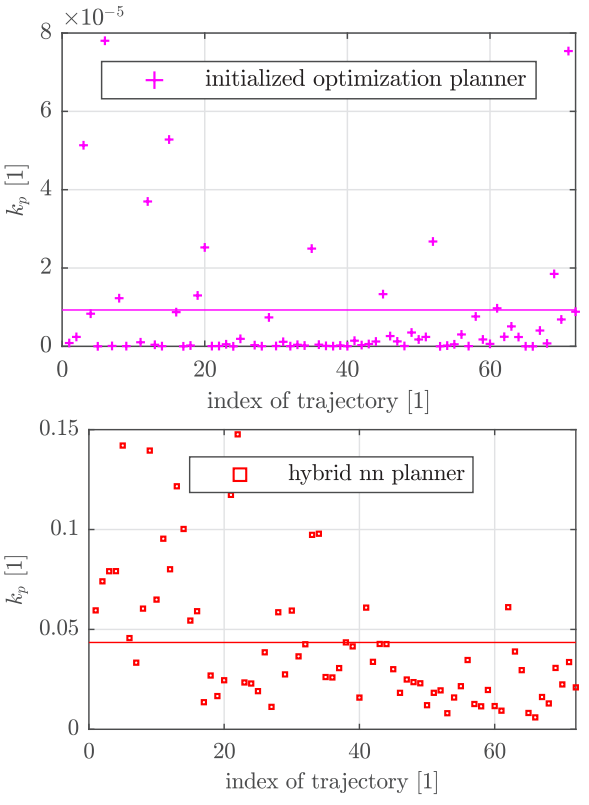

Fig. 7. *Normalized deviation of reference parameters*

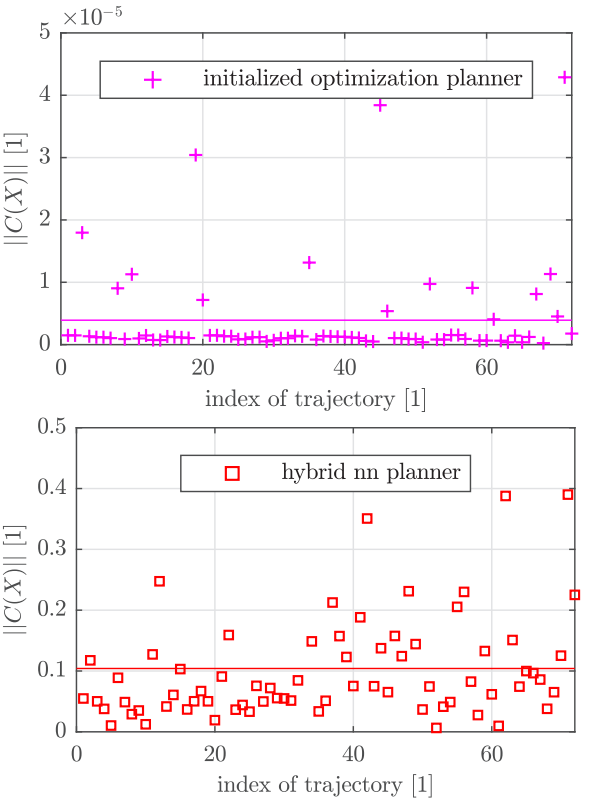

Fig. 8. *Final deviation of vehicle state*

3.2.2 Deviations in Vehicle State

The final value of state constraints, namely the euclidean norm of deviation between prescribed X_f and actually reached $X(t_f)$ end states of the vehicle is shown in Fig. 8. The deviation of the *initialized optimization planner* is again negligible, as the constraint tolerance of the nonlinear optimization solver is set to a sufficiently low value (10^{-4}). In case of the *hybrid nn planner*, the norm of state constraint is noticeable. This is expected based on the results in Fig. 7. The main contributor to the total value is the deviation in the final vehicle position, so we can declare a maximal position error of approximately 40 cm after the whole planned motion (≈2 s), which is remarkable.

However, the motions planned by the algorithm are actually only meant to be executed until the result of the next trajectory planning cycle is being calculated (≈50 ms), and new trajectories are expected to be planned as frequently as possible. The vehicle state deviation when considering only the executed part of the trajectory is calculated as follows:

$$C_T(X) = X^{opt}(t^{nn}_{calc}) - X^{nn}(t^{nn}_{calc}), \qquad (27)$$

where $X_{opt}(\cdot)$ and $X_{nn}(\cdot)$ are the state of the vehicle in case of the *optimization planner* and the *hybrid nn planner* respectively, and t^{nn}_{calc} is the maximal calculation time with the *hybrid nn planner*.

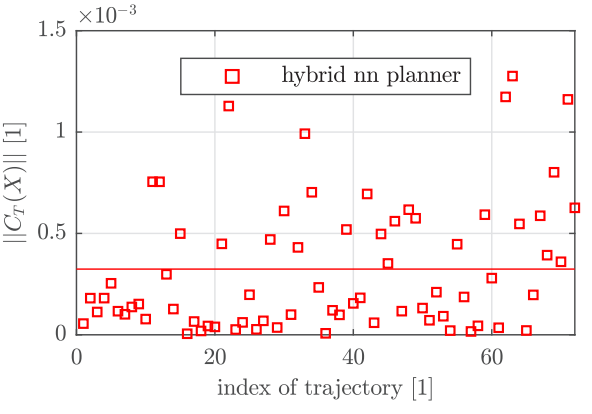

Fig. 9. *Final deviation of vehicle state considering only the driven part*

The results in Fig. 9 show that the state deviations are in a feasible range (with a maximal position deviation of approximately 1.3 mm) when considering only the driven part of the motion.

3.2.3 Influences on the Optimality Criteria

As the proposed *optimization planner* provides an optimal motion with respect to the comfort of the passengers with the minimization of lateral acceleration $\dot{y}^V$, a corresponding comparison is also advisable and is shown in Fig. 10. The maximal value of lateral acceleration normalized to the maximal lateral acceleration developing in case of the *optimization planner* is calculated by the following equation:

$$k_{a_y} = \frac{max(\dot{y}^{V,j}(i))}{max(\dot{y}^{V,opt}(i))}, \tag{28}$$

where $\dot{y}^{V,opt}(i)$ is the lateral acceleration of the i^{th} trajectory in case of the *optimization planner*, and $\dot{y}^{V,j}(i)$ is the lateral acceleration in case of planner j.

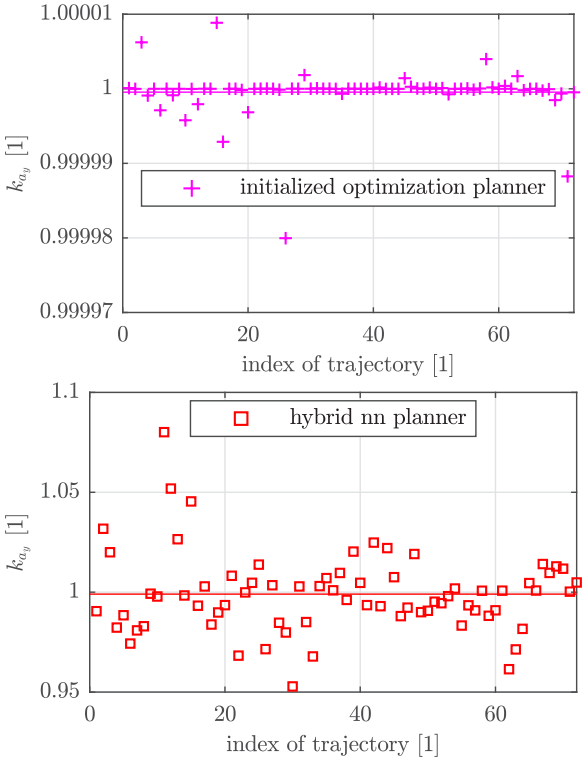

Fig. 10. *Normalized maximal lateral accelerations*

Once again, the performance of the *initialized optimization planner* is virtually the same, as expected. The *hybrid nn planner* produces a maximal increase of approximately 7.85 %, while the average stays around zero deviation. The value of maximal lateral acceleration is even smaller in several cases, which is possible by the violation of the prescribed end configuration.

3.3 Validation of Benchmark Results

As the run-time of the *hybrid nn planner* enables real-time application, the benchmark results for this algorithm were validated with the industrial vehicle simulation software IPG CarMaker to prepare the application on a test car. The examination with a highly accurate, close-to-real environment was important, bacause the benchmark results in Section 3.2 were evaluated using the same single-track vehicle model that is employed in the *optimization planner*, which means that the deviations between the nominal system and a real vehicle due to unmodeled dynamics and changing environment conditions are not considered there.

Fig. 11. *Lane change maneuver in CarMaker*

Fig. 11 shows a lane change maneuver performed by the proposed planner in the CarMaker environment. The virtual test vehicle is chosen as a mid-size passenger car. The main parameters of the chassis (m, θ, l_f, l_r) and the wheels (r_f, r_r, μ_f, μ_r) of the vehicle motion estimator module of the planner were not adjusted exactly to the simulated vehicle to model the inevitable differences between the nominal and the actual systems (e.g. mass depending on the number of passengers).

The CarMaker simulation results on Fig. 12 show that the deviations of the vehicle's final state from the planning target are higher than the ones on Fig. 8 but remain in case of almost every trajectory under a position error of 1 m. The deviation after the time frame necessary for the planning of the following trajectory is typically in a range of a few centimeters as shown in Fig. 13, which is not very small but is still in a feasible range considering that a suitable safety margin is used for collision avoidance.

In terms of the highest lateral acceleration along the planned motion, Fig. 14 even shows an

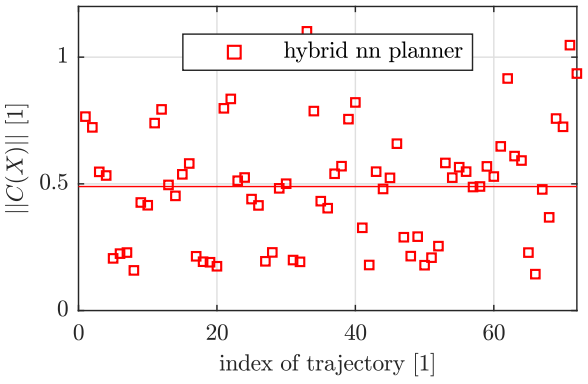

Fig. 12. *Final deviation of vehicle state in CarMaker*

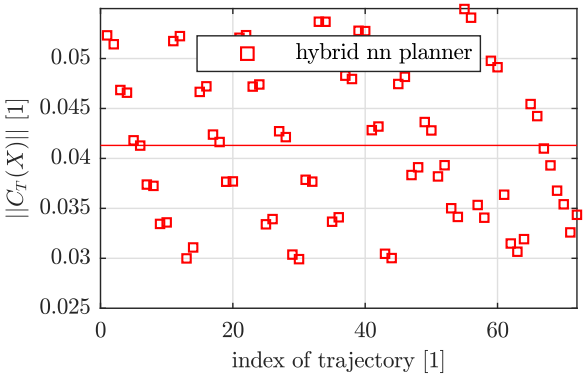

Fig. 13. *Final deviation of vehicle state considering only the driven part in CarMaker*

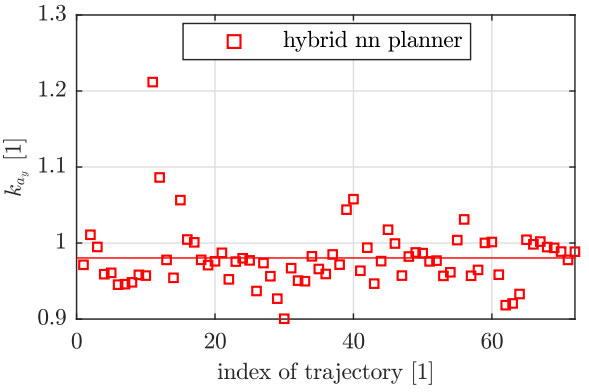

Fig. 14. *Normalized maximal lateral accelerations in CarMaker*

improvement in average. Of course, this is mainly possible due to the violation of the state constraints, but the overall performance is very similar to the one on Fig. 10.

4 CONCLUSIONS AND OUTLOOK

In this paper a nonlinear optimization based trajectory planning algorithm is proposed to generate dynamically feasible, comfortable, and configurable motion for highly automated or autonomous road vehicles with the model-based prediction of the vehicle's motion. The main drawback of the developed approach is the significant computation time, which jeopardizes real-time usage even with a possible move from the current MATLAB based implementation to a faster one, e.g. in C++.

To overcome this issue, two hybrid approaches are suggested with the application of an artificial neural network. Based on a dataset generated off-line with the optimization planner, the network is trained to solve the motion planning problem by the approximation of the optimization planner's behavior. The first method uses the output of the neural network as an initial guess of the optimization process. This halves the run-time of the planning while maintaining the same performance regarding dynamical feasibility and motion optimality. The second algorithm skips the optimization entirely, using the neural network's output directly. The trajectory of the vehicle is calculated with the motion predictor applied in the optimization planner. The plausibility of the network's output is checked by the comparison of the prescribed and actually reached final states, which eliminates the problematic of the neural network being a black-box system. Although there are remarkable differences between the motions planned by the neural network and the optimization process when considering the whole trajectory, the deviations are in a feasible range if only the part of the motion which is meant to be actually driven is dealt with. The significantly decreased computation time can even enable the real-time usage of the proposed hybrid approach.

There are multiple enhancement opportunities of the presented work. Firstly, the performance of the neural network estimator could be examined in case of the usage of more state constraint variables (input variables) as well as a greater magnitude of training data. The behavior of the algorithm should also be investigated in real operating conditions, when it is used as a continuously running motion planning task with a defined output rate to generate interconnected trajectories for long term vehicle motion. Secondly, the current work is not dealing with the generation of a safe emergency motion in case of the neural network generates a highly infeasible solution, which topic is however important for real applicability. Considering that the optimization planner must not be used online, but only to provide the learning samples for the neural

network, an even more accurate twin-track vehicle model could be used to evaluate the trajectories. As the authors are developing the optimization planner to include obstacle avoidance internally in the optimization problem, a corresponding extension of the presented neural network approach would also be an interesting opportunity.

5 ACKNOWLEDGEMENTS

The research reported in this paper was supported by the Higher Education Excellence Program of the Ministry of Human Capacities in the frame of Artificial Intelligence research area of Budapest University of Technology and Economics (BME FIKPMI/FM).

EFOP-3.6.3-VEKOP-16-2017-00001: Talent management in autonomous vehicle control technologies- The Project is supported by the Hungarian Government and co-financed by the European Social Fund.

6 REFERENCES

[1] European Commission Mobility and Transport (2016). Road Safety in the European Union, *from https://ec.europa.eu/transport/road_safety/home_en*, accessed on 2018-10-18.

[2] Mersky, A.C., Samaras, C. (2016). Fuel economy testing of autonomous vehicles. *Transportation Research Part C: Emerging Technologies*, vol. 65, p. 31-48, **DOI:10.1016/j.trc.2016.01.001**.

[3] Chen, Y., Gonder, J., Young, S., Wood, E. (2017). Quantifying autonomous vehicles national fuel consumption impacts: A data-rich approach. *Transportation Research Part A: Policy and Practice*, in press, **DOI:10.1016/j.tra.2017.10.012**.

[4] Tettamanti, T., Varga, I., Szalay, Z. (2016). Impacts of autonomous cars from a traffic engineering perspective. *Periodica Polytechnica Transportation Engineering*, vol. 44, no. 4, p. 244-250, **DOI:10.3311/PPtr.9464**.

[5] Paden, B., Čap, M., Yong, S.Z., Yershov, D., Frazzoli, E. (2016). A survey of motion planning and control techniques for self-driving urban vehicles. *IEEE Transactions on Intelligent Vehicles*, vol. 1, no. 1, p. 33-55, **DOI:10.1109/TIV.2016.2578706**.

[6] Vorobieva, H., Minoiu-Enache, N., Glaser, S., Mammar, S., Mammar, S. (2013). Geometric continuous-curvature path planning for automatic parallel parking. *10th IEEE International Conference on Networking, Sensing and Control*, p. 418-423, **DOI:10.1109/ICNSC.2013.6548775**.

[7] Boryga, M. (2014). Trajectory planning of end-effector for path with loop. *Strojniški vestnik - Journal of Mechanical Engineering*, vol. 60, no. 12, p. 804-814, **DOI:10.5545/sv-jme.2014.1965**.

[8] Minh, V.T., Pumwa, J. (2014). Feasible path planning for autonomous vehicles. *Mathematical Problems in Engineering*, vol. 2014, art. ID 317494, **DOI:10.1155/2014/317494**.

[9] Li, X., Sun, Z., He, Z., Zhu, Q., Liu, D. (2015). A practical trajectory planning framework for autonomous ground vehicles driving in urban environments. *IEEE Intelligent Vehicles Symposium (IV)*, p. 1160-1166, **DOI:10.1109/IVS.2015.7225840**.

[10] Dijkstra, E.W. (1959). A note on two problems in connexion with graphs. *Numerische Mathematik*, vol. 1, no. 1, p. 269-271, **DOI:10.1007/BF01386390**.

[11] Liu, S., Mohta, K., Atanasov, N., Kumar, V. (2018). Search-based motion planning for aggressive flight in SE(3). *IEEE Robotics and Automation Letters*, vol. 3, no. 3, p. 2439-2446, **DOI:10.1109/LRA.2018.2795654**.

[12] Likhachev, M., Ferguson, D., Gordon, G., Stentz, A., Thrun, S. (2005). Anytime dynamic A*: An anytime, replanning algorithm, *The International Conference on Automated Planning and Scheduling*, p. 262-271.

[13] Montemerlo, M., Becker, J., Bhat, S., et al. (2008). Junior: The Stanford entry in the urban challenge. *Journal of Field Robotics*, vol. 25, no. 9, p. 569-597, **DOI:10.1002/rob.20258**.

[14] Jayasree, K.R., Jayasree, P.R., Vivek, A. (2017). Smoothed RRT techniques for trajectory planning. *International Conference on Technological Advancements in Power and Energy*, p. 1-8, **DOI:10.1109/TAPENERGY.2017.8397376**.

[15] Dubins, L.E. (1957). On curves of minimal length with a constraint on average curvature, and with prescribed initial and terminal positions and tangents. *American Journal of Mathematics*, vol. 79, no. 3, p. 497-516, **DOI:10.2307/2372560**.

[16] Arslan, O., Berntorp, K., Tsiotras, P. (2017). Sampling-based algorithms for optimal motion planning using closed-loop prediction. *IEEE International Conference on Robotics and Automation*, p. 4991-4996, **DOI:10.1109/ICRA.2017.7989581**.

[17] Howard, T. M., Kelly, A. (2007). Optimal rough terrain trajectory generation for wheeled mobile robots. *The International Journal of Robotics Research*, vol. 26, no. 2, p. 141-166, **DOI:10.1177/0278364906075328**.

[18] Ferguson, D., Howard, T. M. Likhachev, M. (2008). Motion planning in urban environments: Part I. *IEEE/RSJ International Conference on Intelligent Robots and Systems*, p. 1063-1069, **DOI:10.1109/IROS.2008.4651120**.

[19] Li, B., Shao, Z. (2015). A unified motion planning method for parking an autonomous vehicle in the presence of irregularly placed obstacles. *Knowledge-Based Systems*, vol. 86, p. 11-20, **DOI:10.1016/j.knosys.2015.04.016**.

[20] Yang, S.X., Meng, M. (2001). Neural network approaches to dynamic collision-free trajectory generation. *IEEE Transactions on Systems, Man, and Cybernetics, Part B (Cybernetics)*, vol. 31, no. 3, p. 302-318, **DOI:10.1109/3477.931512**.

[21] Liu, L., Hu, J., Wang, Y. Xie, Z. (2017). Neural network-based high-accuracy motion control of a class of torque-controlled motor servo systems with input saturation. *Strojniški vestnik - Journal of Mechanical Engineering*, vol. 63, no. 9, p. 519-528, **DOI:10.5545/sv-jme.2016.4282**.

[22] Engedy, I., Horvath, G. (2009). Artificial neural network based mobile robot navigation. *IEEE International Symposium on Intelligent Signal Processing*, p. 241-246, **DOI:10.1109/WISP.2009.5286557**.

[23] Qu, H., Yang, S.X., Willms, A.R., Yi, Z. (2009). Real-time robot path planning based on a modified pulse-coupled neural network model. *IEEE Transactions on Neural Networks*, vol. 20, no. 11, p. 1724-1739, **DOI:10.1109/TNN.2009.2029858**.

[24] Janglová, D. (2004). Neural networks in mobile robot motion. *International Journal of Advanced Robotic Systems*, vol. 1, no. 1, p. 15-22, **DOI:10.5772/5615**.

[25] Tai, L., Paolo, G., Liu, M. (2017). Virtual-to-real deep reinforcement learning: Continuous control of mobile robots for mapless navigation. *IEEE/RSJ International Conference on Intelligent Robots and Systems*, p. 31-36, **DOI:10.1109/IROS.2017.8202134**.

[26] Plessen, M.G. (2017). Automating vehicles by deep reinforcement learning using task separation with hill climbing. *CoRR*, vol. abs/1711.10785.

[27] Velagic, J., Osmic, N., Lacevic, B. (2008). Neural network controller for mobile robot motion control. *International Journal of Electrical and Computer Engineering*, vol. 2, no. 11, p. 2471-2476.

[28] Gorinevsky, D., Kapitanovsky, A., Goldenberg, A. (1996). Neural network architecture for trajectory generation and control of automated car parking. *IEEE Transactions on Control Systems Technology*, vol. 4, no. 1, p. 50-56, **DOI:10.1109/87.481766**.

[29] Yim, Y., Oh, S.-Y. (2004). Modeling of vehicle dynamics from real vehicle measurements using a neural network with two-stage hybrid learning for accurate long-term prediction. *IEEE Transactions on Vehicular Technology*, vol. 53, no. 4, p. 1076-1084, **DOI:10.1109/TVT.2004.830145**.

[30] Bellem, H., Schönenberg, T., Krems, J.F., Schrauf, M. (2016). Objective metrics of comfort: Developing a driving style for highly automated vehicles. *Transportation Research Part F: Traffic Psychology and Behaviour*, vol. 41, p. 45-54, **DOI:10.1016/j.trf.2016.05.005**.

[31] Hegedüs, F., Bécsi, T., Aradi, S. (2017). Dynamically feasible trajectory planning for road vehicles in terms of sensitivity and robustness. *Transportation Research Procedia*, vol. 27, p. 799-807, **DOI:10.1016/j.trpro.2017.12.110**.

[32] Hegedüs, F., Bécsi, T., Aradi, S., Gápár, P. (2017). Model based trajectory planning for highly automated road vehicles. *IFAC-PapersOnLine*, vol. 50, no. 1, p. 6958-6964, **DOI:10.1016/j.ifacol.2017.08.1336**.

[33] Pacejka, H.B. (2012). Chapter 8 - Applications of transient tire models. Pacejka, H.B. (ed.) *Tire and Vehicle Dynamics (3rd ed.)* p. 355-401, Butterworth-Heinemann Oxford, **DOI:10.1016/B978-0-08-097016-5.00008-5**.

Strojniški vestnik - Journal of Mechanical Engineering 65(2019)3, 161-180

DOI:10.5545/sv-jme.2018.5788 Original Scientific Paper
Received for review: 2018-10-11
Received revised form: 2019-01-23
Accepted for publication: 2019-01-28

Active Structural Derivator in the Design Crystallization Phase of L7e Vehicle Structures

Roman Pawel Jedrzejczyk* – Michael Sigmar Alb
Virtual Vehicle Research Center, Austria

Over the past years, engineers have begun to apply topology optimization (TO) to obtain the first design proposals for new structures. Consequently, designers need to transform the bionic shapes of the TO results into manufacturable geometry that employs the available body-in-white structure types (BSTs) and affirms the efficient and suitable lightweight design. The lack of standardized methodologies, however, forces designers to transform the bionic shapes of the TO subjectively, which results in insufficient and inadequate design proposals. Many different separate geometrical transitions that attempt to transform the TO results into the one of the selected BSTs make the design process even more difficult to manage. For this reason, we have proposed the active structural derivator (ASD) as an extension of our existing integrative CAE-driven design process (ICDDP). The ASD allows for the smooth transition of the TO results and the practical assessment of the selected BSTs such as tubular space frame, space frame, hybrid structure, unibody and monocoque. Our ASD simultaneously employs the size and free-size optimizations under the specific steering criteria within one simulation model, which consists of fundamental engineering-based geometry (beams and plates), to generate the design concepts of the different BSTs for given sets of different requirements. We present the results of our ASD for the new structure of an electrified eQuad vehicle that reveal the ASD's ability to select, allocate and optimize various beam types (arbitrary and defined) together with the plate (shell) geometry. The results assert that the ASD enables engineers to deliver new applicable and lightweight structures.

Keywords: bionic geometry, body-in-white, design process, FEM, free-size optimization, ICDDP, topology optimization, size optimization, vehicle structure design

Highlights

- *ASD makes possible the smooth transition of the TO results into one of the selected BSTs.*
- *ASD assesses the load-bearing characteristics such as compression-tension, bending and torsion of these structures.*
- *ASD entitles designers to direct comparisons between the various obtained designs of the BSTs and indicates the loads (load cases) with the highest compliance (inverted structural stiffness).*
- *ASD permits the calculations for composite materials and system identifications.*

0 INTRODUCTION

In recent years, the mechanical engineering industry has experimented with methods that unify a systematic approach to the design process and support of computer-aided-engineering (CAE) tools. These methods mainly utilize topology optimization (TO) in many development studies of new structures [1] and [2]. As a result, the TO delivers bionic shapes of new structures that need to be translated into manufacturable geometry. This transition from a bionic model to geometric solutions has not been fully defined because the bionic shapes challenge a coherent and qualitative interpretation [3]. Such interpretation should take full advantage of reasoning material application [4], which is suggested by the TO results. Consequently, the transition of bionic shapes to a new structure can be performed by employing three-dimensional (3D) printing technologies [5] or by deriving a new structure from the bionic results that is traditionally manufactured.

New lightweight structures can now be printed out in various 3D printers for different material types, including metal alloys [5] and [6]. Such manufacturing processes offer an opportunity to examine a functional prototype earlier, check a proper design accurately and bring a final product faster to the market [7]. Additionally, rapid manufacturing methods deliver spare parts for unique mechanisms as well as demonstrators for new product ideas [6]. Although the usage of 3D printing technologies is growing rapidly, these technologies also have downsides [6] and [7] such as necessary additional preparation of bionic geometry for 3D printers, high costs of metallic powders, expensive small dimensional 3D printers, inferior geometric dimensioning and tolerancing. Moreover, 3D printing is improper for structures that exhibit modular scalable constructions (e.g. automotive industry). These facts limit the practical applications of 3D printing technologies to narrow manufacturing areas.

The bionic model can also be transitioned into a traditionally manufactured structure. This transition,

*Corr. Author's Address: Virtual Vehicle Research Center, Inffeldgasse 21a, 8010 Graz, Austria, RomanPawel.Jedrzejczyk@v2c2.at

however, is subjective because designers and engineers interpret the bionic shapes by assessing the TO results individually. In consequence, designers and engineers need to develop one or select from a few unstandardized methods [8] to perform the bionic shapes' transition reasonably. Thus, the new developed structures exhibit a poor and inadequate lightweight design.

1 ACTIVE STRUCTURAL DERIVATOR

1.1 Designing Vehicle Structures

Engineers derive a new vehicle structure from a bionic model by applying selected body-in-white structure types (BSTs). This approach can privilege or even restrict lightweight design of new structures frequently [9]. Recent studies have exemplified that specific BSTs favor lightweight design more than others [9] to [12]. A body-in-white (BIW) of a mid-range sedan, for example, has the same weight (ca. 188 kg) for an aluminum space frame and an aluminum unibody; however, the capable production volumes and possible production costs are significantly different, thus restricting an aluminum space frame BST to low production volumes.

Not only improper applied BSTs can be expensive. Omitting the pieces of a new structure that was insufficiently translated from the TO results into a geometrical engineering model influences the load-bearing capabilities of such structures crucially. To enhance a newly designed structure, engineers apply extra structural optimization [13] and [14] design steps, consequently increasing the overall product development duration.

To target the individual needs of new vehicle customers more directly [15], the number of model derivatives offered by vehicle manufacturers has increased markedly. Designers should assess whether or not a design of model derivatives matches new specifications [16] and [17] by carrying out extra analyses (e.g. system identification). In addition, the 18-month development cycles restrict a number of feasible design studies for a new structure to only a few [18]. Thus, possible lightweight actions of a new design such as new material types, different BSTs and sandwich material types are expensive to apply in the later phase of the development process, which influences the final price of new vehicles [19].

Optimization technologies support the development process notably [20] and [21], but the lack of rapid method-ology to analyze available BSTs for a new vehicle model and almost 40 different CAE tools present in the automotive industry [8] hinder possible cost estimations of such technologies' introductions to a current development and handicap engineers to distinguish between the suitable BSTs that are equal to the lightweight design yet challenging in production know-how [22] and [15]. Moreover, engineers demand that an innovative method selects, allocates and optimizes fundamental structural elements (beams and plates) within one simulation model and allows for fast geometrical updates and the modulization of similar structures [22].

For these reasons, the design method that allows engineers to transform the bionic shapes into geometrical engineering-based models is presented in this paper. Our active structural derivator (ASD) enables designers to reveal the omitted extra details of the translated geometry so that their presence in a new structure can be further analyzed and optimized during the execution of the ASD. The term derivator, in fact, is adopted from mathematics, where it serves to refine and in a certain sense simplify the theory of homotopical algebra [23]. The ASD permits engineers to investigate various configurations of the BSTs such as tubular space frame, space frame, unibody, hybrid structure and monocoque for a new vehicle structure. For the various configurations of the different structure types, the ASD enables designers to assess several arrangements of diverse materials such as isotropic and orthotropic (e.g. steel, aluminum, composites and sandwich composites).

The ASD also offers a possibility to select, allocate and optimize the fundamental structural elements (beams and plates) for a newly designed structure. This method distinguishes between assorted types of beam cross-sections such as arbitrary and defined (e.g. box, rod) cross-sections that can be used together with the plate geometry in the analysis of the available BSTs. The ASD exhibits the character of acting loads in such a way that designers can adequately select the beam types to accommodate better tension-compression, bending and torsion loads. Consequently, the ASD highlights an influence of the plates (shells) geometry on the load-bearing capabilities of a new design structure. The ASD also contrasts the loads and load cases that have an impact on the structural stiffness of new structures and require improvements in the design. More importantly, the ASD makes all of these benefits possible within one FE model (FEm).

Our work illustrates the ASD for a real use case that proposes a new structure design for an electric-driven L7e vehicle. The ASD provides valuable concepts of a new structure with great potential for

a lightweight design, adequate stiffness and useful suggestions for the structure type best suited to the acting loads. These examples of new eQuad structure proposals demonstrate the universal character of the ASD that can be employed to design new structures in numerous fields of mechanical engineering such as the aerospace, automotive, light and heavy machinery, rail industries.

1.2 Extracting Requirements for the ASD

The mechanical and automotive industries are currently postulating the need for a design method that minimizes the number of vehicle prototypes (or even eliminates prototyping test stages) and delivers robust design verification [19], [24] and [25]. Consequently, these industries also require an approach that permits engineers to build the first concept models with the reduced utilization of computer-aided-design (CAD) tools and apply optimization technologies during the stages of product development so that the development process of a new vehicle becomes completely virtual.

To cope a current systematic approach (which consists of four main phases [26] and [27] such as (1) planning and task clarification, (2) conceptual design, (3) embodiment design, and (4) detail design,) for the design process of a new part or item with simulation technologies, Sellgren [28] postulated a simulation-driven design process (SDDP). The SDDP supports the design process by providing required pieces of information from modeling and simulation techniques. This profitable input allows engineers to reduce work time to acceptable levels and allows for earlier design changes during the development process. The SDDP, however, offers any opportunity to discuss available BSTs.

Engineers search for a design method that allows for innovative and optimal design solutions of available BSTs. Osborne et al. [29] presented the idea for a meth-od of vehicle concept designs. This approach utilizes simple geometrical elements such as beams and plates to describe the rough geometry of a new vehicle structure. In addition, such a rough defined model enables designers to collect engineering data: inertia components, principle force values, rigid body analysis, etc. Although engineers can obtain a rough geometrical description of a new structure, this approach considers no possible way of transition for the geometrical models of bionic shapes. Moreover, this approach demonstrates a lack of optimization technologies that allows for the consideration of a suitable BST.

Compared to Osborne's idea, Steinwall and Viippola [30] demonstrated a design method that combines optimization technology and modern product development. This method applies simulations, optimizations (including TO) and CAD tools to the trial and error design process of a new structure. However, this approach restricts contemporary studies of potential BSTs and different material types within one model with the multiple iterations. Therefore, the changes in the design provoke the actualization of the base line model that adds the extra design iterations. Nevertheless, the transition of bionic shapes into a geometrical model is treated insufficiently, resulting in the difficult enhancement of geometrical models.

Each designer requires that a CAE method transforms bionic TO results into engineering-based models. Baskin el al. [31] proposed a design method that attempts to transform the bionic shapes of TO results into beam-based geometrical models. The beam-based models are further improved to shell-based models with the adaptation of hand-determined beam sections. TO is applied for the generation of load paths. Consequently, other optimization technologies are utilized upon request to optimize one explicitly defined type of the BIW. As a result, the explicitly defined BST prevents simultaneous consideration of the various BSTs in this method. Nonetheless, this approach discloses a lack of examination for different material types such as composites and sandwiches. Moreover, this method provides no opportunity to select, allocate and optimize arbitrary beams together with plate-based geometry.

1.3 Description of the ASD

We propose the ASD method as an extension of our Integrative CAE-driven design process (ICDDP), published earlier in [32]. The ICDDP works as a framework for the ASD and this ICDDP is divided into three essential engineering phases of a new structure design: conceptual design, design crystallization and design sophistication (Fig. 1). Fig. 1 demonstrates the application area of our ASD within the ICDDP. Fig. 1 also depicts the main steps and phases of the ICDDP together with the detailed view of design, modeling and calculation techniques. For each step, there are specified inputs, tasks to perform and defined tools (including optional tools) to apply.

The design sequences of the ICDDP and the ASD employ only one simulation software package (Altair OptiStruct®) that supplies the necessary simulation and optimization methods. It is possible to incorporate other types of software for the ICDDP and ASD if

they are requested. The main steps and design phases of the ICDDP as well as the ASD are universal and to execute them, the other types of software that provide crucial simulation and optimization methods – either partially or all within one software environment – can also be utilized.

As a result of the TO, the bionic shapes of new structures need to be translated into one of the available and selected BSTs. Engineers utilize beams and plates (shells) to represent the fundamental engineering geometry that constitutes all available BIWs. For this reason, our ASD utilizes these fundamental structural elements to deliver new structure concepts. Comparing different types of BIWs, one can assess the qualitative concentration of these fundamental structural elements through available BSTs. Table 1 summarizes the concentration of the available BSTs. This comparison is based on the definitions of the available BSTs [9] to [12], visual assessment of qualitative fundamental geometry and its dominant geometrical shapes.

In fact, Table 1 affirms the domination of one fundamental structural element over the others for the specific BST, e.g. beams over plates for an aluminum space frame (ASF). Consequently, we assumed that the investigation of the available BSTs requires simultaneous analysis and optimization for beams and plates within one calculation-simulation model.

To perform such investigation of the available BSTs, the ASD depends upon the layout and its criteria that steer this investigation. Fig. 2 shows that the definition of the available BSTs is influenced by the economic, materials and manufacturing constraints. These three groups of constraints determine the main characteristics of the available BSTs. This observation, for example, can be noticed for the tubular space frame and space frame where the main differences result from the applied materials (steel versus aluminum), production quantity and joining technology (aluminum requires the more sophisticated approach). Despite these fundamental differences, industries also utilize the space frame design for the structures made of steel [9] to [12].

Table 1. *Qualitative distribution of the BIW fundamental engineering structural elements*

BIW types	1D – beams	2D – plates	BIW types	1D – beams	2D – plates
TSF	High	Low	SU	Low ÷ med.	High
SSF	High	Low ÷ med.	AU	Med.	High
ASF	High	Low ÷ med.	CM	Low	High
BOF	Med. ÷ high	High	HS	Low ÷ high	Low ÷ high

Where: TSF – tubular space frame; SSF – steel space frame; ASF – aluminum space frame; BOF – body-on-frame; SU – steel unibody; AU – aluminum unibody; CM – composite monocoque; HS – hybrid structure; Med. – medium

Considering the distribution of the fundamental engineering geometry (beams and plates) [9] to [12], one can define the prioritizing of such geometrical

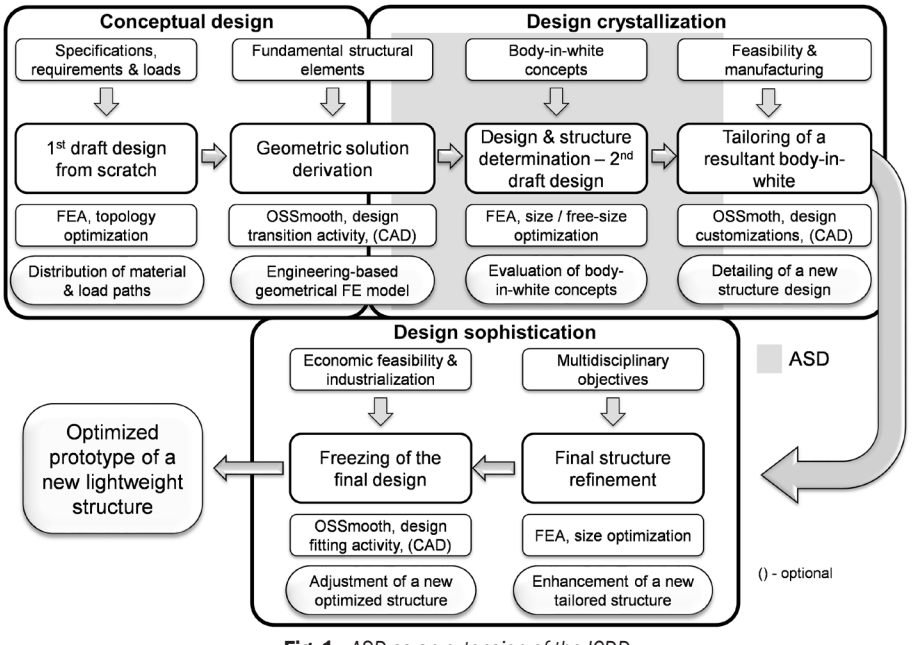

Fig. 1. *ASD as an extension of the ICDD*

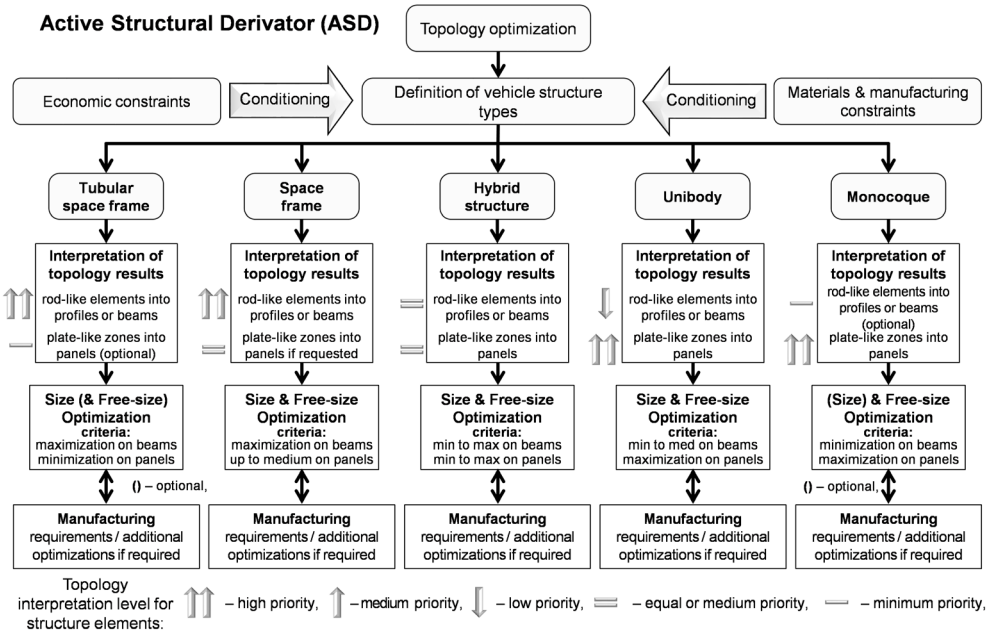

Fig. 2. *Steering criteria for the ASD and the applied optimization techniques*

elements for an FEm obtained from the geometric solution derivation step (Fig. 2). This prioritizing actually constitutes the steering criteria of the ASD by maximizing and / or minimizing the load-bearing intensity for one of the fundamental geometrical elements. Additionally, the ASD provides the opportunity to include special manufacturing requirements that take into account joining technology, testing of lightweight materials (e.g. sandwich composites) as well as extra optimization runs (to reveal more detailed optimization results) if required (Fig. 2).

Table 2. *Steering methodology for the ASD*

BIW structure types	Optimization methods	Prioritizing for 1D elements	Prioritizing for 2D elements
Tub. space frame	SO (/FSO)	Maximization	Minimization
Space frame	SO / FSO	Maximization	Up to medium
Hybrid structure	SO / FSO	Min to max	Min to max
Unibody	SO / FSO	Min to med	Maximization
Monocoque	FSO (/SO)	Minimization	Maximization

Where: BIW – body-in-white; Tub. – tubular; SO, FSO – size and free-size optimization, respectively; (/*) – optimization upon request; Min – minimization; med – medium; max – maximization

The main idea behind the steering methodology is to obtain a BST selected by influencing the load distributions throughout the load-bearing profiles and plates and picking the useful optimization methods or a combination thereof (Fig. 2). Table 2 demonstrates the steering methodology for the ASD. For the reason of simplicity, we chose five different BSTs - tubular space frame, space frame, hybrid structure, unibody and monocoque - to highlight the ASD methodology.

The steering methodology of the ASD utilizes two optimization methods to satisfy the load-bearing capabilities of a new structure by prioritizing the distribution of acting loads throughout the one dimensional (1D) and/or two dimensional (2D) geometrical engineering elements. Thus, the steering methodology sets the limits for the applications of fundamental engineering geometry.

We investigated the ASD by holding this discussion for the real use case of a new eQuad structure. The employment of the ASD raises the following questions regarding the embodiment design phase:

- How can the load-bearing be indicated throughout the arbitrary and defined beams of a new structure to provide knowledge about the tension-compression, bending and torsion loads?
- Is it possible to select, allocate and optimize various beam types together with the plate (shell) geometry for the different BSTs such as tubular space frame, space frame, hybrid structure, unibody and monocoque?
- How can the influence of the plate (shell) geometry be assessed for the load-bearing

capabilities of a new structure that consists of beams and plates?
- How can the bionic TO results be transitioned into manufacturable geometry that exploits the design suggestions of the TO efficiently?
- How should an optimized FEm be prepared to discuss and analyze the different BSTs for a new structure design within one FEm?
- How can the ASD be executed to deliver different proposals for the available BSTs of a new eQuad structure?
- Is it possible to consider the composite and sandwich-composite materials for the ASD of the available body-in-white structure types?
- How can the load cases be revealed that influence mostly the structural stiffness of a new structure and advise about improvements in design concepts?

The next sections provide the answers to the above-listed questions.

2 APPLICATION OF THE ASD

To take full advantage of beam and plate (shell) elements in a new structure, engineers need to know the distribution of the load-bearing throughout all beam elements of a new structure. This section examines the arbitrary and defined beams, their combinations with plate (shell) geometry, a system identification for such combinations, and composite materials for plate geometry with the conjunction of the arbitrary and defined beams. To understand the ASD results of five picked BSTs (Section 2.2) for a new L7e vehicle structure, one needs to test this ASD method on a small scale (Section 2.1) to enlighten the relationship between the beams and plates (shells).

2.1 Beams and Plates as a Fundament to Understand the ASD

2.1.1 ASD - Universal Design Approach for Arbitrary and Defined Beams

We proposed the universal design approach (UDA), which is also one of the ASD design steps, for arbitrary and defined beams that delivers the load-bearing's distribution and allows for the optimization of the selected beam elements. The box beams were selected as a special case of the arbitrary beams to demonstrate the capabilities of the UDA for the defined beam types and because the box cross-sections are characterized, compared to other cross-sections with the constant area, by the highest buckling stiffness, a great section modulus for bending and a significant section modulus for torsion loads [33]. The box cross-section offers flat surfaces that allow for easier packaging and connections of additional accessories and attachments.

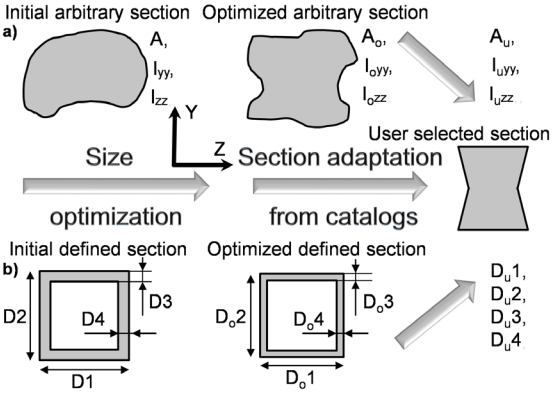

Fig. 3. *ASD – universal design approach for a) arbitrary, and b) defined beams*

Fig. 3 illustrates our UDA methodology for arbitrary (Fig. 3a) and defined (Fig. 3b) beams. A, A_o, A_u, Iyy, Izz, I_oyy, I_ozz, I_uyy, I_uzz are the cross-sectional areas and second moments of area for initial, optimized and user-selected arbitrary beam cross-sections, whereas D1, D2, D3, D4, D_o1, D_o2, D_o3, D_o4, D_u1, D_u2, D_u3, D_u4 are the dimensions of the initial, optimized and user-selected for a defined beam cross-section (e.g. box, channel), respectively. The beams of the UDA can be modeled with different isotropic materials such as steel, aluminum and titanium.

The UDA offers two ways to optimize the beam elements and collect essential distribution of beams' load-bearing capabilities. The first general way (Fig. 3a) employs the arbitrary beams that provide the values of the cross-sectional areas and second moments of area (for both principal cross-sectional coordinate axes) after the optimization run. As the cross-sectional parameters are independent for the arbitrary beams, the value of the cross-sectional areas indicates the changes in tension-compression loads and the second moments of cross-sectional area indicates bending and torsional loads. Designers applying the size optimization (SO) [34] and [35] that optimizes the properties (e.g. length, diameter, height, width) of structural elements to provide required solutions obtain the optimized values of the cross-sectional areas and second moments of area. These values of the arbitrary beam cross-sectional parameters serve to select the real beam cross-sections. Consequently, engineers can select the real beam cross-sections that

bear the acting load sufficiently and grant specific requirements given. This selection matches the optimized cross-sections to the real cross-sections from industrial profile catalogs [36] and [37], which can also be new or the preferred one.

The second detailed way (Fig. 3b) makes use of beam elements with the defined cross-sections. As a result of the SO, the user achieves the cross-sectional dimensions that represent a concrete defined beam cross-section (e.g. box, channel). The values of the cross-sectional dimensions for a defined cross-section communicate the distribution of the load-bearing less simply due to the functional relationship between these cross-sectional dimensions. This inconvenience overcomes the possibility of adopting the beam cross-sections directly from industrial profile catalogs [36] and [37], which helps designers deliver new structure concepts more rapidly and efficiently.

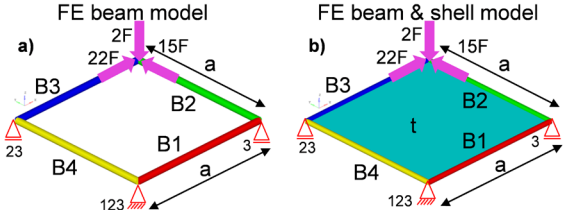

Fig. 4. *ASD – FEms: a) beams, b) beams and shell*

We prepared the FE beam model for the arbitrary and defined box beam cross-sections (Fig. 4a) to test the UDA methodology. The FE beam model (Fig. 3a) consisted of four beam elements (called B1 to B4) with the length a = 100 mm and these four beams were made of steel (Table 3). Three forces that act in three principal axial directions (x, y, z), with the values F = 1 kN multi-plied by corresponding factors such as x = 22, y = 15 and z = 2, were applied to this FEm (Fig. 4). The FEm was constrained to the ground by blocking the relevant degrees of freedom (xyz, yz, and z) in the frame's corners.

The optimization runs were conducted in this work for the constrained values of displacements and the function to minimize was volume or total volume, respectively. The authors of this work tested the UDA for the arbitrary and defined beams by optimizing the FE beam model for the given intervals of the cross-sectional parameters (A is 1.96 mm^2 to 66.0 mm^2; Iyy, Izz 7.8465 mm^4 to 1355.8 mm^4) and dimensions (D1, D2 5 mm to 12.5 mm; D3, D4 0.1 mm to 1.5 mm). The displacements were limited in the point of the force applications to x ≤ 11.0 mm, y ≤ 0.55 mm, and z ≥ -5.95 mm and the values were specially selected to highlight the optimization process.

Table 3. *Material properties for the optimization runs*

Material	ρ [kg/mm^3]	E [GPa]	υ [-]
Steel	7.85e-06	210.0	0.30
Q-I CFRP	1.60e-06	78.0 / 78.0	0.06 / 6.5
Balsa wood	9.7e-08	0.4 / 0.4 / 0.2	0.085
Structural foam	1.05e-07	0.11 / 0.11 / 0.2	0.021
Q-I CFRP – Quasi-isotropic carbon fiber reinforced plastics			

2.1.2 *Conjunction of the Plates (Shells) and UDA for Beams*

In this case, the objective was to assess if and how the additional geometry influences the results of the UDA for beams. The additional objective was to reveal an impact of the plate (shell) geometry on the structure's load-bearing capabilities.

For this purpose, we added the square plate made of steel (Table 3) with dimension a = 100 mm and thickness t = 4 mm to the FE beam model (Fig. 4b). Different isotropic and orthotropic materials can also be applied to model this plate. The plate was optimized together with beams simultaneously by applying free-size optimization (FSO) and SO [34] and [35] to the whole FEm. The FSO optimizes the thickness of each single finite element for the plate (shell) geometry.

Three different cases were examined for the FEm of the beams and plate (Fig. 4b). The first case had the cross-sectional parameters (A is 1.96 mm^2 to 66.0 mm^2; Iyy, Izz 7.8465 mm^4 to 1355.8 mm^4) and dimensions (D1, D2 5 mm to 12.5 mm; and D3, D4 0.1 mm to 1.5 mm). The second case had the smaller intervals of the cross-sectional parameters (A is 1.96 mm^2 to 36.0 mm^2; Iyy, Izz 7.8465÷492.0 mm^4) and dimensions (D1, D2 5 mm to 10 mm; D3, D4 0.1 mm to 1.0 mm) than the first case. The third case differentiated only the allowable resultant displacements of the optimization (x ≤ 2.0 mm, y ≤ 0.55 mm, and z ≥ -5.0 mm) from the first case.

2.1.3 *Conjunction of the Plates (Shells) and the UDA for Beams – System Identification*

The system identification was conducted for the joined FEm consisting of the plate and beams (Fig. 4b). The aim of this investigation was to test if the joined FEm can deliver the system identification that assesses a system for specific sets of system constraints established narrowly.

For this purpose, we explored the system identification for the joined FEm by performing the SO and FSO simultaneously. The joined FEm for the system identification had the cross-sectional parameters (A is 1.96 mm^2 to 66.0 mm^2; Iyy, Izz =

7.8465 mm^4 to 1355.8 mm^4) and dimensions (D1, D2 5 mm to 12.5 mm; D3, D4 0.1 mm to 1.5 mm) but the displacements corresponding to the location of the force applications were more restrictive: $1 \leq x \leq 3$ mm, $0.55 \leq y \leq 0.65$ mm, and $-7.5 \leq z \leq -5$ mm. The plate thickness t was equal to 4 mm.

2.1.4 Conjunction of the plate made of composite material and UDA for beams

To check if the conjunction of the plate and UDA for beams works properly for composite materials, the authors of this work investigated the joined FEm (Fig. 4b) with a plate made of the quasi-isotropic carbon fiber reinforced plastic (CFRP). The quasi-isotropic $[0/45/-45/0]_2$ CFPR laminate was prepared in the HyperLaminate® software from Altair® using the values for the single woven ply of CFRP material (Table 3) [38] and [39]. The thickness t was 4 mm and the cross-sectional parameters (A is 1.96 mm^2 to 66.0 mm^2; Iyy, Izz 7.8465 mm^4 to 1355.8 mm^4) and dimensions (D1, D2 5 mm to 12.5 mm; D3, D4 0.1 mm to 1.5 mm), yet the displacements were limited in the point of the force applications to the values of $x \leq 4$ mm, $y \leq 0.55$ mm, and $z \geq -8$ mm.

2.2 ASD – A New Structure for the eQuad

Our ASD is expected to deliver several possible design proposals for a new vehicle structure. For this reason, the ASD was tested on a large scale for an electrified L7e class vehicle called eQuad. The eQuad (Fig. 5) is a quadricycle vehicle that VIRTUAL VEHICLE Research Center adopted and further developed into the full electric-driven quad [40] and [41].

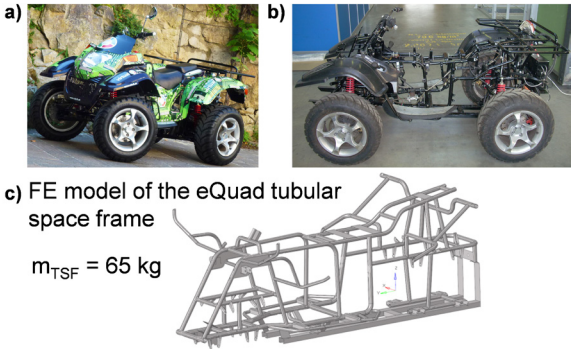

Fig. 5. *Fully electric quadricycle – eQuad: a) complete vehicle, b) tubular space frame, c) FEm of the current vehicle tubular space frame*

The electric power provides the lithium-ion electric batteries to the electric engine. During the adaptation work, the research center converted the original tubular space frame to accommodate the components of the electric powertrain by applying the conversion design approach. The vehicle is capable of reaching 45 km/h and traveling a distance of 30 km. The vehicle is rated for the maximal permissible laden weight of 550 kg including two occupants and luggage; the total mass of the vehicle tubular space frame, which includes the lug-gage rack, brackets for the powertrain and body styling covers, is 82 kg. Fig. 5c displays the FEm of the current eQuad tubular space frame that exemplifies only the fundamental BIW of the eQuad and it weighs 65 kg.

2.2.1 ASD – Geometric solution derivation step for TO results

The ASD requires a geometrical FEm to discuss the various BSTs. The geometrical FEm was obtained by utilizing the geometric solution derivation step of the ICDDP that allows engineers to translate the TO results [32] from the conceptual design phase of the ICDDP.

Fig. 6 exhibits the geometric solution derivation step for the transition of the bionic TO results (Fig. 7a). The transition process starts with the identification of the most visible load paths and material distributions with the densities near 1.0 that form the lines of the force flows (Fig. 7b). Knowing the load paths and material distributions, engineers assess the characteristics of acting loads in the resultant design proposals by identifying shear fields and tension-compression areas [32].

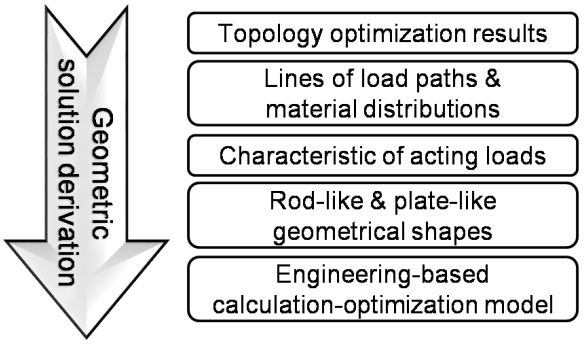

Fig. 6. *Geometric solution derivation step for the transition of the bionic TO results*

Additionally, the lines of the load paths and material distributions help to recognize the rod-like and plate-like geo-metrical shapes from the bionic TO results. This recognition results in the geometrical transition of the bionic TO results into an engineering-

based calculation-optimization model that consists of beam-like and plate-like geometrical engineering elements (Fig. 7c). The geometric solution derivation step can be performed in any aided engineering software that contains basic functions of 3D modeling.

2.2.2 ASD – 1D-2D FEm

The geometric solution derivation step delivered the calculation-optimization FEm (Fig. 7c) of a new structure to the ASD. Fig. 7c presents the 1D-2D FEm of a new structure design for the eQuad. The 1D-2D FE model for the ASD consisted of the beam (1D) and shell (2D) elements. The beam elements of this 1D-2D FEm allowed for the different cross-sections: defined and arbitrary. The material model MAT1 was selected to describe the linear, temperature-independent, isotropic material properties of the FEm geometry that is made of steel (Table 3).

The steel material was chosen due to its higher strength to density ratio and better stiffness to weight ratio than aluminum and magnesium (i.e. in the case of high-strength steels) [42]. These steels can also be paired with other materials to deliver modern hybrid and innovative multi-material designs [43]. The economic ad-vantages of the manufacturing process favor steels [44] over other materials. More importantly, the steel simplifies the simulation-optimization process compared to the composites, while at the same time offering similar stiffness, allowing for the generalization described in the previous work [32].

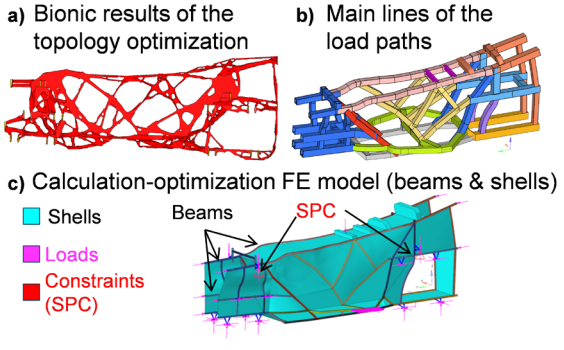

Fig. 7. *Preparation of the 1D-2D FE model for the ASD*

The same loads were applied as they were prepared for the conceptual design phase of a new structure [32]. These loads consider different load scenarios such as static, driving and crash situations that result in 19 different load cases. The prepared load cases define the forces for: vertical bending, front and rear torsion, front and rear braking, cornering, front and rear vertical bumps, bending for front and rear axles, and equivalent static front, rear and side crashes.

The values of these defined forces were obtained by applying a first-order model approach [45] that allows for analyses of what-if questions during the early design phase. We established the additional equations for the models of the first-order approach that calculate the forces for the short-long-arm suspension type under driving conditions. The calculated forces of driving conditions took into account the dynamic behavior with the additional coefficients [45]. The forces obtained were put onto the attached points of the vehicle suspension. A work-energy balance approach [45] was utilized to determine the acting forces for the equivalent static crash load cases. Furthermore, the forces for the bending and torsion load cases were determined by executing the FE analyses for the original structure of the eQuad [46]. We executed the FE simulations for the complete FE eQuad model with the original space frame to assess the vehicle behavior during accidents [46].

The 1D-2D FEm (Fig. 7c) employed the inertia relief approach [34] and [35] to enhance optimization convergence and simulation stability in the case of unconstrained structures. The optimization runs of the all ASD cases minimized the total volume function while the optimization constraints set the optimization domain, limiting the maximal displacements corresponding to the forces from the defined load cases.

We estimated the values of these displacements by conducting the additional FE linear simulations and extracting the displacements from the realized finite element analyses (FEA) [46]. In the case of the crash loads, the displacements were adjusted by allowing larger de-formations so that the other loads could influence the optimization results more evidently.

42 different beams and 22 shell components were specified to define the geometry of the 1D-2D FEm for a new eQuad structure. This frame-shell FEm contained 80 optimization constraints on the resultant displacements; the design variables were 126 (127 for FEm with shells) for the beams with the arbitrary cross-sections and 168 (169 for FEm with shells) for the beams with the defined box cross-sections.

2.2.3 ASD – The Tubular Space Frame

A vehicle tubular space frame is the structure that consists of joined together (mostly welded) tubes or pro-files, different in size and dimensions. The

presence of plate (shell)-like geometry is limited to a minimum and accommodates the packaging purposes.

For this reason, the shell geometry was excluded from the 1D-2D FEm, thus allowing for maximal prioritizing of 1D elements. The cross-sectional parameters and dimensions varied for the arbitrary beams: A 0.44 mm^2 to 896 mm^2, Iyy, Izz = 0.0895 mm^4 to 470,700 mm^4 and the box beams: D1, D2 1.2 mm to 60 mm, D3, D4 0.1 mm to 4 mm.

2.2.4 *ASD – The Space Frame*

A vehicle space frame is the advanced BST that is based on the profile-like (beams) geometry in the structure layout. The shell-like geometry supports the beams in their load-bearing capabilities. The acting loads are mainly distributed among the beams, whereas the shells reinforce the structure in the case of the shear loads.

We prepared the 1D-2D FEm that contains the beam and shell geometry (Fig. 7c). The cross-sectional parameters and dimensions varied for the arbitrary beams: A 0.44 mm^2 to 896 mm^2, Iyy, Izz 0.0895 mm^4 to 470,700 mm^4 and the box beams: D1, D2 1.2 mm to 60 mm, D3, D4 0.1 mm to 4 mm to prioritize the beam-like geometry. The thickness of the shell geometry changed between 0.0 and 1.0 mm.

2.2.5 *ASD – The Hybrid Structure*

A hybrid structure for vehicles is defined as a mix of engineering geometry types, in which the domination of profiles or shells depends on the designer's ideas.

The entire 1D-2D FEm (Fig. 7c) was utilized with the two different intervals of cross-sectional parameters and dimensions. The first setup of the design variables was set for the arbitrary beams: A 0.44 mm^2 to 144 mm^2, Iyy, Izz 0.0895 mm^4 to 7872 mm^4 and box beams: D1, D2 1.2 mm to 20 mm, D3, D4 0.1 mm to 2.0 mm. The second setup was set for the arbitrary beams: A 0.44 mm^2 to 896 mm^2, Iyy, Izz 0.0895 mm^4 to 470,700 mm^4 and box beams: D1, D2 1.2 mm to 60 mm, D3, D4 0.1 mm to 4 mm. The thickness of the shells varied from 0 mm to 0.95 mm for the first setup and 0 to 0.5 mm for the second setup.

2.2.6 *ASD – The Unibody*

A vehicle unibody is the modern BST that utilizes the combination of shells and profiles and the shell geometry dominates in the structural design. The shell geometry also enhances the load-bearing capabilities for shear loads. The profiles are used for very specific load-bearing structural elements, e.g. the B-pillar.

We utilized the entire 1D-2D FEm to achieve the unibody structure design. The cross-sectional parameters and dimensions changed for the arbitrary beams: A 0.44 mm^2 to 144 mm^2, Iyy, Izz 0.0895 mm^4 to 7872 mm^4 and box beams: D1, D2 1.2 mm to 20 mm, D3, D4 0.1 mm to 2 mm to prioritize the beam-like geometry. The thickness of the shell geometry varied between 0 and 0.85 mm.

2.2.7 *ASD – The Monocoque*

A monocoque structure for vehicles is the special case of the unibody BST and is characterized by employing the shell-like geometry for the whole structure design. The number of the profiles is reduced to minimal applications for the specific parts of a new structure (e.g. the A-pillar).

All profiles in the 1D-2D FE (Fig. 7c) model were blocked by modeling them as the box cross-sections with small dimensions (the arbitrary beams: A = 3 mm^2 to 59.04 mm^2, Iyy, Izz 1.25 mm^4 to 693.5232 mm^4 and the box beams: D1, D2 2 mm to 10 mm, D3, D4 0.5 mm to 1.8 mm; the higher values were used for the elements under crash forces) and therefore only permitted optimization for the shells. The thickness of the shell geometry changed be-tween 0 and 6 mm.

3 APPLICATION OF THE ASD - RESULTS AND DISCUSSION

3.1 Beams and Plates as a Fundament to Understand the ASD

The FE calculation results reported in this section correspond with the method testing on a small scale de-scribed in Section 2.1. These results are provided with additional comments. The ASD results for the arbitrary beams reveal the cross-sectional parameters that lead to a proper selection of the suitable beam section, whereas the box beams indicate the possible design proposals based on the industrial types of the beam cross-sections. The figure legends were purposely left inconsistent to reveal more valuable data and the total mass describes the sum of all the components' mass.

3.1.1 *ASD - UDA for Arbitrary and Defined Beams*

The aim of this investigation was to highlight the benefit of the UDA (as a part of the ASD) for the arbitrary and defined box beams. We conducted two

optimization runs for the same FEm (Fig. 4a) for both the arbitrary and defined box cross-sections.

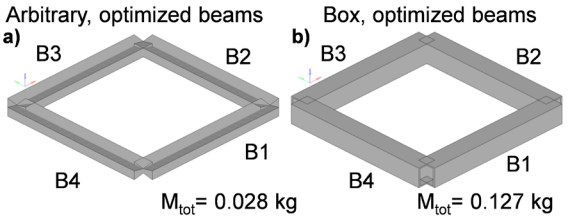

Fig. 8. *ASD results for the beam cross-sections: a) arbitrary, b) box*

The SO results presented in Fig. 8a demonstrate the values of second moments of area for the arbitrary beams. The values of the area are missing in Fig. 8a due to the mathematical description of the arbitrary beam cross-section where the area is only a parameter. The possible shape of the area would introduce the functional relationships (additional constraints) between the area and basic dimensions of the cross-section, which leads to the defined beams. The areas of the arbitrary beams indirectly represent the total resultant mass in Fig. 8a. The optimization run sets the cross-sectional parameters for the arbitrary beams to minimal possible values that minimize the weight and accommodate the acting loads.

The second moments of area for the arbitrary case illustrate this observation more precisely because of the variables of this beam cross-section type that are optimized independently due to the theory of arbitrary beams **[34]** and **[35]**. The values of the $I_o zz$ were set to a high level to increase the bending stiffness of the arbitrary beams (Fig. 8, Table 4). The area of the B2 beam also increases to bear the compression load.

Table 4. *Summary of the UDA for the arbitrary and box beams*

Fig. 8		B1	B2	B3	B4
Arbitrary	A_o [mm²]	7.85	12.82	7.30	7.34
	$I_o yy$ [mm⁴]	211.05	211.06	211.05	211.06
	$I_o zz$ [mm⁴]	1335.80	1335.80	1335.80	1335.80
Box	$D_o 1$ [mm]	12.50	12.50	12.50	12.50
	$D_o 2$ [mm]	12.50	12.50	12.50	12.50
	$D_o 3$ [mm]	1.08	1.06	1.05	1.06
	$D_o 4$ [mm]	0.68	0.67	0.66	0.67
Resultant displacements [mm]: arbitrary x = 11; y = 0.55; z = -5.46; box x = 11; y = 0.18; z = -5.84					
Compliance [kNmm]: arbitrary 130.701; box 128.211					

In the case of the defined box beams, the optimization results in the maximal external dimensions of the box cross-sections that react to the bending and compression loads (Fig. 8, Table 4). The case of the arbitrary beams displays a slightly higher total compliance (the inverse of stiffness) **[34]** and **[35]** than that of the defined box beams (Table 4). This finding means that the defined box beams exemplify a stiffer design. The arbitrary beams show much lower total mass compared to the defined box beams because the arbitrary beams evidence the total resultant mass the uncoupled cross-sectional parameters that satisfy the given boundary conditions theoretically.

Consulting the available catalog of industrial beam products **[36]** and **[37]**, the authors of this work propose the beam with the box cross-section of 13 mm × 13 mm × 1.6 mm to satisfy the design suggestions from the UDA for defined beams. For the arbitrary beams, two solutions can be found: the same as the previous box section and the rectangular box section of 15 mm × 10 mm ×1.5 mm. The last beam type can be applied if there is no geometrical limitation to the design space. These facts affirm that the UDA works for the arbitrary and defined beams and allows for various and broad adaptations of different beam cross-sections.

3.1.2 Conjunction of the Plates (Shells) and UDA for Beams

We tested the conjunction of the plate (shell) geometry and the UDA for beams to highlight the benefits of such a combination. Fig. 9 presents the SO and FSO results for three different optimizations, such as the addition of plate (shell) geometry to the FEm of the beams (the first case, Figs. 9a and b), design space restriction (the second case, Figs. 9c and d) and tougher limits on the displacements (the third case, Figs. 9e and f) and two different types of the beam section: arbitrary and box.

The addition of the extra plate (shell) geometry results in the lower values of the areas and second moments of area for the arbitrary beams (Table 5, Fig. 9a). The resultant values of the first case (Table 5) indicate the load-bearing characteristics such as bending and tension-compression that result from the acting loads. To improve the structural stiffness, the arbitrary beams utilize the thickness of the plate in the corners. For the second case of the design space restriction (Table 5, Fig. 9c), the SO and FSO results for the arbitrary beams are the same as for the first case because this solution satisfies both analyzed cases.

In the case of the restrictive displacement limits, the optimization sets the second moments of area higher than the previous values of the first and second cases. The values of the second moments of area for the arbitrary beams affirm the presence of the bending loads (Table 5). The cross-sectional areas of the arbitrary beams remain on the same level as in the first and second cases

(Table 5). The optimization employs the plate thickness to fulfill the optimization constraints. These employed parts of the plate (Fig. 9e) form the diagonal shape and gain the plate thickness in the corners of the plate.

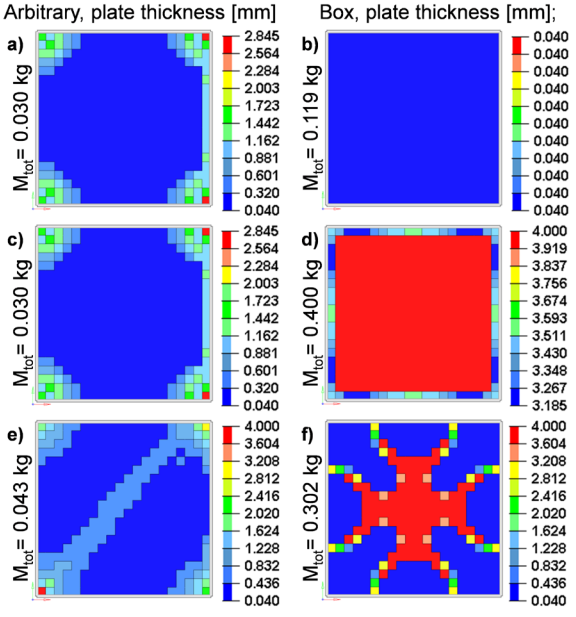

Fig. 9. *ASD results of the frame-plate FEms: a, b) plate addition to the FE beam model, c, d) design space restriction, e, f) restrictive displacement limits*

Owing to the thickness employment, the optimized frame-plate model of the arbitrary beams weighs 0.043 kg, more than the optimized frame-plate model (0.030 kg) for the first and second cases. Considering the total resultant compliance (Table 5) for three cases of the arbitrary beams, the optimized frame-plate model (29.624 kNmm) from the third case displays the stiffest design.

The simultaneous SO and FSO optimizations of the frame-plate model consisting of the box beams demonstrate slightly different results. The optimization of the frame-plate model with the added plate geometry and the box beams reports almost the same values of the cross-sectional dimensions for the first case (Table 5) as those of the pure frame model (Table 4). This remark can also be noticed in Fig. 9b where the optimization neglects the plate thickness. Compared to the first case, the second case of the design space restriction for the box beams reveals the more contrasting results. The optimization places the cross-sectional dimensions to fulfill the optimization boundaries and minimize the weight (Table 5). Due to the insufficient stiffness of the box beams, the optimization makes use of the whole plate to assure the requested stiffness (Fig. 10d). In the third

Table 5. *Conjunction of the plate (shell) and UDA for beams – summary*

Figs. 9a, b / 1st case		B1	B2	B3	B4
Arbitrary	A_o [mm^2]	2.01	7.57	2.01	2.1
	$I_o yy$ [mm^4]	212.89	212.89	212.89	212.89
	$I_o zz$ [mm^4]	7.85	7.85	7.85	7.85
Box	$D_o 1$ [mm]	12.5	12.5	12.5	12.5
	$D_o 2$ [mm]	12.5	12.5	12.5	12.5
	$D_o 3$ [mm]	0.77	0.77	0.77	0.77
	$D_o 4$ [mm]	0.81	0.81	0.81	0.81
Resultant displacements [mm]: arbitrary x = 7.35, y = 0.55, z = -5.95; box x = 4.52, y = 0.19					
Compliance [kNmm]: arbitrary 90.918; box 57.100					
Figs. 9c, d / 2nd case		B1	B2	B3	B4
Arbitrary	A_o [mm^2]	2.01	7.57	2.01	2.1
	$I_o yy$ [mm^4]	212.89	212.89	212.89	212.89
	$I_o zz$ [mm^4]	7.85	7.85	7.85	7.85
Box	$D_o 1$ [mm]	10	10	10	10
	$D_o 2$ [mm]	10	10	10	10
	$D_o 3$ [mm]	0. 82	0. 82	0. 82	0. 82
	$D_o 4$ [mm]	0. 83	0. 83	0. 83	0. 83
Resultant displacements [mm]: arbitrary x = 7.35, y = 0.55, z = -5.95; box x = 0.27, y = 0.10, z = -5.93					
Compliance [kNmm]: arbitrary 90.918; box 9.673					
Figs. 9e, f / 3rd case		B1	B2	B3	B4
Arbitrary	A_o [mm^2]	2.59	7.92	2.57	2.34
	$I_o yy$ [mm^4]	576.50	576.50	576.50	576.50
	$I_o zz$ [mm^4]	10.36	10.36	10.36	10.36
Box	$D_o 1$ [mm]	12.5	12.5	12.5	12.5
	$D_o 2$ [mm]	12.5	12.5	12.5	12.5
	$D_o 3$ [mm]	1.5	1.5	1.5	1.5
	$D_o 4$ [mm]	1.5	1.5	1.5	1.5
Resultant displacements [mm]: arbitrary x = 2.00; y = 0.55; z = -3.50; box x = 0.77, y = 0.10, z = -3.50					
Compliance [kNmm]: arbitrary 29.624; box 12.757					

case of the tougher limits on the displacements, the optimization puts the cross-sectional dimensions to maxi-mal values to satisfy the boundary conditions. To enhance the frame-plate stiffness, the SO and FSO utilize the plate thickness by forming the central cross-like member (Table 5, Fig. 9f).

Observing the total mass of these three box cases, the first case of the frame-plate model possesses the lowest weight, yet the second case represents the stiffest structure (minimal compliance, Table 5). The observations presented affirm that the conjunction of the plate (shell) and the ADA for beams can deliver new helpful pieces of information to the design process. This conjunction points out not only where the plate (shell) can be improved to withstand the

shear loads by adding extra strips of the geometry, but also exhibits the load-bearing characteristics that engineers identify as compression-tension, bending or torsion fields. The delivering of additional design suggestions constitutes the ASD as the functional methodology.

3.1.3 *Conjunction of the Plates (Shells) and the UDA for Beams – System Identification*

The system identification run was performed for the conjunction of the plate (shell) and the UDA for two beam cross-sections: arbitrary and defined box beams. The aim of this system identification was to examine if the FEm (Fig. 4b) can additionally provide the solutions under the highly restricted sets of the model constraints. Fig. 10 and Table 6 display the ASD results of the system identification for the arbitrary a) and box b) beams.

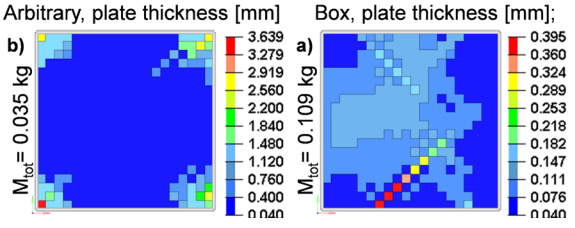

Fig. 10. *ASD results of the system identification for the frame-plate FEms: a) arbitrary beams, b) box beams*

Table 6. *System identification for the frame-plate FEms – summary*

Fig. 10		B1	B2	B3	B4
Arbitrary	A_o [mm^2]	1.99	7.02	1.99	1.99
	$I_o$yy [mm^4]	146.23	146.23	146.23	146.23
	$I_o$zz [mm^4]	10.23	10.23	10.23	10.23
Box	D_o1 [mm]	12.5	12.5	12.5	12.5
	D_o2 [mm]	12.5	12.5	12.5	12.5
	D_o3 [mm]	0.79	0.21	0.79	0.92
	D_o4 [mm]	0.83	0.25	0.83	0.95
Resultant displacements [mm]: arbitrary x = 3.00, y = 0.65, z = -7.50; box x = 2.99, y = 0.55, z = -7.50					
Compliance [kNmm]: arbitrary 45.367; box 44.559					

The simultaneous SO and FSO of the arbitrary beams set the second moments of area to bear the bending loads and the cross-sectional beam areas to handle the compression-tension loads as well as minimize the weight (Table 6). To improve the stiffness of the frame-plate model consisting of arbitrary beams, the optimization increases the plate thickness in the plate's corners (Fig. 10a). In the case of the defined box beams, the SO and FSO assign the cross-sectional dimensions to with-stand the bending (torsion) loads and reduce the overall resultant mass (Table 6). These optimizations adjust the structural stiffness of the frame-plate model by utilizing the plate thickness that forms the central reinforcement (Fig. 10b).

Despite the difference in the weights of the arbitrary and box beams, both optimized frame-plate models depict the same stiffness (similar level of the resultant compliance, Table 6). These remarks suggest that the arbitrary beams offer the indications of possible solutions for a given set of requirements, but the box beams present the real one with the more easily applicable cross-sections.

3.1.4 *Conjunction of the Plate Made of Composite Material and UDA for Beams*

The application of CFRP materials was investigated for the plate (shell) within the frame-plate FEm (Fig. 4b). Fig 11 and Table 7 illustrate this application for the plates of the arbitrary a) and box b) beams.

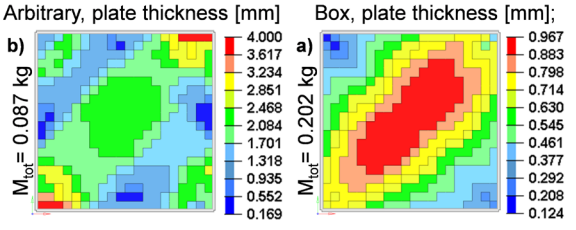

Fig. 11. *ASD results of the CFRP material application for the plate in the frame-plate FEms: a) arbitrary beams, b) box beams*

The simultaneous SO and FSO of the arbitrary beams regulate the values of the second moments of area to bear the bending loads (Table 7). These optimizations also place the cross-sectional areas of the arbitrary beams to limit the overall weight. Since the optimization boundaries were further restrained (Tables 5 and 7) for this application of the CFRP materials (compared to the other cases), the CFRP plate of the arbitrary beams forms the diagonal with the local reinforcements similar (Fig. 11a) to the geometry observed in the steel plate (Fig. 9e) that strengthens the beam-plate structure. For the frame-CFPR plate model of the box beams, the SO and FSO set the cross-sectional dimensions to accommodate the bending loads and moderate the structural weight (Table 7).

To improve the structural stiffness of the frame-CFRP plate, the SO and FSO employ the CFRP plate thickness that creates the diagonal with the center part of the high thickness (Fig. 11b). After optimization,

the defined box frame-CFRP plate model weighs nearly 0.202 kg, which is 0.1 kg less than the frame-plate made of steel. In the case of the arbitrary frame-CFRP plate model, the optimized structure weighs 0.087 kg, which is approximately three times more than the frame-plate made of steel.

Table 7. *CFRP material application for the plate in the frame-plate FEm – summary*

Fig. 11		B1	B2	B3	B4
Arbitrary	A_o [mm²]	14.62	27.19	15.53	16.81
	I_oyy [mm⁴]	305.83	305.83	305.83	305.83
	I_ozz [mm⁴]	7.85	7.85	7.85	7.85
Box	D_o1 [mm]	12.5	12.5	12.5	12.5
	D_o2 [mm]	12.5	12.5	12.5	12.5
	D_o3 [mm]	1.34	1.37	1.33	1.33
	D_o4 [mm]	1.38	1.41	1.37	1.37
Resultant displacements [mm]: arbitrary x = 1.00, y = 0.23, z = -4.00; box x = 1.00; y = 0.11, z = -4.0					
Compliance [kNmm]: arbitrary 16.690; box 15.803					

Considering the total resultant compliance, both the arbitrary and box frame-CFRP plates disclose almost the same structural stiffness (Table 7) and exceed the structural stiffness of the corresponding frame-plate made of steel (Tables 5 and 6). This investigation proves that other material types such as composite materials, CFRPs and sandwich composites (also metal sandwich composites) can be analyzed and optimized by the ASD as well as provide profitable suggestions for a new structure design.

3.2 ASD – A New Structure for the eQuad

The FE calculation results reported in this section match with the method testing on a large scale described in Section 2.2. The ASD results are provided with additional comments. For the reason of available space, we only report the graphical illustrations for the selected and defined (Section 3.2) BSTs. The lists of the resulting values from the optimization runs, which contain 80 optimization constraints and 128 (arbitrary beams) as well as 169 (defined box beams) design variables for each BST, could extend the length of this work excessively.

The ASD results for the arbitrary beams display the cross-sectional parameters and indicate the beams with the load-bearing characteristics that help to select proper suitable beam sections, whereas the box beams reveal the possible design proposals based on the available industrial types of the beam cross-sections. The figure legends were purposely left inconsistent to reveal more valuable data. The total mass presented in the figures describes the sum of all the components' mass.

3.2.1 ASD – The Tubular Space Frame

We obtained the tubular space frame design for a new eQuad structure by performing SO. Fig. 12 presents the geometrical representation of the SO results for arbitrary a) and box b) beam cross-sections.

The SO results of the arbitrary beams (Fig. 12a) graphically display the values of the second moment of area without the values of the cross-sectional areas due to the theory of the arbitrary beams (Section 4.1) **[34]** and **[35]**. The cross-sectional beam areas are indicated indirectly by the total resultant mass (7.44 kg) of a new structure. These SO results of the arbitrary beams deliver the optimal values of the cross-sectional parameters that allow engineers to select the most suitable beam cross-section for the load-bearing. Following the principal ideas of the UDA for beams (information about load-bearing), Fig. 12a indicates the beams where the bending and/or torsion loads dominate. The beams with the dominating tension-compression loads can be identified by analyzing the resultant values of the cross-sectional areas for all arbitrary beams.

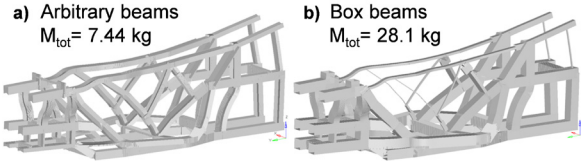

Fig. 12. *ASD results for the tubular space frame design: a) arbitrary beam, b) box beams*

Fig. 12b illustrates the SO results of the optimized cross-sectional dimensions for the box beams. The SO adapted the cross-sectional dimensions to accommodate the acting load. Similar to the arbitrary beams, the values of the box cross-sectional dimensions (Fig. 12b) also suggest the load-bearing characteristics (tension-compression, bending and torsion) by tailoring the proper dimensions of the box cross-sections. In Fig. 12b, there are the beams with the small cross-sections (central upper part of a new structure) as well as with the large cross-sections (central and lower, front and rear parts of the new structure). The new structure consisting of the box beams weighs 28.1 kg because the cross-sectional dimensions of the box beams are related in the functional relationship.

In spite of the difference in weight, the arbitrary and box beams deliver the valuable proposals of a new structure that offer the stiff and lightweight design com-pared to the current structure design (Fig. 5c). The slightly lower compliance for the arbitrary beams (1171.3 kNmm) discloses this solution being stiffer than the box beams (1271 kNmm). These observations suggest that the ASD provides profitable proposals for the tubular space frame design.

3.2.2 ASD – The Space Frame

The space frame design of the new eQuad structure was obtained by utilizing the SO and FSO simultaneously. Fig 13 reports the SO and FSO results of a new structure design for the a) arbitrary and b) defined box beams.

The application of the shells in the 1D-2D FEm of the arbitrary beams influences the values of the cross-sectional areas and second moments of area (Figs. 13a, b). The cross-sectional areas decrease and the second moments of area adapt locally by sizing the correspond-ing values of cross-sectional parameters forcing the shells to bear more loads, especially shear loads. These sized values of the second moments of area indicate the load-bearing characteristics of bending loads. As a result of the great shear load-bearing characteristics, the arbitrary beams with the shells weigh 34.1 kg, which is considerably more than the 7.44 kg of the tubular space frame.

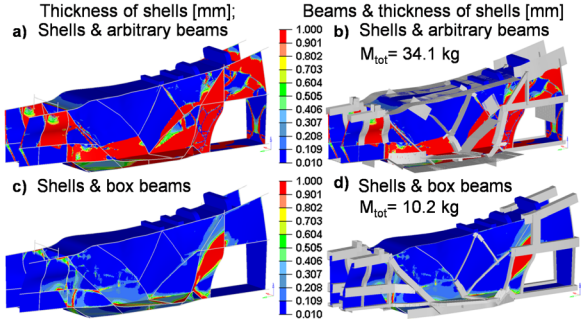

Fig. 13. *ASD results for the space frame design: a, b) arbitrary beams, c, d) box beams*

The shells impact the defined box beams more evidently (Fig. 13b), reducing the total resultant mass to 10.2 kg, which is two times lower than the weight of the tubular space frame (28.1 kg) consisting of box beams. This lower weight results from the combined SO and FSO that set the cross-sectional dimensions of the box beams to minimize the weight and maximize the second moments of area. The reduced cross-sectional areas need a sup-port of the shells to bear the acting loads.

Regardless of the difference between the two resultant weights, the ASD provides the space frame designs with a similar level of compliance: 1762 kNmm for the arbitrary and 1855 kNmm for the box beams. These observations confirm that the ASD can deliver suitable proposals for a new space frame design.

3.2.3 ASD – The Hybrid Structure

We achieved the hybrid structure design of a new eQuad structure by performing the SO and FSO simultaneously for the two setups of the 1D-2D FEm that consists of the arbitrary and defined box beams. Fig. 14 presents the obtained proposals for the hybrid structure designs for the first setup of the arbitrary (Figs. 14a and b) and box (Figs. 14c and d) beams.

Compared to the results of the tubular space frame and the space frame for the arbitrary beams, the shells from the hybrid structure affect the arbitrary beams more evidently. Because of the tighter design space (lower allowable values of the cross-sectional parameters), the SO and FSO minimize the weight of a new structure by setting the suitable values of the second moment of area and reducing the cross-sectional areas of the arbitrary beams.

The simultaneous SO and FSO utilize the shells to improve the load-bearing characteristics of the arbitrary beams. This improvement results in the employment of the large shell surfaces that display the great variety of the shell thickness (Figs. 14a and b). More importantly, the hybrid structure of the shells and arbitrary beams weighs 18.5 kg, which places the hybrid structure in the middle between the proposal designs of the tubular space frame and space frame.

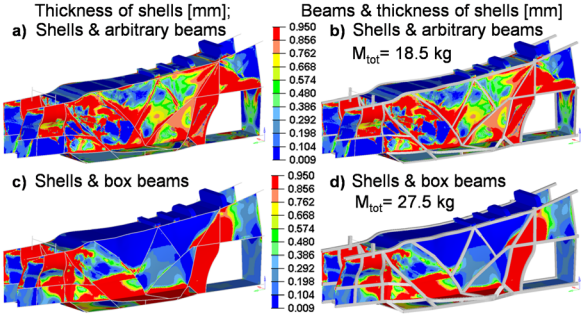

Fig. 14. *ASD results for the hybrid structure design: a, b) arbitrary beams, c, d) box beams*

Similar to the arbitrary beam case, the shells impact the results of the hybrid structure for the box

beams (Figs. 14c and d). The simultaneous SO and FSO adjust the cross-sectional dimensions of the box beams to minimize the weight and bear the acting loads. Because of the tighter design space, the cross-sectional dimensions exhibit maximal values for the external dimensions and moderate values for the internal ones (Fig. 14d).

The optimization uses parts of the shell surfaces to satisfy the given boundary conditions. Owing to the functional relationship of the cross-sectional dimensions, the hybrid structure consisting of the shells and box beams weighs 27.5 kg, which is slightly less than the tubular space frame and considerably more than the space frame.

The less common observations can also be made for the second setup (Fig. 15) of the 1D-2D FEm. The wider design space allows the cross-sectional parameters of the arbitrary beams (Figs. 15a, b) to set the higher values of the areas and second moments of area. The values of the second moments of area, which are presented in Fig. 15b, show the obtained values that indicate the actual characteristics of the acting loads such as bending and (or) torsion.

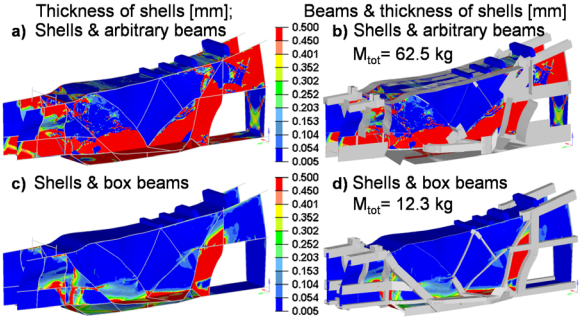

Fig. 15. *ASD results for the hybrid structure design: a, b) arbitrary beams, c, d) box beams*

Compared with the first setup of the hybrid structure and other BSTs, the thick shells dominate more evidently in the new structure, especially in the lower center part. Thus, this hybrid structure weighs 62.5 kg, which reaches the mass of the present eQuad tubular space frame.

In the case of the box beams, the simultaneous SO and FSO assign the external cross-sectional dimensions to the high values and the internal dimensions to the lower ones to minimize the weight (Figs. 15c and d). To enhance the structural stiffness, the optimization exploits the shell surfaces locally. This hybrid structure comprising the box beams weighs only 12.3 kg and bears a re-semblance to the space frame design (Figs. 13c and d).

Considering the level of the total resultant compliances (invert stiffness), the second setup for the arbitrary beams provides more stiffness (2680 kNmm) than the first one (3547 kNmm), whereas the hybrid structure with the box beams from the first setup delivers the toughest design (1531 kNmm vs. 1761 kNmm of the second setup) among all cases of the hybrid structure. The results presented indicate that the ASD produces valuable proposals for the hybrid structure design.

3.2.4 ASD – The Unibody

We obtained the unibody design of the new eQuad structure by simultaneously executing the SO and FSO for the given design space. Fig. 16 reveals the design proposals for the unibody for the arbitrary (a,b) and box (c,d) beams.

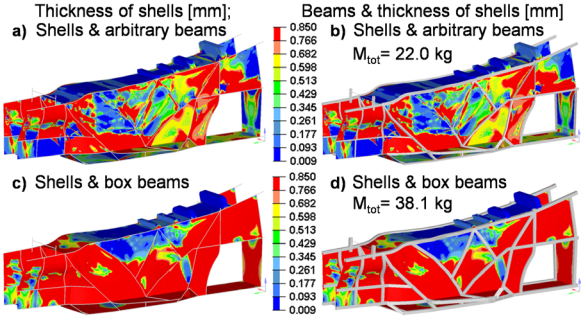

Fig. 16. *ASD results for the unibody design: a,b) arbitrary beams, c, d) box beams*

In the case of the arbitrary beams (Figs. 16a and b), the optimization adjusts the values of the second moments of area between the lower and medium levels. These optimized values disclose the load-bearing characteristics (bending and/or torsion loads) of the arbitrary beams. The SO and FSO position the values of the cross-sectional areas to reduce the total resultant mass. To fulfill the displacement constraints, the optimization utilizes the various thicknesses of the shell surfaces (Figs. 16a and b).

As a consequence of this (SO and FSO) optimization, the unibody design of the arbitrary beams weighs 22 kg. Compared to the presented results of the arbitrary beams for the tubular space frame, space frame and hybrid structure, the unibody consisting of the shells and arbitrary beams displays the medium weight.

The application of the shell geometry in the box beams (Figs. 16c and d) reveals results that show a resemblance to the arbitrary beam case. The

simultaneous SO and FSO optimization assigns high values for the external cross-sectional dimensions and moderate to high values for the internal dimensions to increase the bending and/or torsional stiffness and decrease the overall structure weight. To raise the structural stiffness, the optimization employs shell surfaces with the full thickness (Figs. 16c and d). Consequently, this combined frame-shell weighs 38.1 kg. Considering the total resultant mass of the tubular space frame, space frame and hybrid structure, this unibody design containing the shells and box beams demonstrates a heavier design than the other proposals.

Despite its heavier weight, the unibody design of box beams contrasts the very stiff design; the compliance (1342 kNmm) is relatively low compared to the tubular space frame case. The unibody design of the arbitrary beams demonstrates, however, similar stiffness (3880 kNmm) to the first setup for the hybrid structure. Regarding the observations revealed, the ASD generates profitable design suggestions for the unibody structure.

3.2.5 *ASD – The Monocoque*

The monocoque design was obtained by carrying out FSO for the 1D-2D FEm (Fig. 7c). Fig. 17 presents the design proposals for the monocoque BST for the arbitrary (a, b) and (c, d) box beams.

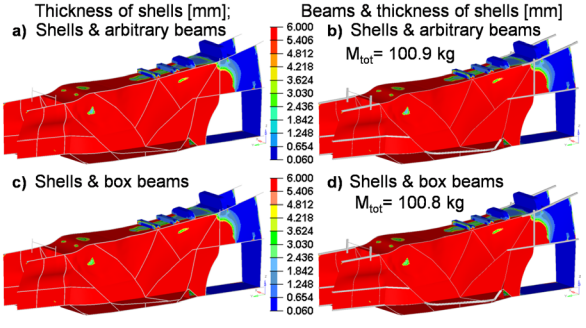

Fig. 17. *ASD results for the monocoque design: a, b) arbitrary beams, c, d) box beams*

Because FSO neglects the optimization of the arbitrary and box beams, the optimization results point out the same thickness distributions throughout both structures for the arbitrary (Figs. 17a and b) and box (Figs. 17c and d) beams. FSO optimization utilizes the majority of the shell geometry by setting the shell thickness at the high value of 6 mm. Only in the rear part of the new structure does the shell geometry remain almost without the material (Fig. 17). Owing to the great employment of the shell areas and shell thickness, the new monocoque structure possesses the heaviest weight (100.9 kg) of all of the BSTs achieved.

Considering the total resultant compliance (invert stiffness), the monocoque made of steel displays a notably lower stiffness (compliance: 5540 kNmm for the arbitrary and 5938 kNmm for the box beams) than the other BSTs presented, such as the uni-body. This remark can be explained by the poor load-bearing capability for the load case of bending on the rear axle (1917 kNmm for the arbitrary and 2401 kNmm for the box beams). To overcome this local insufficient stiffness, the automotive industry designs the attached structure of suspension parts as a separate tubular space frame or a separate space frame **[9]** to **[12]**. If the term of compliance for bending on the rear axle decreases, the steel monocoque possesses the compliance that is comparable with the other BSTs.

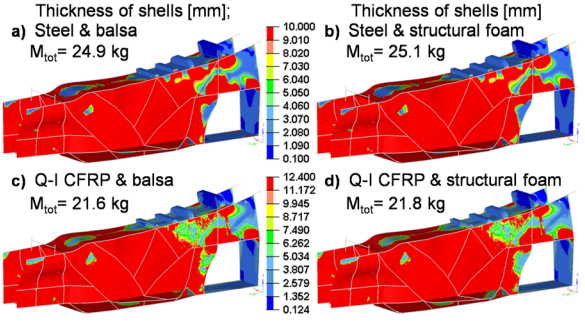

Fig. 18. *ASD results for the monocoque design: a) steel & balsa wood, b) steel & structural foam, c) Q-I CFRP & balsa wood, d) Q-I CFRP & structural foam*

Because of the highest weight of the steel monocoque, we also tested four additional pairs of the lightweight material (material properties from Table 2, **[47]** to **[51]**) namely steel with structural foam (AIREX® C70), steel with balsa wood (BALTEK® SB.50), Q-I CFRP with structural foam, and Q-I CFRP with balsa wood. These pairs of the composite sandwich materials were expected to decrease the overall weight of the monocoque structure significantly.

Fig. 18 reports the monocoque designs obtained from the FSO for the four pairs of the lightweight materials and the box beams. These monocoque designs (Fig. 18) display very similar material distributions to the design of the steel monocoque (Fig. 17). The thickness of the shell geometry increases markedly, however, to satisfy the optimization constraints. The thickness of the shells doubles for the Q-I CRFP with the balsa wood and PVC foam.

Owing to the sandwich structure design that offers a notable mass reduction, the monocoque designs of the four material pairs weigh approximately 21.6 kg to 25.1 kg. These weights are comparable with the other BSTs and are considerably less than the unibody design of the shells and box beams. The monocoque designs of the four material pairs exhibit lower stiffness than that of the steel monocoque. If the load-bearing capacity for the loads of the side crash (as a medium value of 2810 kNmm) and bending on the rear axle (as a medium value of 2816 kNmm) increases, the monocoque designs of the four material pairs deliver lightweight and stiff structures.

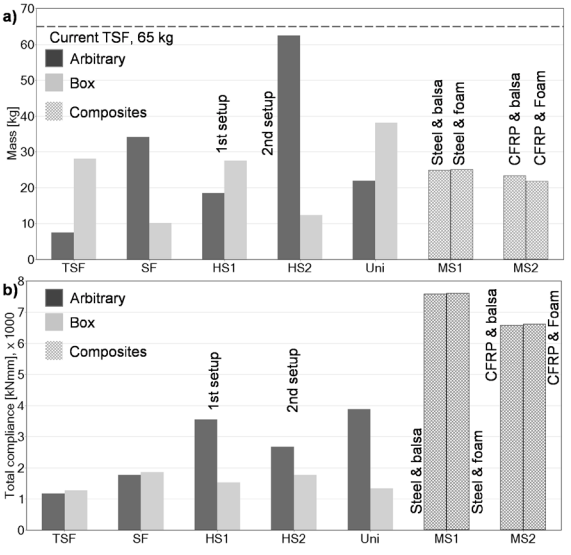

Fig. 19. *Comparison of the resulting BSTs from the ASD application: a) mass level, b) compliance level; TSF tubular space frame, SF space frame, HS hybrid structure, Uni unibody, MS monocoque structure*

These results confirm the original material distribution obtained for the steel monocoque design (Fig. 17) and assert that the ASD also provides worthwhile design suggestions for the monocoque design made of composites (Fig. 18).

As a summary of the ASD's design advantages, Fig. 19 affirms the delivery of the various lightweight design concepts for a new eQuad structure. All of these delivered BSTs present the structural mass (Fig. 19a) that is markedly beneath the current tubular space frame design. The distribution of the total compliance (Fig. 19b) indicates to the stiffest design concepts (Uni, HS1 and TSF) from the obtained BSTs.

4 CONCLUSIONS

In recent years, engineers have begun to apply TO to provide the first design suggestions for new structures. Consequently, TO delivers the bionic shapes that demand additional treatment to obtain manufacturable geometry. Our ASD allows for the smooth transition of the TO results into design concepts of a new structure. The ASD enables engineers to realize the studies of various BSTs within only one FEm by adjusting the model parameters, changing (replacing) available materials and setting the prioritizing of the fundamental structural elements (beams and plates). Our results affirm that the ASD delivers profitable lightweight proposals for the selected BST concepts such as tubular space frame, space frame, hybrid structure, unibody and monocoque.

The ASD results prove that the steering criteria permit engineers to pick and optimize the selected BSTs. Our ASD reveals the characteristics of acting loads such as tension-compression, bending and torsion in the fundamental structural elements (beams and plates) by reporting the cross-sectional parameters (areas and second moments of area) and dimensions of analyzed beams and by pointing out the geometrical shapes as well as thicknesses of additional plates (shells). The ASD results also illustrate the influence of the plate (shell) geometry on the structural stiffness versus the change in the overall weight that can greatly increase the load-bearing of a new structure. Additionally, the ASD results help to identify the acting loads or load cases that provoke the high values of the compliance, which indicates the necessary improvements to increase the structural rigidity (Fig. 19).

Once the design proposals for the possible BSTs are delivered for the new eQuad structure, the most suitable proposal needs to be chosen for the tailoring of a resultant body-in-white step and the further design sophistication phase to take full advantage of real material properties such as strength. Considering our ASD results, the space frame and the second case of the hybrid structure (Fig. 19) assert their advantages over the other BSTs analyzed. The design sophistication phase requires for the final structure refinement that those two chosen BSTs should merge into one coherent design to perform the enhancement of a new tailored structure for real material data. The first results of the design sophistication phase suggest maintaining the level of lightweight design.

5 ACKNOWLEDGEMENTS

This work was accomplished at the VIRTUAL VEHICLE Research Center in Graz, Austria. The authors would like to acknowledge the financial support of K-Project WoodC.A.R. – Computer Aided Research, the COMET K2 - Competence Centers for Excellent Technologies Programme of the Austrian Federal Ministry for Transport, Innovation and Technology (bmvit), the Austrian Federal Ministry of Science, Research and Economy (bmwfw), the Austrian Research Promotion Agency (FFG), the Province of Styria and the Styrian Business Promotion Agency (SFG).

6 REFERENCES

[1] Cavazzuti, M., Baldini, A., Bertocchi, E., Costi, D., Torricelli, E., Moruzzi, P. (2011). High performance automotive chassis design: a topology optimization based approach. *Structural and Multidisciplinary Optimization*, vol. 44, no. 1, p. 45-56, **DOI:10.1007/s00158-010-0578-7**.

[2] Christensen, J., Bastien, C., Blundel, M.V., Grimes, O., Appella, A., Bareham, G., O'Sullivan, K. (2012). Generation of optimised hybrid electric vehicle body in white architecture from a styling envelope. *Global Journal of Researches in Engineering Automotive Engineering*, vol. 12, no. 1.

[3] Agkathidis, A., (2016). Implementing biomorphic design, design methods in undergraduate architectural education. *Proceedings of eCAADe 34th Annual Conference*, vol. 1, p. 291-298.

[4] Rokicki, W., Gawell, E. (2016). Voronoi diagrams – rod structure research models in architectural and structural optimization. *MAZOVIA Regional Studies, Analyses and Studies*, no. 19, p. 155-164, **DOI:10.21858/msr.19.10**.

[5] Galjaard, S., Hofman, S., Perry, N., Ren, S. (2015). Optimizing structural building elements in metal by using additive manufacturing, *Proceedings of International Association for Shell and Spatial Structures Symposium*, Amsterdam.

[6] Fastermann, P. (2014). *3D-Drucken – Wie die generative Fertigungstechnik funktioniert*, Springer Vieweg, Berlin, Heidelberg.

[7] Hagl, R. (2015). Das 3D-Druck-Kompendium, Leitfaden für Unternehmer, *Berater und Innovationstreiber, 2nd Ed.,* Springer Gabler, Wiesbaden, **DOI:10.1007/978-3-658-07047-2**.

[8] Moser, A., Schweiger, R. (2007). Prospects and barriers for Up-Front CAE-Simulation in the automotive development. *Proceedings of NAFEMS World Congress Vancouver*.

[9] Crolla, D.A. (2009). *Automotive Engineering, Powertrain, Chassis System and Vehicle Body*, Elsevier Inc.

[10] Mallick P.K. (2010). *Materials, Design and Manufacturing for Lightweight Vehicles*, Woodhead Publishing Ltd., Cambridge, **DOI:10.1533/9781845697822**.

[11] Davies, G. (2012). *Materials for Automobile Bodies*, Butterworth-Heinemann, Elsevier Ltd., Oxford.

[12] Friedrich, H.E. (2013). *Leichtbau in der Fahrzeugtechnik*, Springer Vieweg, Wiesbaden, **DOI:10.1007/978-3-8348-2110-2**.

[13] Calì, M., Oliveri, S.M., Ambu, R., Fichera, G. (2018). An integrated approach to characterize the dynamic behaviour of a mechanical chain tensioner by functional tolerancing. *Strojniški vestnik - Journal of Mechanical Engineering*, vol. 64, no. 4, p. 245-257, **DOI:10.5545/sv-jme.2017.5079**.

[14] Future Steel Vehicle, Phase 2 - Report (2011). *World Auto Steel*, Brussels.

[15] Hirz, M., Gfrerrer, A., Dietrich, W. (2013). *Integrated Computer-Aided Design in Automotive Development*, Springer-Verlag, Berlin Heidelberg.

[16] Česnik, M., Slavič, J., Boltežar, M. (2016). Assessment of the fatigue parameters from random vibration testing: Application to a rivet joint. *Strojniški vestnik - Journal of Mechanical Engineering*, vol. 62, no. 7-8, p. 471-482, **DOI:10.5545/sv-jme.2016.3774**.

[17] Mršnik, M., Slavič, J., Boltežar, M. (2018). Vibration fatigue using modal decomposition. *Mechanical Systems and Signal Processing*, vol. 98, p. 548-556, **DOI:10.1016/j.ymssp.2017.03.052**.

[18] Höfer, C. (2013). A Winner: Car Body Design Development of the Hyundai Sonata, *Proceedings of 12th annual Great Designs in Steel seminar*, Steel Market Development Institute.

[19] Current & Future Technologies in Automotive Engineering Simulation (CAE) (2008). *AUTOSIM Consortium*, NAFEMS.

[20] Son, I., Noh, Y., Choi, E., Choi, J., Ji, Y., Lim, K. (2018). Optimization of the flow path efficiency in a vacuum cleaner fan. *Strojniški vestnik - Journal of Mechanical Engineering*, vol. 64, no, 4, p. 258-268, **DOI:10.5545/sv-jme.2017.4736**.

[21] Harzheim L. (2014). *Strukturoptimierung: Grundlagen und Anwendungen*, 2. Auflage, Europa-Lehrmittelm.

[22] Kang, B. (2015). CAE for Digital Development. *Proceedings of European Altair Technology Conference*, Paris.

[23] Groth, M. (2015). *Introduction to the theory of derivators*, Mathematical Institute of the University of Bonn, Bonn.

[24] Stanton, M. (2015). Exceeding customer expectations by left shifting with robust virtual engineering at jaguar land rover. *Proceedings of European Altair Technology Conference*, Paris.

[25] Nair, N. (2014). CAE driven multi-disciplinary optimization of vehicle systems. *Proceedings of 13th LS-DYNA Forum*.

[26] The Association of German Engineers (VDI) (1997). *VDI 2221: Methodik zum Entwickeln und Konstruieren technischer Systeme und Produkte*, Verein Deutscher Ingenieure, Düsseldorf.

[27] The Association of German Engineers (1997). *VDI 2222: Blatt 1 Methodisches Entwickeln von Lösungsprinzipien*, Verein Deutscher Ingenieure, Düsseldorf.

[28] Sellgren, U. (1999). *Simulation-Driven Design - Motives, Means, and Opportunities*, PhD Thesis, KTH, Stockholm.

[29] Osborne, G., Prater, G., Lesiv, R., Lamb, D., Castanier, M. (2011). Vehicle concept model abstractions for integrated geometric, inertial, rigid body, powertrain, and FE analyses. *Proceedings of ASME International Mechanical Engineering Congress and Exposition*, Denver, **DOI:10.1115/IMECE2011-63590**.

[30] Steinwall, J., Viippola, P. (2014). *Concept Development of a Light-weight Driver's Seat Structure & Adjustment System*, MSc thesis, Chalmers University of Technology, Gothenburg.

[31] Baskin, D.M., Reed, D.B., Seel, T.N., Hunt, M.N., Oenkal, M., Takacs, Z., Vollmer, A.B. (2008). A Case Study in Structural Optimization of an Automotive Body-In-White Design. *Proceeding of SAE International 2008 World Congress*, Detroit, **DOI:10.4271/2008-01-0880**.

[32] Jedrzejczyk, R.P., Alb, M.S., Jost, T. (2018). Integrative CAE-driven design process in the embodiment design phase of L7e vehicle structures. *Strojniški vestnik - Journal of Mechanical Engineering*, vol. 64, no. 1, p. 3-16, **DOI:10.5545/sv-jme.2017.4489**.

[33] Haberhauer, H., Bodenstein, F. (2014). *Maschinenelemente, Gestaltung, Berechnung, Anwendung, 17th ed*., Springer Vieweg, Berlin Heidelberg, **DOI:10.1007/978-3-642-37417-3**.

[34] Altair Engineering Inc. (2015). *HyperWorks 14.0, OptiStruct Reference Guide*, Troy, Michigan.

[35] Altair Engineering Inc. (2015). *HyperWorks 14.0, OptiStruct User's Guide*, Troy, Michigan.

[36] Parker Steel Company (2016). Metric Size Metals*, Metric Metals Reference Guide*. Toledo.

[37] SSAB (2016). *Structural Hollow Section – Dimensions and Cross-Sectional Properties*, SSAB AB, Stockholm.

[38] Soden, P.D., Hinton, M.J., Kaddour, A.S., (1998). Lamina properties, lay-up configurations for a range of fibre-reinforced compo-site laminates. *Composites Science and Technology*, vol. 58, p. 1011-1022, **DOI:10.1016/S0266-3538(98)00078-5**.

[39] Daniel, M.I., Ishai, O. (2006). *Engineering Mechanics of Composite Materials. 2nd ed*. Oxford University Press, New York, Oxford.

[40] VIRTUAL VEHICLE Research Center (2017). eQuad, from *http://www.v2c2.at/foerderprogramme/k2-forschungsprogramm/ee-software/projects/equad/*, accessed on 2017-10-23.

[41] Edwards, M., Seidl, M., Carroll, J., Nathanson, A. (2014). *Provision of Information and Services to Perform an Initial Assessment of Additional Functional Safety and Vehicle Construction Requirements for L7e-A Heavy On-Road Quads*. Transport Research Laboratory, European Commission, Brussels.

[42] Horvath, C.D., Cannon, M. (2012). Future Material opportunities and direction for lightweighting automotive body structures. *Proceeding of Advanced High-Strength Steels for Automotive Lightweighting USCAR Offices*, Southfield, .

[43] Roland Berger GmbH (2017). *Automotive Metal Components for Car Bodies and Chassis, Global market study*, Munich.

[44] Keeler, S., Kimchi, M., Mooney, P.J. (2017). Advanced High-Strength Steels Application Guidelines Version 6.0, World Auto Steel, Brussels. Jedrzejczyk, R.P., Jost, T. (2015). The finite element assessment of structure properties for an L7e class vehicle under the bending, torsion static and crash loads. *Proceedings of ICoEV International Conference on Engineering Vibration*, Ljubljana.

[45] Malen, D.E. (2011). Fundamentals of Automobile Body Structure Design. *SAE International*, Warrendale, **DOI:10.4271/R-394**.

[46] Jedrzejczyk, R.P., Jost, T. (2015). The finite element assessment of structure properties for an L7e class vehicle under the bending, torsion static and crash loads. *Proceedings of ICoEV International Conference on Engineering Vibration*, Ljubljana.

[47] Songhan Plastic Technology Co., Ltd. (2016). *3A Composites Core Materials BALTEK® SB.50 Structural End-Grain Balsa, Data Sheet*, Fengxian District, Shanghai City.

[48] MatWeb Material Property Data (2018), 3A Composites Core Materials BALTEK® SB.50 Structural End-Grain Balsa, from *http://www.matweb.com/search/datasheet.aspx?matguid=680f7698bfed40d9854a2b2b9ced7c3e&ckck=1*, accessed on 2018-09-18.

[49] Airex AG (2011). *3A Composites Core Materials AIREX® C70 Universal Structural Foam*, Data Sheet, Sins,

[50] MatWeb Material Property Data (2018). 3A Composites Core Materials AIREX® C70.55 Universal Structural Foam, from *http://www.matweb.com/search/DataSheet.aspx?MatGUID=d6bdd351de1240eba63335fb439978e4*, accessed on 2018-09-18.

[51] Stoll, F., Campbell, S., Banerjee, R., Griffin, D. (2008). Blade design with engineered cores materials, *Wind Turbine Blade Workshop*, Albuquerque.

Strojniški vestnik - Journal of Mechanical Engineering 65(2019)3, 181-188

DOI:10.5545/sv-jme.2018.5730 Original Scientific Paper
Received for review: 2018-09-03
Received revised form: 2019-02-15
Accepted for publication: 2019-02-21

Physical-Mechanical Characterization of Moriche Natural Fibre (*Mauritia flexuosa*) and Composite with Bio-epoxy Resin

William Javier Mora Espinosa* – Bladimir Azdrubal Ramón Valencia – Gonzalo G. Moreno Contreras
University of Pamplona, Colombia

The characterization of natural fibres is currently used in the field of science and engineering of materials with the purpose of developing new bio-composites friendly to the environment. The goal of this research is to manufacture and characterize a bio-composite reinforced with Moriche palm fibre (Mauritia flexuosa) and to determine the thermal, mechanical and morphological properties of the fibre. Subsequently, the tensile and flexion properties of the composite was evaluated, as well as its morphology. The thermogravimetric analysis demonstrated that the fibre has hydrophilic characteristics and good stability at temperatures close to 200 °C. In the tensile test under static axial forces, its modulus of elasticity, stress and maximum deformation was determined. Its morphology, composed of the small lumen and wide cell wall with size variations, was examined with scanning electron microscopy (SEM). In the same way, the maximum tensile stress of the composite leads to the conclusion that it is viable to use this material for applications in non-structural elements, which are below 25 MPa. The results of maximum flexural strength (253.7 MPa) allow more extensive applications in doubly supported or overhanging parts subjected to concentrated or distributed loads. The microstructure obtained with SEM showed a poor adhesion between the matrix and the reinforcement.
Keywords: natural fibres, bio-composite, reinforcement, characterization

Highlights
- *The natural fibre was characterized thermally, mechanically, and morphologically.*
- *A uniform 45° artisan fabric was used as reinforcement in the bio-composite.*
- *The tensile and flexural properties in the bio-composite were determined, and the adhesion was evaluated by means of a SEM test.*
- *The flexural properties obtained allow the bio-composite to be used in simply supported components that support different types of loads.*

0 INTRODUCTION

Recently, increasing attention has been given towards the development of green (or eco-friendly) products in the field of composites, motivating a wide range of research on the use of matrices and reinforcements of types of organic materials in its production [1]. The utilization of natural fibres as substitutes for traditional synthetic fibres (glass and carbon), used as reinforcement in biologically based and synthetically based matrices, for properties such as: mechanical strength, high specific modulus, density, low weight, thermal stability, low cost, lower energy requirement, less wear on processing, wide availability, excellent biodegradability, and resistance to deforestation [2].

The most commonly used natural-type reinforcements are lignocellulosic fibres, constituted of crystalline microstructures formed by cellulose and other spirals connected by amorphous lignin and hemicellulose [3]. The mechanical strength of the fibre is directly related to the angle of these cellulose fibrils; a lower angle ensures a better mechanical response of the fibre [4]. Its mechanical, thermal, and structural properties allow multiple uses in industry, mainly for manufacturing parts, in sectors such as automotive and packaging [5], displacing conventional materials in some applications, especially compounds made with synthetic fibres of glass, carbon and other manmade fibres [6], particularly in applications where low maintenance and weather resistance are required [7]. Composites are widely used in various industrial applications because of their properties and ease of tailoring to meet specific requirements [8]. The automotive sector has focused on applications mainly for interiors and semi-structural uses, for which stem fibres have dominated, both in thermoplastic and thermostable matrices [9].

Colombia has more than 26,000 species of plants [10]; many of them produce fibres, which are only used at the artisanal level [11], to supply basic needs or to manufacture implements such as bags, hats, rugs, baskets, and sacks [12] and [13]. This research focuses on the Moriche palm fibre (MPF) that comes from the young leaves of the plant located between 30 m and 40 m, according to the height of the palm [14]. By processes such as extraction, defibration, cooking, and drying, the leaves are transformed into fibres for use by craftsmen in the manufacturing of various fabrics [12], mainly in the Tucano and Nukak Maku ethnic groups' residents in the Colombian Amazon [15].

*Corr. Author's Address: University of Pamplona, Km 1 Highway to Bucaramanga, Pamplona, Colombia, william.mora2@unipamplona.edu.co

The potential as a reinforcement in bio-composite materials was evaluated by finding its thermal stability using thermogravimetric (TG) curves. The mechanical behaviour was obtained with a uniaxial tension test adjusted to the ASTM D3822/D3822M-14 standard [16], determining the resistance of the cellulose micro-fibrils coupled within an amorphous matrix of lignin and hemi-cellulose that constitute the fibre [17]. Finally, the microstructure was observed through a scanning electron microscope (SEM), allowing determination of the influence of its geometry on the tensile strength, where the lumen and the cell wall thickness are the determining factors of the mechanical properties of the fibre [18]. When making a comparison with other natural fibres investigated by various authors, the viability of this fibre was validated in the development of new low-cost materials and friendly to the environment.

Once the fibre has been characterized and validated, it is used as a reinforcement to make a bio-composite through the vacuum assisted resin transfer moulding process (VARTM) [19], with an epoxy resin matrix obtained from agro-industrial waste [20]. The material obtained is mechanically characterized by tensile and bending tests using ASTM D3039/D3039M-14 [21] and ASTM D790–15 [22] standards, respectively. The microstructure observed via the SEM test enabled an evaluation of the adhesion between the fibre and the resin. When the mechanical properties were obtained, and the adhesion verified, the bio-composite was compared with other materials reinforced with natural fibres to identify possible application fields.

1 METHODS AND MATERIALS

The methods used to determine the properties of fibre and bio-composite are based on standardized procedures for ASTM, thermogravimetric analysis (TGA), and SEM tests.

The manufacture of the compound using vacuum-assisted resin transfer moulding (VARTM) method was adapted from an industrial process.

1.1 Reinforcement of Moriche Palm Fibre

The MPF can reach a height of 40 meters in the Amazon region, taking a diameter of 30 cm to 60 cm and ends in a crown of 15 to 20 palmate leaves arranged in a spiral, approximately 2.5 meters long and 4.5 m wide [14]. The fibres are extracted from their young leaves (bud) to make various products such as bags, roofs of houses, ropes, hammocks, mats, baskets, fishing nets, ceremonial garments, among others [13], the palm and a textile fibre fabric are shown in Fig. 1.

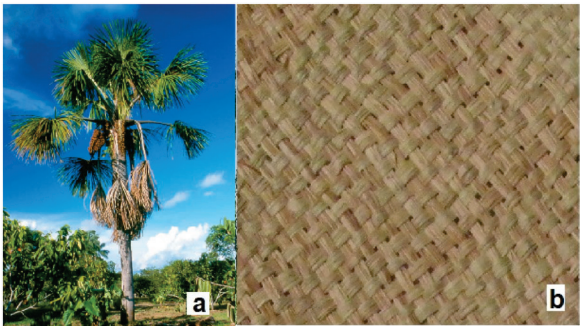

Fig. 1. *a) Moriche palm, and b) textile fibre fabric, (Reproduced from [15])*

1.2 Bio-epoxy Resin Matrix

The matrix to manufacture the bio-composite is a modified liquid epoxy resin (Super Sap CLR epoxy) and a hardener of two speeds: Super Sap INF (fast and slow). Unlike traditional resins composed primarily of petroleum-based materials, Super Sap formulations contain renewable biofuel materials obtained as co-products or from industrial process waste, such as wood pulp and biofuel production [20].

1.3 Fibre Thermogravimetric Analysis (TGA)

The thermal stability of the fibres was evaluated in the laboratory using an SDT Q600 TA Instruments machine, at a heating rate of 10 °C/min, until reaching 600 °C in a nitrogen controlled inert atmosphere. The samples were crushed until obtaining fine size with weights between 5 mg and 10 mg and placed in alumina capsules stable at high temperatures.

The graphs of thermal decomposition: percentage of weight vs temperature (TG) and its first derivative percentage of weight per min vs temperature difference thermo-gravimetry (DTG) for lignocellulosic fibres, generally show a first mass loss, attributed by several authors to the vaporization of the water absorbed into the fibre; the second mass loss process represents the degradation initiation, with thermal stability in the fibres up to about 200 ºC [23].

1.4 Natural Fibres Tensile Test

The mechanical characterization was carried out by tensile testing with the ASTM standard D3822/D3822M-14, (Standard test method for tensile properties of single textile fibres) [16], measured with

a Shimazu UH 600 KNI universal testing machine. The conditions of the test were room temperature (20 °C), deformation speed (1 mm/min), and calibrated length (20 mm).

1.5 Morphology of Natural Fibres (SEM Test)

The microstructure was observed using a scanning electron microscope (JEOL model JSM 6490-LV) with 3.0 nm resolutions, and using a voltage of 30KV with high vacuum isolation, covering the cross-section of the sample with a thin layer of gold to allow conductivity.

1.6 Manufacture of Bio-composite

The braided fibre reinforcement was hand-made by the Tukano and Guayabero Indians of the Panuré reservation in San José del Guaviare, Colombia [24]. To make the fabric they initially extract and dry the fibres, then select the homogeneous threads to interlock them manually until obtaining a uniform, balanced bidirectional fabric at 45°. The resin matrix bio Super Sap CLR epoxy is adequate for the VARTM method in mixed in a ratio of 100: 33 (resin: hardener) by weight, until obtaining a viscosity of 490 cPs to guarantee good fluidity [20].

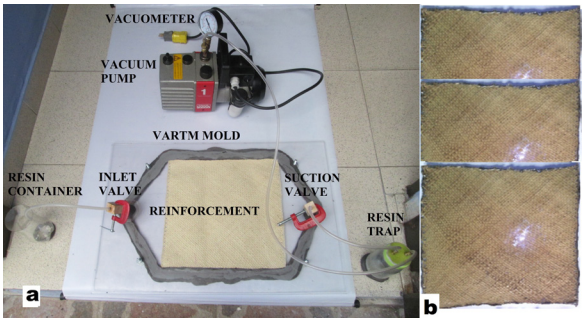

Fig. 2. *a) Assembly for VARTM method, and b) Moriche/bio-epoxy laminate*

The Moriche textile fibre fabric was used without physical-chemical treatments, cutting sections of 20 cm × 30 cm with a grammage of 8.833 g/cm^2. Laminates of the material reinforced with woven fibres were made, using the assembly shown in Fig. 2a. After impregnating all the fibre, the vacuum is maintained by closing the valves (inlet and outlet) for 24 hours for curing. Finally, the laminate is obtained (Fig. 2b).

1.7 Bio-composite Characterization

The specimens were obtained by cutting the bio-composite laminates with dimensions according to ASTM D3039/D3039M-14 [21], for traction in polymer matrix composite materials. The test speed is 1 mm/min at room temperature and 52 % relative humidity. Five specimens with a calibrated length of 100 mm were tested, using a system of flat jaws in the Shimazu UH 600 KNI universal machine.

The bending tests for Moriche/epoxy specimens were adjusted to ASTM D790-15 [22], for non-reinforced, reinforced plastics and insulating materials. The test conditions were at a speed of 2 mm/min and room temperature. Five specimens were tested in the Shimazu UH 600 KNI universal machine, using an accessory for three-point bending, with 100 mm between supports.

2 RESULTS AND DISCUSSION

2.1 Tensile Test of the Fibre

The characteristic behaviour of Moriche fibre when evaluated by ASTM D3822 / 3822M-14 standard [16], is shown in the strength-strain diagram of Fig. 3.

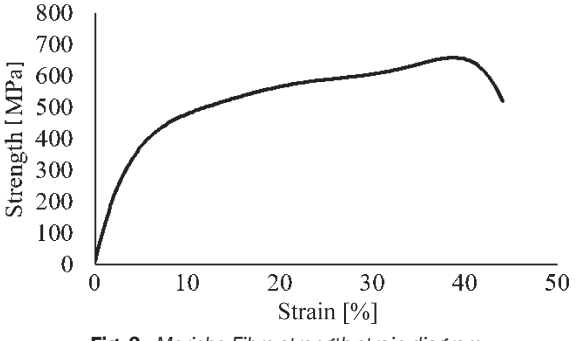

Fig. 3. *Moriche Fibre strength-strain diagram*

Fig. 3 shows an elastic (linear) zone associated to the deformation of the cell wall (cellulose microfibrils) and a plastic zone (non-linear) due to the delamination of cellulose and the orientation of the amorphous phase (lignin, pectin and hemicellulose) [25]. The average values and standard deviation for the modulus of elasticity, the maximum tensile strength and the maximum deformation are presented in Table 1.

The maximum strength in Table 1 shows a low standard deviation value compared with previous investigations for fibres such as flax (1000±500 MPa) [26], okra (233.8±126.4 MPa) [27] and ramie (586.5±351.5 MPa) [28].

Table 1. *Mechanical properties of MPF*

Cross section [mm×mm]	Gage length [mm]	Tensile strength [MPa]	Young's modulus [GPa]	Breaking strain [%]
0.1 × 2	20	585.03 ± 178.4	9.53 ± 2.8	40.57 ± 27.6

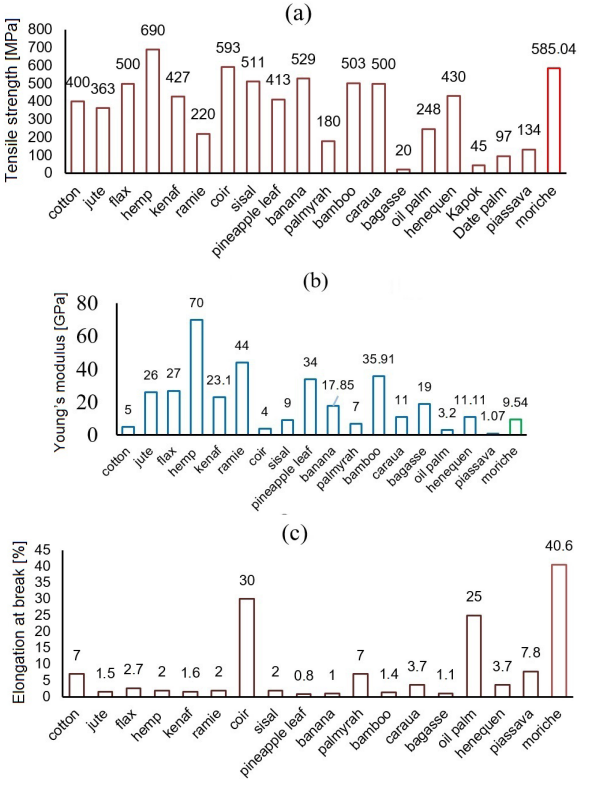

Fig. 4. *a) Tensile strength, b) Young's modulus, and c) elongation at break in various natural fibres vs Moriche fibre, adapted from* [34]

The values of maximum tensile strength allow the selection of MPF as a possible alternative to be used as reinforcement in bio-composite materials by overcoming fibres (Fig. 4a), such as jute [29], kenaf [30], flax [31], sisal [32] and cotton [33], used in the development of these materials. Although the module obtained shows representative variations with respect to fibres such as flax, hemp, jute, ramie, and kenaf; there are similarities between the MPF and the sisal fibre [34], as shown in Fig. 4b. The maximum elongation value of MPF was 40.58 % with elasto-plastic behaviour [35], but higher than most natural fibres, where the coconut fiber [34] obtained a similar value, as shown in Fig. 4c.

2.2 Fibre Thermal Stability

The behaviour of the TG graph of the MPF is shown in Fig. 5.

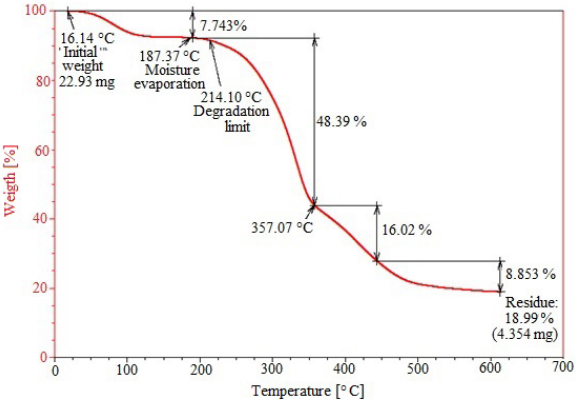

Fig. 5. *TG fibre Moriche curve*

The hydrophilicity or moisture retention in reinforcement with lignocelluloses fibres is one great drawback for polymer composites [36]. The moisture generates a weak interfacial bond; causing the reduction in the mechanical properties of the composite [37].

For MPF, a percentage of humidity of 7.74 % is obtained in a range of (18 °C to 187 °C), similar to that of other fibres such as althaea (25 °C to 135 °C) [28], areca (30 °C to 100 °C) [38], cissus (25 °C to 175 °C) [39], proporis (25 °C to 110 °C) [4] and okra (30 °C to 110 °C) [27]. This percentage generates a negative effect on adhesion, so it is recommended to perform a preliminary physical-chemical treatment before adding it to the matrix.

Maintaining the temperature below the limit of fibre degradation ensures that it maintains its mechanical properties during the manufacturing processes of the bio-composite by extrusion or injection moulding in thermoplastics [18]. The limit of the beginning of the degradation of MPF is given at 214 °C, with values close to other fibres such as artichoke (230 °C), bamboo (214 °C), bagasse (222 °C) [[40], okra (220 °C), hemp (250 °C), curauá (230 °C), kenaf (219 °C) and jute (205 °C) [27].

2.3 Moriche Fibre Morphology

The micrographs of MPF show a uniform distribution of cells along the cut (see Fig. 6), the size of the lumen is large from 8 μm to 10 μm, as well as its cell wall, which in some areas equals the lumen, whose dimensions oscillate between 5 μm and 10 μm. The

fibre tends to be more massive at one end but, in general, its structure is symmetrical.

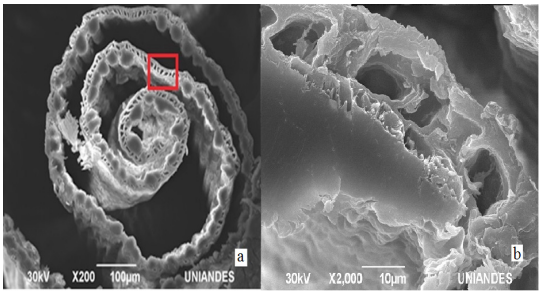

Fig. 6. *Microstructure of MPF at a) ×200 and b) ×2000*

The images obtained have similar morphological characteristics between MPF and other fibres, such as jute, sisal, curaua, coconut, artichoke (Cynara cardunculus L.) **[40]**, piassava **[41]**, okra (Abelmoschus esculentus) **[27]**, marshmallow (Althaea officinalis L) **[28]**, shell of betel nut (Areca catechu) **[38]**, cabecinegro fibre (manicaria saccifera) **[42]**, and sugar cane fibre **[43]**.

As the cell wall is responsible for supporting the force, especially the microfibrils of cellulose, the micrographs of MPF validate the results obtained in the mechanical behaviour, because the axial force is evenly distributed in a larger support area by having robust and symmetrical cell walls.

2.4 Bio-composite Tensile Test

The behaviour of the bio-composite tensile material is shown in Fig. 7.

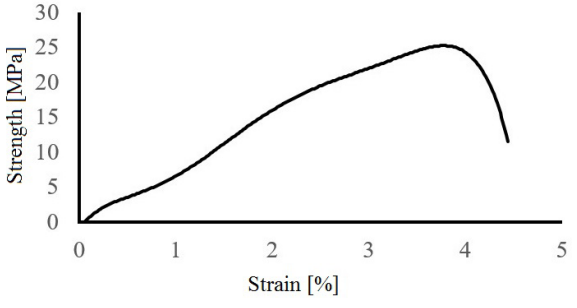

Fig. 7. *Tensile behaviour of MPF-bio-epoxy composite*

The results of Young's modulus averages, maximum tensile strength and strain are shown in Table 2.

The results of the mechanical properties show a fragile behaviour due to the low percentages in the strain. In contrast, the differences are more significant in the resistance and the module. The behaviour in the stiffness, measured with the elastic modulus was diminished by almost a third for the MPF. The possible cause of this variation is mainly due to the low compatibility of the reinforcements with bio-epoxy resin, attributed to excess moisture in the fibre, affecting the adhesion. The low value of strength is a consequence of the delamination of the reinforcement when subjected to axial forces due to tissue orientation.

Table 2. *Properties of the MPF bio-composite*

Properties	MPF/bio-epoxy
Tensile strength [MPa]	25.02 ± 0.48
Young's modulus [GPa]	9.17 ± 7.00
Breaking strain [%]	3.77 ± 0.65

2.5 Bio-composite Flexural Test

In Fig. 8, an elastoplastic behaviour is observed, in the first elastic zone, the flexural modulus has similar values (slope); however, the strengths have more dispersed behaviours in the plastic zone.

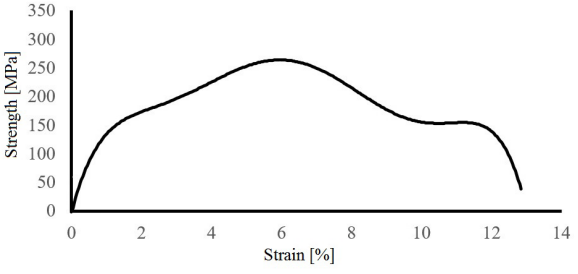

Fig. 8. *Flexural behaviour of MPF-bio-epoxy composite*

The strength in the plastic area presents a small variation that is due to the alignment of the microfibrils after the delamination of the amorphous and crystalline components in the direction of the load. This behaviour occurs below the neutral axis where the specimen is located in traction. The strength in the upper part depends only on the resin because the reinforcement does not act in compression.

The average values of strength to flexion, modulus and strain were obtained by descriptive statistics; the results are shown in Table 3.

Table 3. *Average values of strength, strain and flexural modulus for the MPF bio-composite*

Properties	MPF/bio-epoxy
Flexural strength [MPa]	253.75 ± 43.31
Flexural modulus [GPa]	10.9 ± 2.0
Breaking strain [%]	28.45 ± 3.75

The mechanical properties of tensile/flexural strength and Young's modulus were compared with other polymer matrix bio-composites evaluated by different authors. Table 4 shows the results obtained.

Table 4. *Mechanical properties of various bio-composites developed vs MPF-bio-epoxy*

Composite	Tensile strength [MPa]	Flexural strength [MPa]	Young's modulus [GPa]	Ref.
sisal/polyester	40	77	2.13	[44]
jute/polyester	66.01	93.8	4.42	
coco/polyester	20.4	41.54	1.2 to 2	
banana/cotton/polyester	30.96	61.24	2.03	
Pineapple leaf/polyester	43.38	85.81		
jute/epoxy	104	150	15.04	
bamboo/PBS	32	40.5	0.9	
Oil palm/ HDPE	12.5	248.1	0.39	
Straw/PP	33	1200	1.18	
Abaca/PLA	74	-	8.34	[1]
Abaca/PP	42	-	4.9	
Flax/PP	42	67	3.2	
Hemp/PP	42	70	3	
Moriche/Bio-epoxy	25.02	253.74	9.17	

The composite developed with MPF and bio-epoxy resin obtained intermediate values between the coconut/polyester composite and the banana/cotton/polyester tested under traction. In contrast, the comparison of flexural strength presents higher values than those reported in other investigations that are only surpassed by the straw/PP composite.

These results define a limited application only in components that do not need to be of a structural type or that are subjected to high loads and whose tensile strengths do not exceed 25 MPa. Regarding the values of flexural strength, the results allow wider applications in parts subjected to concentrated or distributed loads, either double-supported or cantilevered.

2.6 Microstructure of the Bio-composite

In Fig. 9, the three zones of the bio-composite are observed, the reinforcement (MPF), the matrix (bio-epoxy resin) and the interface between the two materials. It is worth noting again the poor adhesion between the micro-constituents, showing an interface with a separation between materials close to 20 μm. The absence of interaction between the natural fibre and the bio-epoxy resin proves the low mechanical properties of this system, causing the composite to be delaminated under the effect of the axial force applied in the tensile test.

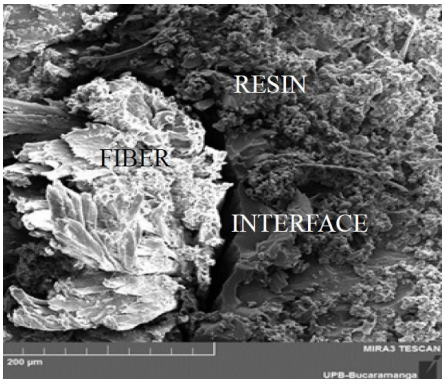

Fig. 9. *Micrography of MPF/bio-epoxy composite*

As explained in the TGA test, the natural fibre is hydrophilic, that is, they tend to retain a significant percentage of moisture, and as a consequence, the interfacial junctions with the hydrophobic matrix are affected, decreasing the mechanical properties of the bio-composite.

3 CONCLUSIONS

Mechanical tests showed that the MPF is a good alternative for reinforcement in bio-composite polymer matrix materials, due to its excellent tensile strength properties with respect to various fibres investigated by other authors.

The thermal analysis enabled determining both the moisture content of the fibre and the limit of the beginning of degradation of the fibre, defining with these results the need for a previous drying process and the type of matrix that can be used. With these parameters, the loss of mechanical properties due to excess temperature in the manufacturing process is avoided. The effect of moisture on the mechanical properties was evidenced in the results obtained for the bio-composite.

The scanning electron microscopy enabled understanding the direct relationship that exists between the results of the mechanical tests and the microstructure of the fibre, allowing to observe a robust cell wall, where the axial load to which the fibre is subjected is distributed in a uniform way. In the case of the bio-composite, it was possible to demonstrate a very poor adhesion between the fibre and the matrix.

The low tensile strength value is also due to the orientation of the fibres in the fabric used, so it is advisable to manufacture a uniform balanced fabric at

90° so that the reinforcement is oriented properly in the direction of the loads.

Once the mechanical, thermal, and morphological properties of the fibre and Moriche-bio-epoxy composite have been compared with other compounds reinforced with natural fibres, it is demonstrated that the MPF has a very high potential in the field of environmentally friendly materials, making a pre-treatment to improve adhesion.

4 ACKNOWLEDGEMENTS

This research study was supported by the University of Pamplona – Colombia. The authors declare that there is no conflict of interest regarding the publication of this paper.

5 REFERENCES

[1] Anshu, A., Singh, Afrin, S., Karim, Z. (2017). Green Composites: Versatile Material for Future. M. Jawaid et al. (eds.) *Green Biocomposites, Green Energy and Technology*, p. 30-44, Springer, Cham, **DOI:10.1007/978-3-319-49382-4_2**.

[2] Saba, N., Jawaid, M., Alothman, O.Y., Paridah, M.T. (2016). A review on dynamic mechanical properties of natural fibre reinforced polymer composites. *Construction and Building Materials*, vol. 106, p. 149-159, **DOI:10.1016/j.conbuildmat.2015.12.075**.

[3] Pereira, P.H.F., Rosa, M. de F., Cioffi, M.O.H., Benini, K.C.C. de C., Milanese, A.C., Voorwald, H.J.C., Mulinari, D.R. (2015). Vegetal fibers in polymeric composites: a review. *Polímeros*, vol. 25, no. 1, p. 9-22, **DOI:10.1590/0104-1428.1722**.

[4] Fiore, V., Scalici, T., Valenza, A. (2014). Characterization of a new natural fiber from Arundo donax L. as potential reinforcement of polymer composites. *Carbohydrate Polymers*, vol. 106, p. 77-83, **DOI:10.1016/j.carbpol.2014.02.016**.

[5] Kommula, V.P., Kanchireddy, O.R., Shukla, M., Marwala, T. (2014). Effect of acid treatment on the chemical, structural, thermal and tensile properties of napier grass fibre strands. *International Conference on Advances in Marine, Industrial and Mechanical Engineering*, Johannesburg, p. 45-51.

[6] Ramesh, M., Palanikumar, K., Hemachandra Reddy, K. (2017). Plant fibre based bio-composites: Sustainable and renewable green. *Renewable and Sustainable Energy Reviews*, vol. 79, p. 558-584, **DOI:10.1016/j.rser.2017.05.094**.

[7] AL-Oqla, F.M., Sapuan, S.M. (2014). Natural fiber reinforced polymer composites in industrial applications: feasibility of date palm fibers for sustainable automotive industry. *Journal of Cleaner Production*, vol. 66, p.347-354, **DOI:10.1016/j.jclepro.2013.10.050**.

[8] Murat, B.I.S., Fromme, P., Endrizzei, M., Olivo, A. (2018). Characterization of Impact Damage in Composite Plates. *Strojniški vestnik - Journal of Mechanical Engineering*, vol. 64, no. 11, p. 672-680, **DOI:10.5545/sv-jme.2017.5186**.

[9] Barari, B., Omrani, E., Moghadam, A.D., Menezes, P.L., Pillai, K.M., Rohatgi, P.K. (2016). Mechanical, physical and tribological characterization of nano-cellulose fibers reinforced bio-epoxy composites: An attempt to fabricate and scale the 'Green' composite. *Carbohydrate Polymer*, vol. 147, p. 282-293, **DOI:10.1016/j.carbpol.2016.03.097**.

[10] Moreno, L.A., Andrade, G.I., y Ruíz-Contreras, L.F. (eds.). (2016). *Biodiversity 2016. Status and Trends of Continental Biodiversity in Colombia*. Research Institute of Biological Resources Alexander von Humboldt. Bogotá, D.C., Colombia. 106 p.

[11] García, N., Galeano, G., Mesa, L., Casta-o, N., Balslev, H., Bernal, R. (2015). Management of the palm Astrocaryum chambira Burret (Arecaceae) in northwest Amazon. *Acta Botanica Brasilica*, vol. 29, no. 1, p. 45-57, **DOI:10.1590/0102-33062014abb3415**.

[12] Artesanias de Colombia, (2014). from h*ttp://www.artesaniasdecolombia.com.co*.

[13] Mesa Castellanos, L., Toro Buitrago, A., Isaza Aranguren, C. (2017). Management of Mauritia flexuosa l.f. for the production of crafts in the Colombian highlands. *Forest Colombia*, vol. 20. p. 85-101, **DOI:10.14483/udistrital.jour.colomb.for.2017.1.a07**. (in Spanish)

[14] Virapongse, A., Endress, B.A., Gilmore, M.P., Horn, C., Romulo, C. (2017). Ecology, livelihoods, and management of the Mauritia flexuosa palm in South America. *Global Ecology and Conservation*, vol. 10, p. 70-92, **DOI:10.1016/j.gecco.2016.12.005**.

[15] SINCHI Institute and Corpoamazonia (2007). *Ecology, use and sustainable management of nine species of plants from the department of Amazonas, generators of timber and non-timber products*. Ministry of environment, housing and territorial development, Bogotá (Colombia). (in Spanish)

[16] ASTM D3822/D3822M:2014. *Standard Test Method for Tensile Properties of Single Textile Fibers*. American Society for Testing and Materials. USA.

[17] Jose Chirayil, C., Mathew, L., Thomas, S. (2014). Review of recent research in nano cellulose preparation from different lignocellulosic fibers. *Reviews on Advanced Materials Science*, vol. 37, no.1-2, p. 20-28.

[18] Pickering, K.L., Aruan Efendy, M.G., Le T.M. (2016). A review of recent developments in natural fibre composites and their mechanical performance. *Composites Part A: Applied Science and Manufacturing*, vol. 83, p. 98-112, **DOI:10.1016/j.compositesa.2015.08.038**.

[19] Schuster, J., Govignon, Q., Bickerton, S. (2014). Processability of biobased thermoset resins and flax fibres reinforcements using vacuum assisted resin transfer moulding. *Open Journal of Composite Materials*, vol. 4, no. 1, p. 1-11, **DOI:10.4236/ojcm.2014.41001**.

[20] Entropy resins, Super Sap INF System Entropy Resins Inc. (2016). from *https://entropyresins.com/product/super-sap-clr-clear-epoxy-resin/*, accessed on 2016-03-12.

[21] ASTM D3039/D3039M:2014. *Standard Test Method for Tensile Properties of Polymer Matrix Composite Materials*. American Society for Testing and Materials. USA.

[22] ASTM D790:2015. *Standard Test Method for Flexural Properties of Unreinforced and Reinforced Plastics and Electrical Insulating Materials. American Society for Testing and Materials.* USA.

[23] Maache, M., Bezazi, A., Amroune, S., Scarpa, F., Dufresne, A. (2017). Characterization of a novel natural cellulosic fiber from Juncus effusus L. *Carbohydrate Polymers*, vol. 171, p. 163-172, **DOI:10.1016/j.carbpol.2017.04.096**.

[24] Municipality of San Jose del Guaviare (2008). *Comprehensive Plan for Indigenous Life - Panuré Resguardo*, Department of Guaviare, San José del Guaviare. (in Spanish)

[25] Fiore, V., Scalici, T., Valenza, A. (2014). Characterization of a new natural fiber from Arundo donax L. as potential reinforcement of polymer composites. *Carbohydrate Polymers*, vol. 106, p. 77-83, **DOI:10.1016/j.carbpol.2014.02.016**.

[26] Hughes, M. (2012). Defects in natural fibres: their origin, characteristics and implications for natural fibre-reinforced composites. *Journal of Materials Science*, vol. 47, no. 2, p. 599-609, **DOI:10.1007/s10853-011-6025-3**.

[27] De Rosa, I.M., Kenny, J.M. Maniruzzaman, M., Moniruzzaman, M., Monti, M., Puglia, D., Santulli, C., Sarasini, F. (2011). Effect of chemical treatments on the mechanical and thermal behaviour of okra (Abelmoschus esculentus) fibres. *Composites Science and Technology*, vol. 71, no. 2, p. 246-254, **DOI:10.1016/j.compscitech.2010.11.023**.

[28] Sarikanat, M., Seki, Y., Sever, K., Durmuskahya, C. (2014). Determination of properties of Althaea officinalis L. (Marshmallow) fibres as a potential plant fibre in polymeric composite materials. *Composites Part B, Engineering*, vol. 57, p. 180-186, **DOI:10.1016/j.compositesb.2013.09.041**.

[29] Sanjay, M.R., Madhu, P., Jawaid, M., Senthamaraikannan, P., Senthil, S., Pradeep, S. (2018). Characterization and properties of natural fiber polymer composites: A comprehensive review. *Journal of Cleaner Production*, vol. 172, p. 566-581, **DOI:10.1016/j.jclepro.2017.10.101**.

[30] Faruk, O., Bledzki, A.K., Fink, H.-P., Sain, M. (2014). Progress report on natural fiber reinforced composites. *Macromolecular Materials and Engineering*, vol. 299, no. 1, p. 9-26, **DOI:10.1002/mame.201300008**.

[31] Moothoo, J., Allaoui, S., Ouagne, P., Soulat, D. (2014). A study of the tensile behaviour of flax tows and their potential for composite processing. *Materials & Design*, vol. 55, p. 764-772, **DOI:10.1016/j.matdes.2013.10.048**.

[32] Senthilkumar, K., Saba, N., Rajini, N., Chandrasekar, M., Jawaid, M., Siengchin, S., Alotman, O.Y. (2018). Mechanical properties evaluation of sisal fibre reinforced polymer composites: A review. *Construction and Building Materials*, vol. 174, p. 713-729, **DOI:10.1016/j.conbuildmat.2018.04.143**.

[33] Layth, M., Ansari, M.N.M., Pua, G., Jawaid, M., Islam, M.S. (2015). A review on natural fiber reinforced polymer composite and its applications. *International Journal of Polymer Science*, vol. 2015, p. 1-15, **DOI:10.1155/2015/243947**.

[34] Müssig, J. (ed.) (2010). *Industrial Applications of Natural Fibres. Structure, Properties and Technical Applications,* University of Applied Sciences, John Wiley & Sons, Bremen, **DOI:10.1002/9780470660324**.

[35] Fuentes, C.A., Willekens, P., Petit, J., Thouminot, C, Müssig, J., Trindade, L.M., Van Vuure, A.W. (2017). Effect of the middle lamella biochemical composition on the non-linear behaviour of technical fibres of hemp under tensile loading using strain mapping. *Composites Part A: Applied Science and Manufacturing*, vol. 101, p. 529-542, **DOI:10.1016/j.compositesa.2017.07.017**.

[36] Stanciu, M.D., Savin, A., Nastac, S. (2018). Mechanical and surface properties of lignocellulosic fibres reinforced composites. *Strojniški vestnik - Journal of Mechanical Engineering*, vol. 64, no. 11, p. 698-705, **DOI:10.5545/sv-jme.2018.5352**.

[37] Ridzuan, M.J.M., Abdul Majid, M.S., Afendi, M., Aqmariah Kanafiah, S.N., Zahri, J.M., Gibson, A.G. (2018). Characterisation of natural cellulosic fibre from Pennisetum purpureum stem as potential reinforcement of polymer composites. *Materials & Design*, vol. 89, p. 839-847, **DOI:10.1016/j.matdes.2015.10.052**.

[38] Yusriah, L., Sapuan, S.M., Zainudin, E.S., Mariatti, M. (2014). Characterization of physical, mechanical, thermal and morphological properties of agro-waste betel nut (Areca catechu) husk fibre. *Journal of Cleaner Production*, vol. 72, p. 174-180, **DOI:10.1016/j.jclepro.2014.02.025**.

[39] Indran, S., Edwin Raj, R., Sreenivasan, V.S. (2014). Characterization of new natural cellulosic fiber from Cissus quadrangularis root. *Carbohydrate Polymers*, vol. 110, p. 423-429, **DOI:10.1016/j.carbpol.2014.04.051**.

[40] Fiore, V., Valenza, A., Di Bella, G. (2011). Artichoke (Cynara cardunculus L.) fibres as potential reinforcement of composite structures. *Composites Science and Technology*, vol. 71, no. 8, p. 1138-1144, **DOI:10.1016/j.compscitech.2011.04.003**.

[41] Alves Fidelis, M.E., Castro Pereira, T.V., Martins Gomes, O.F., Silva, F.A., Toledo Folho, R.D. (2013). The effect of fiber morphology on the tensile strength of natural fibers. *Journal of Materials Research and Technology*, vol. 2, no. 2, p. 149-157, **DOI:10.1016/j.jmrt.2013.02.003**.

[42] Porras, A., Maranon, A., Ashcroft, I.A. (2016). Thermo-mechanical characterization of Manicaria Saccifera natural fabric reinforced poly-lactic acid composite lamina. *Composites Part A: Applied Science and Manufacturing*, vol. 81, p. 105-110, **DOI:10.1016/j.compositesa.2015.11.008**.

[43] Hossain, M.K., Karim, M.R., Chowdhury, M.R., Imam, M.A., Hosur, M., Jeelani, S., Farag, R. (2014). Comparative mechanical and thermal study of chemically treated and untreated single sugarcane fiber bundle. *Industrial Crops and Products*, vol. 58, p. 78-90, **DOI:10.1016/j.indcrop.2014.04.002**.

[44] Mohanty, A.K., Misra, M., Drzal, L.T. (2005). Natural Fibers, Biopolymers and Biocomposites. Taylor & Francis Group, New York, **DOI:10.1201/9780203508206**.

Strojniški vestnik - Journal of Mechanical Engineering 65(2019)3, 189-197

DOI:10.5545/sv-jme.2018.5651 Original Scientific Paper
Received for review: 2018-07-16
Received revised form: 2019-02-27
Accepted for publication: 2019-03-06

An Exacting Wall-Penetration Pipe Analysis

Pino Koc*
University of Ljubljana, Faculty of Mathematics and Physics, Slovenia

Conventional analysis methods for piping systems have incorporated many conservative assumptions. Some of these assumptions can be abandoned by employing advanced analyses, thus allowing for higher loads, which can lead to further uprating of the system without physically intervening with it.

This paper shows the procedure of uprating the design seismic load of an existing pipeline through advanced analyses. First, it was discovered that the seal between the pipe and the wall in fact represents a support which is even stiffer than an engineered, purposely built support. Secondly, analyses demonstrate that a pipeline built of thin wall pipes can sustain significant lateral deformation (ovalization and indentation), imposed by seismically induced relative displacements between the buried pipe and building wall penetration, without breaching the pipe wall. This finding is supported by the fact that the pipe passed the flattening test. In the pipeline qualification procedure, the stress state in the dented pipe wall is compared with the stress state during the flattening test. All relevant stress indicators (stress intensities) at the uprated loading state were smaller than allowed by the applicable code or obtained from the flattening test; thus, the pipeline qualified for uprated seismic conditions.

Keywords: dented pipeline, seismic, ASME, stress categorization, Link-Seal

Highlights

- *During a strong earthquake, the Link-Seal sealing system is insufficient to compensate for relative displacements between the pipe and the wall. It becomes a support.*
- *Ovalization and pipe wall indentation at the piping supports are significant modes of deformation for thin-walled pipes.*
- *Successfully passing the pipe flattening test serves to determine an upper-limit stress state in the pipe.*
- *The stress linearization procedure is applied to a highly plastically deformed pipe wall.*

0 INTRODUCTION

Existing piping systems sometimes need to operate at larger mechanical loads than they are originally designed to. Often, these beyond-the-original-design loads lessen the margin against piping failure so much that performing recalculations using original analysis methods cannot qualify the pipeline. To demonstrate suitability of the existing pipeline to increased loads and to avoid piping hardware modification, more advanced analysis methods need to be employed.

In this paper, a single detail from the beyond-the-original-design analysis [1] of a buried thin-wall water pipeline in nuclear power plant (NPP) Krško is shown. That analysis, the description of which is beyond the aim of this paper, demonstrated that the most critical part of the system is the penetration of the buried pipeline into a power plant's concrete building. Namely, because of a supposed beyond-the-original-design earthquake, relative displacements between the building's basement wall and the surrounding soil evolve, which in turn imposes large deformation on a buried pipe at the site of the building wall's penetration. The most significant mode of deformation is pipe denting at the pipe-to-concrete-wall seal location.

Pipe denting strongly influence pipeline's strength and fatigue life; therefore, the topic was addressed by researchers in the past [2] and [3] and is still attractive today [4] to [6]. The solutions to the problem are in the form of a pure theoretic analysis [2], or as guides extracted from recapitulation of many experiments [3], or, recently, from experiments supplemented with numerical analyses [4] to [6]. All researchers agree that the excessive size of the dent, the abrupt change of the dented surface curvature and the pre-existing pipe damage on the dent spot severely lessen pipe strength and fatigue life. Because the denting is a problem still under research, it is not included in piping structural design codes yet, therefore leaving the structural engineer on thin ice.

The aim of this paper is twofold: describing the experimental-numerical analysis of the dented section of a pipeline at NPP Krško and demonstrating the pipeline qualification with the applicable American Society of Mechanical Engineers (ASME) Code [7] (which is the obligatory code for NPP Krško), although no rule regarding dents is given in [7].

*Corr. Author's Address: University of Ljubljana, Faculty of Mathematics and Physics, Slovenia, pino.koc@fmf.uni-lj.si

1 METHODS

1.1 General Procedure and Acceptance Criteria

Stresses beyond those allowable were obtained at the pipeline penetration by analysing a beyond-the-design loading condition using ordinary design methods, i.e., finite element modelling with pipeline approximation based on beam's finite elements (AutoPipe code, for example) [1]. However, investigation of the problem revealed that by employing unconventional piping analysis methods, an acceptable solution can be found without pipe penetration modification while respecting applicable standards and codes [7]. The whole analysis procedure can be divided into the following steps:

1) Defining material data through a literature search and by the numerical simulation of the experiment; where the experiment itself was performed by others.
2) Cooperating with analysts of the global pipeline model to tune both the global and the local (detailed) model and harmonize their responses.
3) Determining the strain-stress state in the local model.
4) Interpreting the obtained strain-stress state according to code [7] rules.

Acceptance criteria are given in the ASME Code [7] in the form of allowable stresses which are dependent on the material, external loading behaviour and the sort of stress which develops inside the investigated cross-section. In our case, the pipe material is carbon steel SA 106 Grade B [8]. The loading is given in the form of a set of axial and lateral earthquake-induced relative displacements, with a magnitude of several centimetres, between the basement concrete wall and the pipe. The sorts of stresses which need to be checked in the case of extreme loading are primary membrane stress P_m and primary bending stress P_b.

The functionality criterion given in plant specifications and reprinted in [1] is that a pipeline must maintain operability during and after a major earthquake. This means that the pipeline may deform, even permanently, but must convey cooling water in all circumstances.

1.2 Defining Mechanical Properties

1.2.1 Yield Curve

The ASME [8] provides enough material properties data to perform elastic analyses. However, regarding elastic-plastic material response, only tensile strength is given in [8]. To define the yield curve properly, additional information was found in [12] and in a certified test report on the piping material [1]. The yield curve, which was used in all computer simulations, is shown in Fig. 1.

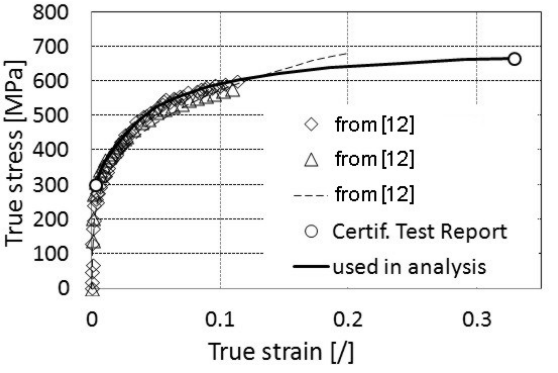

Fig. 1. *Yield curve justification*

1.2.2 Pipe Flattening Test

When the pipeline is manufactured, each pipe from which the pipeline is assembled needs to pass a pipe-flattening test. In the test, described in the steel SA-106 specification [8], a short section, 63.5 mm (2.5 inch) in length, is sliced from each pipe to be used in a pipeline, to obtain a ring, which is then flattened cold between parallel platens until the required distance between the platens is achieved. In our case, for a pipe with outer diameter D = 610 mm (24 inch) and wall thickness t = 9.52 mm (3/8 inch), this distance is 119 mm. No signs of fracture should be seen on the flattened pipe. The test itself is excellent proof of how much local bending a pipe can sustain. Therefore, it is safe to assume that the stress-strain state from the flattening test represents an upper limit which should not be exceeded during any loading conditions.

1.2.3 Numerical Simulation of Pipe Flattening Test

To obtain the flattened pipe stress-strain state, a numerical simulation of the flattening test was performed using the finite element code ABAQUS [9]. Due to the symmetry, only ¼ of the pipe circumference is modelled (Fig. 2). The finite element model consists of 5,600 continuum plane stress elements and a rigid platen (Fig. 2a). The mechanical contact is established between the platen and the outer surface of the pipe. Altogether, the model contains 33,000 variables. The

final stress and strain states are shown in Figs. 2b and c, respectively.

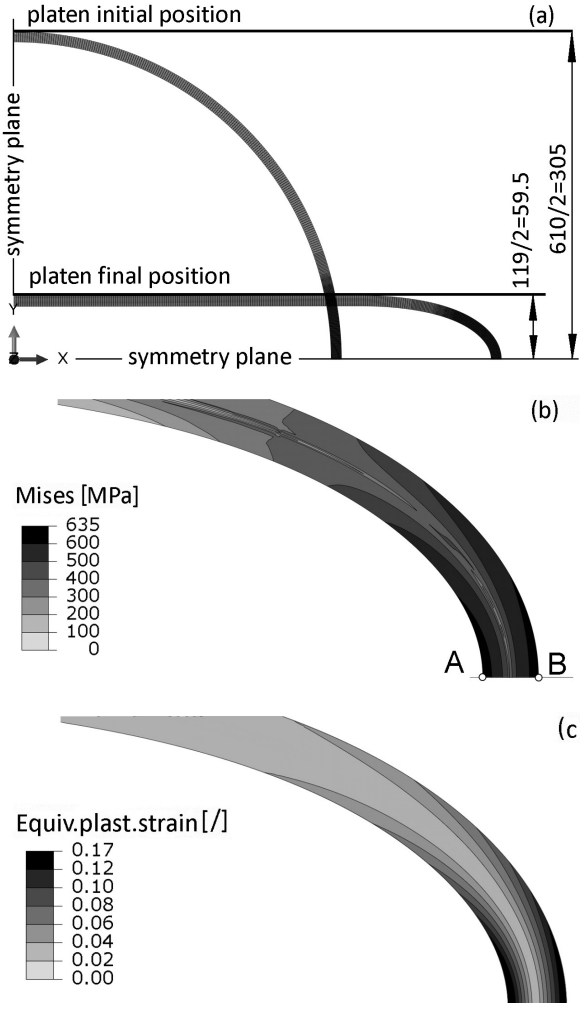

Fig. 2. *Flattening test simulation: a) kinematics; b) equivalent von Mises stress; and c) equivalent plastic strain*

The most stressed and strained part of the pipe is the most curved part of the pipe wall, where the von Mises equivalent stress is 635 MPa, and the equivalent plastic strain at the same material point is 0.17. The mentioned stress of 635 MPa is called the *total stress* and according to the ASME **[7]** needs to be decomposed into primary membrane P_m, primary bending P_b and peak stress F using a stress-linearization procedure. First, a stress path line is defined, denoted by the AB line through the pipe wall (Fig. 2b). The intensity of the radial and circumferential components of the stress tensor along the AB path is depicted in Fig. 3, where point A corresponds with the zero wall-thickness coordinate. From the circumferential stress diagram, it can be seen that inelastic bending is the prevailing loading on the path.

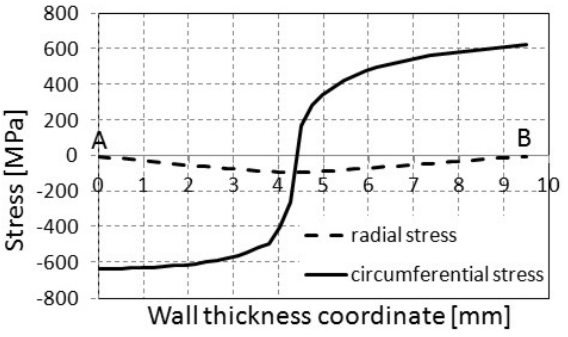

Fig. 3. *Stress components on the most critical stress path for the flattening test*

Next, for each stress tensor component s_{ij} the membrane (average stress across the pipe wall thickness) and bending stress (stress, linearized across the wall so that the net force is zero) need to be calculated according to Eq. (1) and Eq. (2), respectively:

$$\sigma_{ij,memb} = \frac{1}{t}\int_0^t \sigma_{ij}\, dx, \tag{1}$$

$$\sigma_{ij,bend} = \frac{6}{t^2}\int_0^t \sigma_{ij}\left(\frac{t}{2} - x\right) dx, \tag{2}$$

with t denoting the wall thickness at the end of simulation and x representing the local axis aligned along the stress path line from point A towards point B.

Finally, when all components of the membrane and bending stress tensors are obtained, the equivalent von Mises stress is calculated for each of the tensors. For the abovementioned flattening test, the procedure yields the following stress intensities: equivalent stress from membrane stress tensor P_m = 55.7 MPa and equivalent stress from the sum of the membrane and bending stress tensors at point A (inner surface of the pipe), $(P_m + P_b)_A$ = 846 MPa, and at point B (outer surface of the pipe), $(P_m + P_b)_B$ = 912 MPa. It is worth mentioning that P_m is reasonably low due to the prevailing bending of the pipe wall and that the allowable membrane stress according to the ASME **[7]** is $0.7s_{ult} = 0.7\times666 = 466$ MPa.

The stress intensities P_m and $(P_m + P_b)_B$ will serve as allowable stresses for qualifying pipelines according to the ASME Code **[7]**. As expected, the membrane plus bending stresses are extremely high, even higher than the ultimate stress at the material breaking point (see Fig. 1). Such an unreasonable

result is a consequence of the stress-linearization procedure applied to the highly plastically deformed pipe wall. These high stresses cannot be used independently; they can serve only as stress limits in cases with a similar loading pattern, i.e., inelastic pipe wall bending.

1.3 Interaction between Global and Local Model

1.3.1 Ovalization and Indentation Stiffness

The analysed pipeline is made of thin-walled pipes ($D/2t$ = 610 / (2×9.52) = 32) which are susceptible to local radial loading. Thus, for the considered several-centimetre range of relative displacements, ovalization of the pipe cross-section and indentation of the pipe wall, rather than the bending of the pipe centreline, are the dominant modes of pipe deformation at the supports. These two modes are the main deformation patterns regarding how to "consume" the imposed relative displacement at the wall penetration point. The pipe centreline is displaced through these two deformation modes, although parts of the pipe wall in contact with a supporting structure will remain at the same place.

The global pipeline model built of beam finite elements [1] cannot handle ovalization and indentation deformation modes, but it can consider elastic supports, i.e., springs. Therefore, to mitigate the consequences of large relative displacements at the penetration point, springs with stiffness equivalent to the ovalization and indentation stiffness of the pipe wall are determined in separate detailed numerical models and then included in the global beam model at the piping support and seal.

1.3.2 Equivalent Stiffness at the Guide Restraint

Equivalent stiffness was determined through separate analysis of the pipe section with its support in a shell 3D model (Fig. 4). While the pipe is deformable, and its material obeys the elastic-plastic material behaviour from Fig. 1, the guide restraint support itself, i.e., the square-like structure around the pipe, which allows for axial movement of the pipe but prevents lateral displacement, is considered rigid due to the heavy I-beams which constitute the support. The contact surfaces with prescribed initial gaps between the pipe wall and the guide support pads are modelled as well. At the nodes on both pipe ends, kinematic constraints are imposed such that the displacement of these nodes is coupled on translation and rotation of the reference nodes, positioned at the pipe centreline. The pipe's loading is given in the form of the vertical displacement of both reference nodes. During the simulation, displacements of two pipe points on a pipe cross-section at the support and the support reaction force are monitored (Fig. 5) and presented as a graph, shown in Fig. 9. This graph is used in the global pipeline beam model [1] to determine the guide support's equivalent lateral spring stiffness.

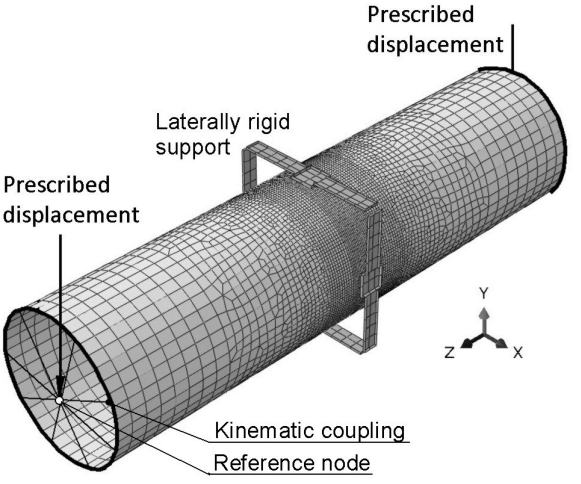

Fig. 4. *Equivalent stiffness determination: pipe and guide support model*

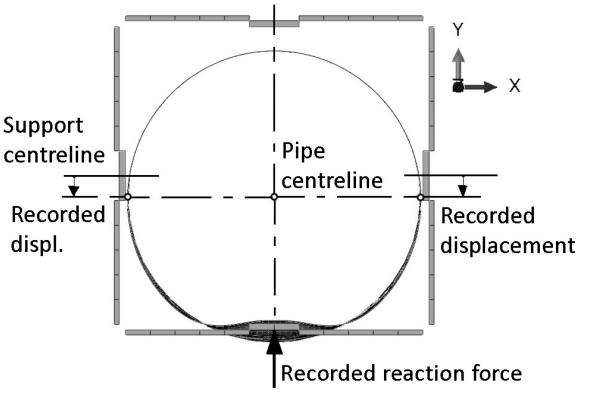

Fig. 5. *Equivalent stiffness determination: pipe centreline displacement on guide support*

1.3.3 Equivalent Stiffness at Link-Seal

Although the Link-Seal [10] is not expected to act as a support, due to its design, which impedes excessive lateral movement of the pipe, the Link-Seal's stiffness should be accounted for in analyses. The seal material is ethylene propylene diene monomer (EDPM) rubber with Shore A hardness 50, which corresponds to a modulus of elasticity of 2.0 MPa. Force-dispersion pressure plates and bolts are made of steel. The

metal sleeve, with which the Link-Seal is in contact, is embedded in a concrete wall and acts as a rigid support for the Link-Seal (Figs. 6 and 7).

Pre-compression of the EDPM and its expansion in a radial direction during the installation of the Link-Seal are not considered in the model.

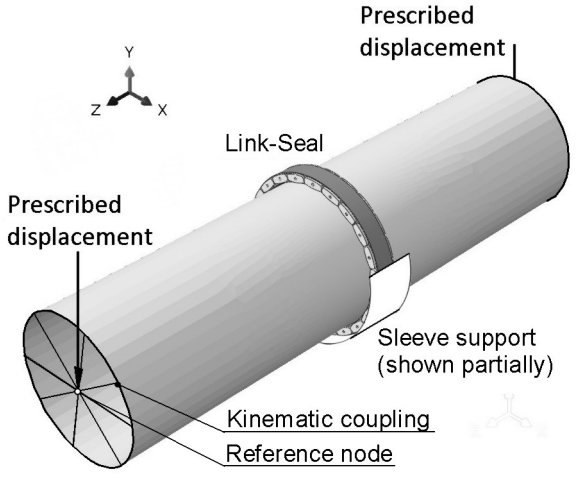

Fig. 6. *Equivalent stiffness determination: pipe and Link-Seal support model*

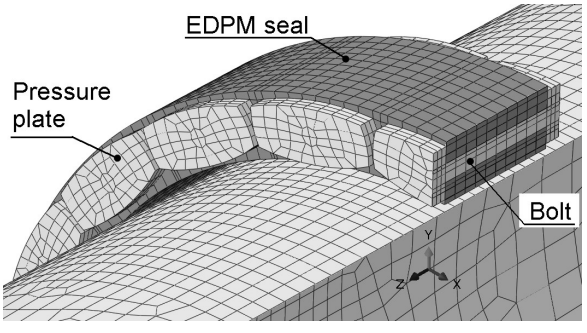

Fig. 7. *Equivalent stiffness determination: pipe and Link-Seal detail*

As with the guide-support case (Section 2.3), the loading of the pipe is given in the form of displacement of both pipe ends. In Fig. 8, the cross section of the pipe at the Link-Seal is shown in the position at which the centreline downward displacement is 24.7 mm. The Link-Seal pressure plates at the lower part of the seal circumference create an obstacle against which the pipe wall locally bends. On the upper part of the cross-section, a gap between the seal and the pipe wall is formed. The reaction force vs. pipe centreline displacement graph, corresponding to the simulated downward movement of the pipe, is given in Fig. 9. The Link-Seal support is, in fact, much stiffer than the guide support. Therefore, it would be a big mistake if the Link-Seal were not considered in a beam model [1] as a support.

Note that in Fig. 7, only the shell mid-thickness surface is shown for the pipe wall's finite elements. The contact algorithm accounts for the shell's thickness; therefore, the pipe in Fig. 7 is in contact with the EDPM seal along the circumference, and the seal is in contact with the metal sleeve.

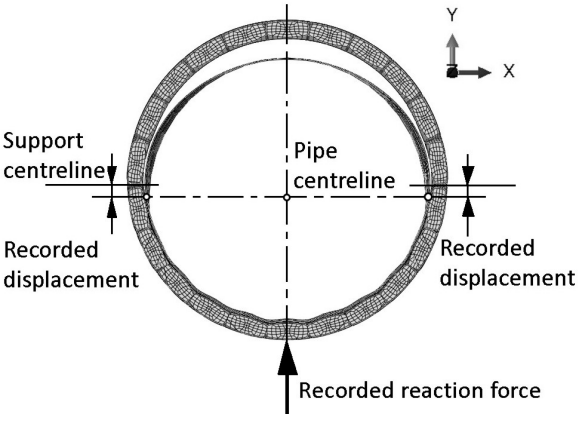

Fig. 8. *Equivalent stiffness determination: pipe centreline displacement on Link-Seal*

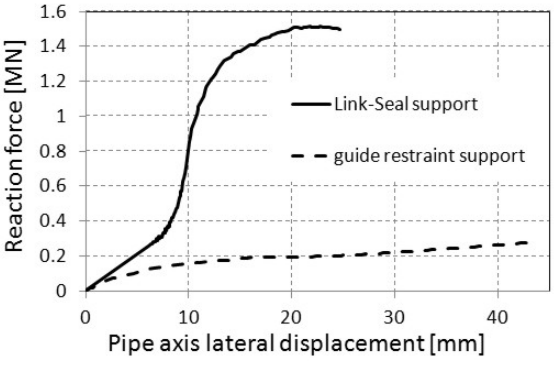

Fig. 9. *Support lateral response*

2 ANALYSIS

2.1 Finite Element Model

The finite element model of the pipe penetration through the wall is a combination of the two models described in Sections 1.3.2 and 1.3.3. The model, shown in Fig. 10, consists of 28,000 shell elements (S4R) with reduced integration; 11 integration points along the thickness direction, representing the pipe; and 13,400 solid elements representing the seal material, dispersion pressure plates and bolts. Altogether, the model contains 339,000 variables.

The model is supported at the sleeve and at the support pads. Contact is possible between the pipe and support pads, between the sleeve and Link-Seal elements and between the pipe and Link-Seal elements. The friction coefficient is 0.8 between the seal and the pipe and 0.2 between the pipe and support pads. A kinematic coupling between the pipe nodes and a reference node is established at both ends of the pipe.

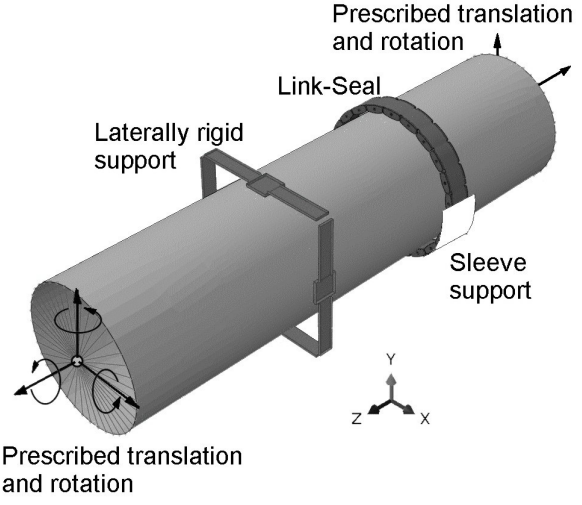

Fig. 10. *Model of the pipe at wall penetration*

2.2 Model Loads

The internal surface of the pipe is loaded with a pressure of 240 kPa.

Table 1. *Critical displacement and rotation combinations*

Load. comb. / Ref. Node	Translation [mm]			Rotation [°]		
	Δx	Δy	Δz	φ_x	φ_y	φ_z
*u*1/1	–8.22	–4.49	–12.51	–0.15	0.23	0.08
*u*1/2	–1.33	–0.53	–12.41	–0.04	0.09	0.06
*u*2/1	–0.77	15.9	23.62	0.52	0.01	0.07
*u*2/2	–0.3	1.58	23.41	0.17	0.01	0.05
*u*3/1	–9.32	–14.53	–1.42	–0.56	0.32	0.09
*u*3/2	–0.22	0.47	–1.34	–0.16	0.11	0.07
*u*4/1	10.12	22.88	2.6	0.73	–0.35	–0.14
*u*4/2	0.27	1.79	2.48	0.25	–0.11	–0.10
*u*5/1	–14.6	4.44	5.41	0.20	0.44	0.26
*u*5/2	–1.68	–0.47	5.26	0.05	0.16	0.20
*u*6/1	23.41	20.77	0.74	0.57	–0.73	–0.34
*u*6/2	2.38	3.33	0.69	0.23	–0.26	–0.26

The prescribed displacements and rotations of the pipe end reference nodes are the pipe's most important loading. From the global beam model [1], with which the earthquake analysis of the whole pipeline was performed, extreme seismic displacements and rotations of two nodes corresponding to two reference nodes were retrieved and incorporated into the pipe shell model as prescribed spatial translations and rotations. Six displacement and rotation combinations, denoted as *u*1 through *u*6, were identified in a beam model as critical combinations; see Table 1.

In the finite element simulation of the pipe shell, the strain and stress state in the pipe from one loading combination was transmitted in the next loading combination. Thus, the plastic strain and possible damage to the pipe wall were accumulated. The analysis was dynamic; thus, one loading combination was smoothly transferred into another. The total duration of one loading combination was 0.1 s, which roughly resembles the time between individual shocks during an earthquake.

3 RESULTS

Selected results from a database of finite element analysis results are displayed. Fig. 11 shows a pipe with a deformed shape (exaggerated by a factor of 10). In that figure, all pipe deformation modes except pipe ovalization are clearly seen. The most severe appears to be the indentation at the Link-Seal where a series of smaller axial dents form one large circumferential dent. Due to the displacement magnification factor 10, this dent seems non-smooth (with kinks). When the deformed shape of the pipe was inspected at magnification factor 1 (no magnification), smooth change of curvature at dents locations were observed. Therefore, the dents are categorized as plain dents. The deepest dent is indented at h = 12 mm, which represents 12/610×100 % = 2 % of the pipe diameter. In ref. [3], where results of many experiments are interpreted, plain dents up to 10 % are considered acceptable. In [6], dents of the same h/t ratio but for smaller D/t ratio are anticipated to preserve 80 % of the dent-free pipe bending moment. Therefore, it seems that the dents in Fig. 11 do not represent a pipe bursting peril.

Fig. 12 shows the equivalent plastic strain at the end of the simulation, i.e., the plastic strain accumulated after all six displacement and rotation combinations were accomplished. The extreme plastic strain value is 0.127, which represents 38 % of the plastic strain at break (Fig. 1) or, in other words, 75 % of the extreme plastic strain during the flattening test

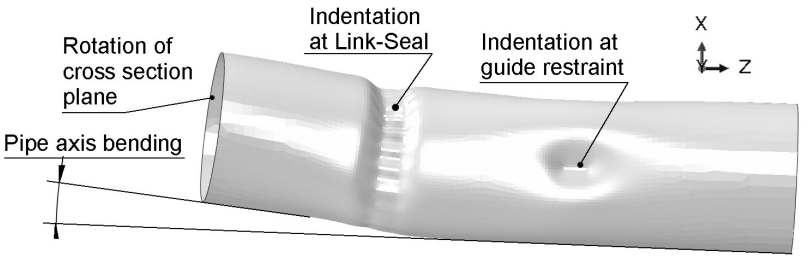

Fig. 11. *Top view of the pipe at the end of the simulation (displacement magnification factor 10)*

(Fig. 2c). It should be noted that high plastic strain, say, greater than 0.05, is localized around several Link-Seal pressure plates. The white-coloured regions represent no plastic strain.

Because the stress cannot accumulate like the plastic strain, the stress states from all displacement combinations in Table 1 need to be checked for extreme stress. The extreme von Mises equivalent stresses found in the pipe are listed in Table 2.

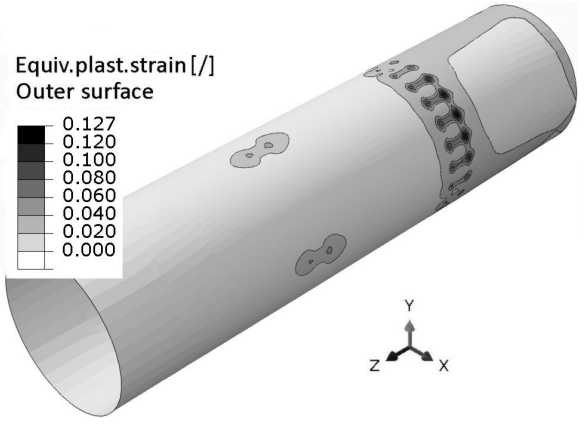

Fig. 12. *Equivalent plastic strain at the end of the simulation*

Table 2. *Penetration pipe, total stress for all displacement combinations*

Loading comb.	von Mises stress at pipe wall surface [MPa]		
	Inner	Middle	Outer
u1	324	240	342
u2	355	376	441
u3	360	357	494
u4	490	453	576
u5	443	409	571
u6	549	489	612

Note: The pipe's middle surface refers to the imaginary surface at the half thickness of the pipe wall.

Because the highest stresses were found in the last displacement combination, the stress state and stress-qualification procedure will be presented in detail for that combination only.

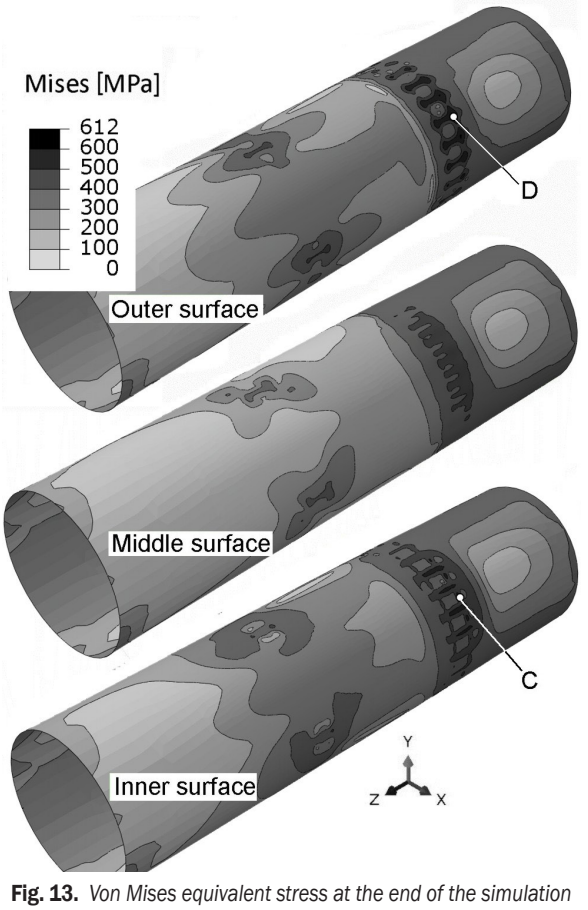

Fig. 13. *Von Mises equivalent stress at the end of the simulation*

Fig. 13 provides the von Mises equivalent stress at the end of the simulation. The three pictures represent the stress field at the outer, middle and inner shell surface.

The most stressed parts of the pipe are locations at which the Link-Seal pressure plates contact the pipe

wall and cause local bending of the pipe wall. Lateral reaction forces produce local contact pressure (Fig. 14) and local shear stress (not shown) on the pipe wall.

The stresses obtained from the finite element simulation are total stresses; therefore, the total stresses are decomposed into bending P_b, local membrane P_L and peak stress F. Fig. 15 shows components of the total stress tensor acting on the C-D stress path through the pipe wall's thickness. The zero-wall thickness coordinate corresponds to the inside of the wall (point C in Fig. 13). As in Fig. 3, inelastic bending is the prevailing loading in the path.

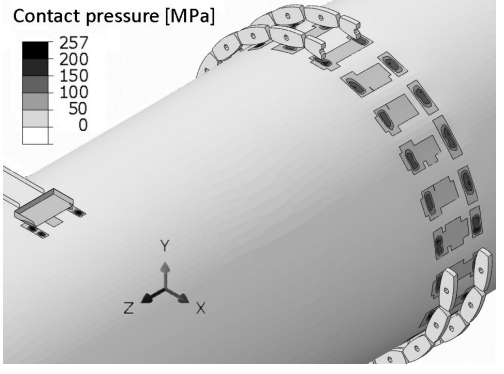

Fig. 14. *Contact pressure at the end of the simulation*

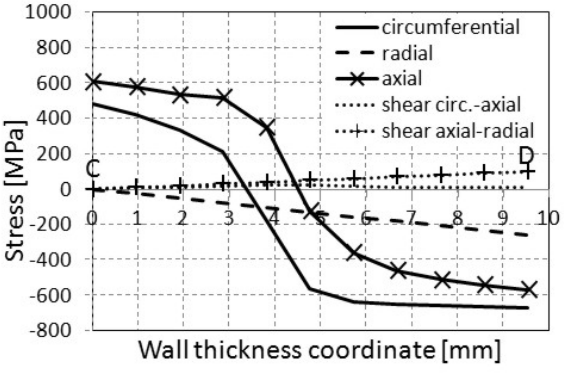

Fig. 15. *Stress tensor components at the most critical stress path C-D at the end of the simulation*

The same stress linearization procedure as described in Section 1.2.3 yields the following stress intensities, expressed in the form of the von Mises equivalent stress intensities: equivalent stress from membrane stress tensor P_L = 232 MPa and equivalent stress from the sum of the membrane and bending stress tensors at point C (inner surface of the pipe), $(P_m + P_b)_C$ = 695 MPa, and at point D (outer surface of the pipe), $(P_m + P_b)_D$ = 813 MPa.

Finally, in Table 3, the analysis results are presented in a short form. All the stress and strain criteria are fulfilled; thus, the pipeline penetration qualifies for augmented (beyond-the-design) seismic loading.

4 DISCUSSION

Qualification of the most stressed part of the pipeline, i.e., the pipe penetration through the concrete wall, is based on the ASME rules **[7]** and common engineering reasoning.

The most discussible part of the methodology, presented in the paper, is the stress linearization procedure, with which the total stress is decomposed into those of the primary membrane P_m, primary local P_L, primary bending P_b and peak stress F. In the ASME Code, it is assumed that the linearization procedure will be performed on stresses obtained on pure elastic material. However, in ASME Sect. III, Appendix F **[7]**, which deals with extreme loading conditions and allows for elastic-plastic material response, the stresses must be decomposed into P_m, P_L and P_b. However, no explicit rule is given in the code about how to linearize stresses in case of elastic-plastic material response **[11]**. In this regard, the same physical equivalence principle regardless of the evidenced degree of non-linearity in the actual stress distribution is adopted in this work. The author is fully aware that by increasing the degree of non-linearity, uncommon results might be obtained from

Table 3. *Penetration pipe, stress intensities*

Stress category	Allowable [MPa]	Calculated [MPa]	Comment
Primary membrane P_m	466	< 350	Remote from supports
Primary bending P_b			
Local membrane P_L	466	232	Stress path C-D
Primary local plus primary bending $P_L + P_b$	912	813	Point D
		695	Point C
Total stress	635	612	Non-ASME requirement
Equivalent plastic strain [/]	0.17	0.127	Non-ASME requirement

thus specified stress linearization. Nevertheless, in the flattening test simulation (Section 1.2.3) and in the penetration pipe simulation (Section 3), this stress linearization procedure was strictly followed regardless of the results obtained in this way. The adopted approach is justified by the fact that the same stress linearization procedure was used for both simulations, i.e., in the assessment of the limiting state for the flattening test and in checking whether the pipe penetration stress state reached the limits. Thus, the same methodological inconsistencies (if any) are cancelled out.

5 CONCLUSIONS

Piping systems are usually designed using the simplest approach permitted by codes and standards. This leaves quite large margins in terms of real sustainability of piping systems. The paper shows how these margins can be exploited to uprate mechanical loads acting on the pipeline without changing any hardware (supports, piping sections, piping layout) while still obeying the codes. Particular analysis methods were used to obtain this goal.

6 ACKNOWLEDGEMENTS

The author acknowledges financial support from the Slovenian Research Agency (research core funding No. P2-0263) and the Nuklearna Elektrarna Krško. Also, the author wishes to express thanks to NEK personnel for their support and collaboration.

All analyses were performed in the Laboratory for Numerical Modelling and Simulation of Faculty for Mechanical Engineering, University of Ljubljana.

7 REFERENCES

[1] Celarec, D., Koc, P., Jalovec, R., Kodrič, M., Planinc, R., Daniels, E. (2014). *Assesment of capacity of the NEK to resist permanent ground deformations due to potential surface faulting*. Report number: NEK ESD-TR-10/13, Revision 2. NEK and Worley parsons, Krško (NEK proprietary document).

[2] Liu, J.H., Francis, A. (2004). Theoretical analysis of local indentation on pressured pipes. *International Journal of Pressure Vessels and Piping*, vol. 81, no. 12, p. 931-939, **DOI:10.1016/j.ijpvp.2004.05.007**.

[3] Cosham, A., Hopkins, P., (2003). The effect of dents in pipelines – Guidance in the pipeline defect assessment manual. *ICPVT-10 Conference Proceedings*, p. 127-139.

[4] Pinheiro, B., Pasqualino, I., Cunha, S. (2014). Fatigue life assessment of damaged pipelines under cyclic internal pressure: Pipelines with longitudinal and transverse plain dents. *International Journal of Fatigue*, vol. 68, p. 38-47, **DOI:10.1016/j.ijfatigue.2014.06.003**.

[5] Garbatov, Y., Guedes Soares, C. (2017). Fatigue reliability of dented pipeline based on limited experimental data. *International Journal of Pressure Vessels and Piping*, vol. 155, p. 15-26, **DOI:10.1016/j.ijpvp.2017.07.001**.

[6] Cai, J., Jiang, X., Lodewijks, G., Pei. Z., Wu W. (2018). Residual ultimate strength of damaged seamless metallic pipelines with combined dent and metal loss. *Marine Structures*, vol. 61, p. 188-201, **DOI:10.1016/j.marstruc.2018.05.006**.

[7] ASME Boiler and Pressure Vessel Code (1972). *Section III, Subsection ND-Class 3 Components and Appendix F-Rules for Evaluation of Service Loading with Level D Limits*. American Society of Mechanical Engineers. New York.

[8] ASME Boiler and Pressure Vessel Code (1972). *Section II, Part A-Ferrous Material Specifications and Part D-Properties.* American Society of Mechanical Engineers. New York.

[9] Dassault Systemes, ABAQUS, Ver. 6.11, from *https://www.3ds.com/products-services/simulia/products/abaqus/*, accessed on 2018-11-09.

[10] GPT Industries, Wall Penetration Seals, Link-Seal from *https://www.gptindustries.com/en/products/link-seal*, accessed on 2018-11-09.

[11] Faidy, C. (Coordinator) (2017). *Non-Linear Analysis Design Rules*. World Nuclear Association, London.

[12] Venter, R.D., Sinclair, A.N., McCammond, D., (1989). *Crack Propagation in Tough Ductile Materials (Phase II)*. Atomic Energy Control Board, Otawa.

Vsebina

Strojniški vestnik - Journal of Mechanical Engineering
letnik 65, (2019), številka 3
Ljubljana, marec 2019
ISSN 0039-2480

Izhaja mesečno

Razširjeni povzetki (extended abstracts)

Strojniški vestnik - Journal of Mechanical Engineering 65(2019)3, SI 19

Prejeto v recenzijo: 2018-11-14
Prejeto popravljeno: 2019-01-23
Odobreno za objavo: 2019-02-22

Vpliv onesnaženega fluida na delovanje hidravličnega potnega ventila

Velibor Karanović[1,*] – Mitar Jocanović[1] – Sebastian Baloš[1] – Darko Knežević[2] – Ivan Mačužić[3]

[1] Univerza v Novem Sadu, Tehniška fakulteta, Srbija
[2] Univerza v Banja Luki, Fakulteta za strojništvo, Bosna in Hercegovina
[3] Univerza v Kragujevcu, Fakulteta za strojništvo, Srbija

Cilj predstavljene študije je raziskava vpliva delcev trdne nesnage v hidravličnem olju na delovanje potnega ventila.

Onesnaževala v hidravlični tekočini (trdni delci, voda in zrak) lahko neposredno ali posredno vplivajo na vedenje sistema. Trdni delci so najbolj uničevalni in lahko povzročijo mnoge težave, še zlasti v sodobnih hidravličnih sistemih z mikronskimi tolerancami. Interakcije med delci, fluidom, komponentami in hidravličnim sistemom so kompleksne in jih je težko napovedati.

Za boljše razumevanje teh pojavov se izvajajo eksperimenti za določanje stopnje obrabe v odvisnosti od različnih ravni onesnaženosti fluida. Opravljeni so bili eksperimenti z meritvijo vpliva čistoče delovnega medija na stopnjo obrabe kontaktnih površin in na druge motnje v delovanju potnega ventila (puščanje, tlačni padec) po določenem številu delovnih ciklov. Uporabljeni so bili trije novi smerni ventili istega proizvajalca z enakimi delovnimi karakteristikami. Zgrajen je bil eksperimentalni sistem s temi delovnimi parametri: $p = 150$ bar, $Q = 9{,}5$ l/min, $T = 45$ °C. Vsi trije ventili so opravili do $n = 10^6$ delovnih ciklov pri različnih stopnjah čistoče olja. Vodeni in nadzorovani so bili parametri, kot so tlak, pretok, temperatura in čistoča hidravličnega olja. Nadzorovana je bila reža med kontaktnimi površinami na izvrtinah in krmilnem batu v telesu ventila, kakor tudi spremembe puščanja fluida skozi reže, spremembe mase bata in telesa ventila zaradi obrabe, in tlačni padec med pretokom fluida skozi odprt ventil.

Rezultati eksperimentov so potrdili pričakovane razlike v stopnji obrabe. Primerjava rezultatov eksperimentov št. 1 in št. 2 (v eksperimentu št. 2 je bilo uporabljeno čistejše olje) je pokazala, da se je stopnja obrabe zmanjšala za faktor 2,5. Primerjava rezultatov eksperimentov št. 1 in št. 3 je pokazala trikratno zmanjšanje stopnje obrabe. Razmerje med zadnjo in prvo izmerjeno vrednostjo puščanja skozi reže pri prvem eksperimentu je bilo 1,97, pri drugem eksperimentu 1,83 in pri tretjem eksperimentu 1,79. Za analizo eksperimentalnih podatkov sta bila uporabljena metoda najmanjših kvadratov in programski paket MATLAB. Izpeljan je bil poseben matematični model za stopnjo obrabe in puščanje skozi reže ventila pri različnih stopnjah onesnaženosti olja. Z meritvami tlačnega padca je bilo ugotovljeno, da stopnja čistoče olja vpliva na tlačni padec in na raztros izmerjenih vrednosti tlaka. Zaradi povečanja tlačnega padca nastane več toplote, celotna učinkovitost sistema pa se zmanjša.

Teoretično izračunane vrednosti puščanja fluida skozi reže v statičnih pogojih se ne ujemajo z eksperimentalno izmerjenimi vrednostmi. Eksperimentalno določene vrednosti puščanja in velikosti rež rastejo znatno hitreje od teoretičnih. Rezultati raziskave bodo prispevali k boljšemu razumevanju vpliva čistoče delovnega medija na napake in motnje komponent hidravličnega sistema.

Ključne besede: hidravlični sistemi, nadzor stanja, tribologija, obraba, čistoča fluida, trdni delci

*Naslov avtorja za dopisovanje: Univerza v Novem Sadu, Tehniška fakulteta, Trg Dositeja Obradovica 6, 21000 Novi Sad, Srbija, velja_82@uns.ac.rs

Strojniški vestnik - Journal of Mechanical Engineering 65(2019)3, SI 20

Prejeto v recenzijo: 2018-10-18
Prejeto popravljeno: 2019-01-28
Odobreno za objavo: 2019-02-27

Načrtovanje gibanja visokoavtomatiziranih cestnih vozil po hibridnem pristopu z nelinearno optimizacijo in umetnimi nevronskimi mrežami

Ferenc Hegedűs[1] – Tamás Bécsi[2] – Szilárd Aradi[2] – Péter Gáspár[3]

[1] Robert Bosch, Madžarska

[2] Univerza za tehniko in ekonomijo v Budimpešti, Oddelek za upravljanje transportnih sistemov in vozil, Madžarska

[3] Madžarska akademija znanosti, Raziskovalni institut za računalništvo in avtomatizacijo, Madžarska

V zadnjem desetletju je bilo zaradi vse večjega zanimanja za avtomatizacijo cestnega transporta razvitih mnogo algoritmov za načrtovanje gibanja cestnih vozil. Za dinamično izvedljivost načrtovanih trajektorij je treba upoštevati anholonomno dinamiko kolesnih vozil. Načrtovalniki trajektorij na osnovi nelinearne optimizacije dokazano izpolnjujejo to zahtevo, vendar na račun povečanja potrebnih računskih kapacitet, to pa ogroža uporabnost teh metod za realnočasovne aplikacije.

Cilj predstavljene raziskave je zasnovati metodo za načrtovanje gibanja avtonomnih cestnih vozil s podobnimi zmogljivostmi na področju dinamike kot pri načrtovalnikih na osnovi nelinearne optimizacije, ki pa ne bo obremenjena z računsko zahtevnostjo sprotne optimizacije.

Najprej je predstavljen načrtovalnik trajektorij na osnovi nelinearne optimizacije, ki zahtevane dinamične lastnosti zagotavlja z napovedovanjem gibanja vozila na podlagi točnega modela dinamike cestnega vozila. V predstavljenem pristopu so bile uporabljene tehnike nadzorovanega učenja umetne nevronske mreže (ANN) za pridobitev enakih izhodov kot pri predstavljenem načrtovalniku na osnovi nelinearne optimizacije. Ker se podatki za učenje ustvarijo v ločenem koraku, odpade problem računske zahtevnosti optimizacijskih metod. Naučena ANN se nato uporabi na tak način, da je vedno zagotovljena veljavnost njenih izhodov. Po eni strani lahko deluje kot generator začetnih vrednosti blizu optimalnim za optimizacijski proces, po drugi strani pa lahko v hibridnem pristopu tudi popolnoma nadomesti optimizacijsko zanko v kombinaciji s plastjo dinamike vozila originalnega načrtovalnika.

Zmogljivost pristopov na osnovi ANN je bila ovrednotena s simulacijami ob upoštevanju časa izvajanja, odstopanj stanj vozila in kriterija optimalnosti gibanja. Rezultati kažejo, da oba pristopa znatno skrajšata čas izvajanja, obenem pa se ohrani izvedljivost načrta gibanja. Drugi pristop je primeren tudi za realnočasovne aplikacije in trenutno potekajo priprave z dodatnimi simulacijami v priznanem paketu za dinamiko vozil CarMaker za uporabo v testnem vozilu.

Predstavljeno delo ima seveda tudi določene omejitve. Čeprav so se algoritmi dobro izkazali v simulacijah, jih bo treba preveriti še v realnih obratovalnih pogojih. V proces učenja ANN tudi še ni bilo vključeno izogibanje oviram in to je ena od možnih smeri za nadaljnje delo.

Uporaba ANN za naloge načrtovanja gibanja cestnih vozil je v literaturi zelo redka, kljub odličnim rezultatom ANN na področju prilagajanja in generalizacije. Novost predstavljene tehnike je tako v uporabi umetnih nevronskih mrež, ki so možna zamenjava za računsko zahtevne procese sprotne optimizacije in primerne za realnočasovne aplikacije, kakor tudi v nadzoru ANN s klasičnimi pristopi kot osnovi za validacijo.

Ključne besede: avtomatizirana vožnja, načrtovanje gibanja, načrtovanje trajektorij, vodenje vozila, nelinearna optimizacija, umetne nevronske mreže

*Naslov avtorja za dopisovanje: Robert Bosch, 2 Stoczek cesta, 1111 Budimpešta, Madžarska, hegedus.ferenc@mail.bme.hu

Strojniški vestnik - Journal of Mechanical Engineering 65(2019)3, SI 21

Prejeto v recenzijo: 2018-10-11
Prejeto popravljeno: 2019-01-23
Odobreno za objavo: 2019-01-28

Aktivni strukturni derivator v fazi kristalizacije zasnove konstrukcije vozil L7e

Roman Pawel Jedrzejczyk* – Michael Sigmar Alb
Raziskovalno središče Virtual Vehicle, Avstrija

Inženirji so zadnja leta začeli uporabljati topološko optimizacijo (TO) za pripravo prvih predlogov zasnov novih konstrukcij. Konstruktorji morajo bionske oblike kot rezultate TO pretvoriti v tehnično izvedljive geometrije na osnovi razpoložljivih tipov konstrukcij surovih karoserij (BST), ki bodo učinkovite in lahke. Pomanjkanje standardiziranih metodologij sili konstruktorje v subjektivno pretvorbo bionskih oblik TO, posledica tega pa so neučinkoviti in neustrezni predlogi zasnov. Upravljanje konstrukcijskega procesa je še toliko težje zaradi vrste ločenih geometrijskih prehodov, ki so na voljo pri transformaciji rezultatov TO v enega od izbranih BST. Izbira neustreznega BST je lahko tudi draga napaka. Morebitni neobstoječi deli v novi konstrukciji, ki ni bila ustrezno pretvorjena iz rezultatov TO v geometrijski model, ključno vplivajo na nosilnost konstrukcije. Da bi izboljšali na novo zasnovane konstrukcije, morajo inženirji zato uporabiti dodatne korake za optimizacijo konstrukcij, s čimer se podaljša skupni čas razvoja. Avtomobilski proizvajalci so znatno povečali število izpeljank modelov v svoji ponudbi, da bi odgovorili na individualne potrebe in zahteve kupcev novih vozil. Konstruktorji morajo z dodatnimi analizami (npr. z identifikacijo sistemov) ovrednotiti, ali zasnove izpeljank ustrezajo novim specifikacijam. 18-mesečni razvojni cikli pa končno tudi omejujejo število študij izvedljivih zasnov novih konstrukcij. Uvajanje potencialnih ukrepov za zmanjšanje teže pri novih zasnovah, kot so drugačni tipi BST in novi materiali, vključno s sendvič materiali, je v poznejših fazah razvojnega procesa povezano z visokimi stroški in lahko vpliva na končno ceno novih vozil. Avtorji so zato podali predlog aktivnega derivatorja konstrukcij (ASD) kot razširitve obstoječega integrativnega procesa konstruiranja na osnovi CAE (ICDDP). Pojem »derivator« je bil prevzet iz matematike, kjer izpopolnjuje in v določeni meri poenostavlja teorijo homotopične algebre. ASD omogoča gladko pretvorbo rezultatov TO in praktično vrednotenje izbranih tipov surovih karoserij, kot so cevni palični okvir, hibridna konstrukcija, samonosna karoserija in monokok. ASD istočasno uporablja optimizacijo velikosti in prosto optimizacijo velikosti s posebnimi kriteriji znotraj simulacijskega modela, ki vključuje osnovno tehnično geometrijo (nosilci in plošče), za ustvarjanje konceptov zasnov različnih BST glede na dane zahteve. ASD pri različnih konfiguracijah konstrukcij omogoča konstruktorjem, da ocenijo kombinacije različnih materialov, kot so izotropni in ortotropni materiali (npr. jeklo, aluminij, kompoziti in sendvič materiali), loči med izbranimi poljubnimi in definiranimi vrstami prerezov nosilcev (npr. škatlasti, palice), ki jih je skupaj s ploščatimi geometrijami mogoče uporabiti v analizi razpoložljivih BST. ASD upošteva vrsto dejanskih obremenitev in omogoča konstruktorjem izbiro primernih nosilcev za dane natezno-tlačne, upogibne in torzijske obremenitve, upošteva vpliv geometrije plošč (lupin) na nosilnost nove konstrukcije, upošteva obremenitve in obremenitvene primere, ki vplivajo na togost novih konstrukcij in zahtevajo izboljšanje zasnove. ASD vse to omogoča v enem modelu po MKE. V članku so predstavljeni rezultati analize ASD za novo konstrukcijo električnega vozila eQuad oz. predlog nove zasnove konstrukcije električnega vozila L7e.

Ključne besede: bionska geometrija, surova karoserija, konstrukcijski proces, MKE, prosta optimizacija velikosti, ICDDP, topološka optimizacija, optimizacija velikosti, zasnova konstrukcije vozila

*Naslov avtorja za dopisovanje: Virtual Vehicle Research Center, Inffeldgasse 21a, 8010 Graz, Austria, RomanPawel.Jedrzejczyk@v2c2.at

Strojniški vestnik - Journal of Mechanical Engineering 65(2019)3, SI 22

Prejeto v recenzijo: 2018-09-03
Prejeto popravljeno: 2019-02-15
Odobreno za objavo: 2019-02-21

Fizikalno-mehanska karakterizacija naravnih vlaken palme (*Mauritia flexuosa*) in kompozita z bioepoksi smolo

William Javier Mora Espinosa* – Bladimir Azdrubal Ramón Valencia – Gonzalo G. Moreno Contreras
Univerza v Pamploni, Kolumbija

Namen predstavljene raziskave je bil določitev mehanskih, toplotnih in morfoloških lastnosti vlaken palme Mauritia flexuosa ter kompozita iz bioepoksi smole, ojačene s temi vlakni. Cilj je popularizacija vlaken, pridobljenih iz te palme, ki je razširjena po ravninah v kolumbijskem porečju Amazonke. Ta vlakna danes uporabljajo samo rokodelci in zato se raziskujejo nove možnosti za boljše izkoriščanje tega naravnega vira.

Uporaba naravnih vlaken za ojačitev kompozitnih materialov raste na svetovni ravni zaradi prizadevanj k zmanjševanju vplivov na okolje in zdravstvenih težav, ki jih povzroča ravnanje s konvencionalnimi ojačitvenimi materiali, kot so steklena vlakna, ogljikova vlakna in druga sintetična vlakna. Novi in prijaznejši materiali naj bi imeli lastnosti, ki so primerljive z lastnostmi obstoječih materialov ali celo boljše. Ojačitvene materiale in kompozite običajno vrednotimo po mehanskih, toplotnih in morfoloških lastnostih, kot so natezna trdnost, elastični modul, deformacije, odstotni delež vlage, temperaturno območje skladiščenja, notranja struktura (velikost odprtin, debelina celičnih sten, simetrija, variabilnost količine in velikosti) in adhezija.

Prvi korak je bil pridobitev vlaken iz primarnih virov in določitev njihovih lastnosti za primerjavo z vlakni, ki se danes že uporabljajo v industrijski proizvodnji kompozitov (juta, lan, konoplja ali kenaf). Na ta način je mogoče opredeliti primernost vlakna za uporabo v funkciji ojačitvenega materiala in določiti ustrezno matrico (termoplastična ali duroplastična) za oblikovanje biokompozitnega materiala. V tem primeru je bila uporabljena duroplastična matrica oz. bioepoksi smola, pridobljena iz kmetijskih odpadkov in ojačena z več plastmi 45° tkanine, ročno izdelane iz vlaken palme Mauritia flexuosa. Za enakomerno impregniranje s smolo brez mehurčkov je bil uporabljen vakuumski postopek VARTM. Tako ustvarjeni laminat je bil nato okarakteriziran z nateznimi in upogibnimi preizkusi po standardu ASTM, stopnja adhezije vlaken in matrice pa je bila ocenjena z vrstičnim elektronskim mikroskopom. Mehanske lastnosti novega materiala so bile primerjane z drugimi kompoziti, ojačenimi z naravnimi vlakni, in izkazalo se je, da ima novi material odlične upogibne lastnosti.

Rezultati omogočajo opredelitev možnih področij uporabe materiala, mikroskopski posnetki pa so pokazali slabo adhezijo zaradi uporabe neobdelanega ojačitvenega materiala v naravnem stanju. Na ta način je mogoče identificirati tiste spremenljivke, ki imajo največji vpliv na mehanske lastnosti (površinska obdelava, predhodno sušenje, geometrija tkanine, smer ojačitve, količine, itd.) in jih uravnavati za boljše rezultate. Ugotovljena je bila majhna natezna trdnost (25 MPa) in visoka upogibna trdnost (253,7 MPa). Te vrednosti so tudi brez predhodne obdelave vlaken podobne in v nekaterih primerih celo boljše kot pri drugih kompozitnih materialih. Rezultati predstavljene raziskave vlaken in biokompozitnega materiala odpirajo nove priložnosti za nadaljnje delo na področju fizikalno-kemičnih obdelav ter novih orientacij in vrst ojačitvenih rastlinskih tkiv, s katerimi bo mogoče doseči boljšo adhezijo vlaken in matrice in tako izboljšati mehanske lastnosti materiala.

Prispevek tega dela na področju kompozitnih materialov je v popularizaciji novih naravnih vlaken, ki imajo potencial za uporabo v funkciji ojačitve pri biokompozitih. Ti materiali so prijaznejši do okolja in ravnanje z njimi je manj tvegano, kot zamenjava za konvencionalne materiale pa imajo tudi manjši vpliv ob koncu svojega življenjskega cikla. Pridelava in obdelava palme Mauritia flexuosa bi v prihodnje lahko postala tudi vir prihodkov za prebivalstvo področij, kjer uspeva ta rastlina.

Ključne besede: naravna vlakna, ojačitev, matrica, biokompozit, mehanske lastnosti, toplotna stabilnost, morfologija, adhezija

*Naslov avtorja za dopisovanje: Univerza v Pamploni, Km 1 Highway to Bucaramanga, Pamplona, Kolumbia, william.mora2@unipamplona.edu.co

Strojniški vestnik - Journal of Mechanical Engineering 65(2019)3, SI 23

Prejeto v recenzijo: 2018-07-16
Prejeto popravljeno: 2019-02-27
Odobreno za objavo: 2019-03-06

Zahtevnejša mehanska analiza preboja cevovoda v stavbo

Pino Koc*
Univerza v Ljubljani, Fakulteta za matematiko in fiziko, Slovenija

V inženirski praksi se ne tako redko pojavi problem povečanja obratovalnih obremenitev obstoječega cevovodnega sistema. S tem povečanjem se povečuje nevarnost porušitve cevovoda in prav lahko se zgodi, da z računskimi metodami, ki so bile uporabljene v originalnem izračunu, ne moremo več dokazati ustreznosti obstoječega cevovoda za nove, povečane obremenitve. Zaradi tega bi bila potrebna nadgradnja cevovoda v obliki dodajanja podpor, ojačevanja ali zamenjave delov cevovoda, itd. V nekaterih primerih pa se je možno fizičnemu spreminjanju cevovoda izogniti z naprednimi računskimi metodami, s katerimi je moč dokazati ustreznost cevovoda na povečane obremenitve.

V prispevku je prikazan primer analiz pri povečanju potresnih obremenitev na zakopan jeklen cevovod v Nuklearni elektrarni Krško. Najbolj kritično mesto je vstop cevovoda (preboj) v betonsko stavbo, saj na tem mestu pride pri potresu do velikih razlik v premikih stavbe in okoliške zemljine, v kateri je zakopan cevovod. To povzroči velike lokalne deformacije tankostenskega cevovoda (D/t = 64), ki se izkazujejo v obliki ovalizacije prereza cevovoda ter v lokalnem vbočenju stene cevovoda. Tovrstni načini deformacij in posledično tudi pripadajoča napetostna stanja še niso uvrščeni v izračune v ASME B&PV standardu, ki je obvezen standard v NEK-u. Namen naše raziskave je ugotoviti ali je možno na kakršen koli računski način in ob upoštevanju smernic in zahtev iz ASME standarda, dokazati ustreznost analiziranega cevovoda na mestu preboja skozi betonski zid tudi v primeru povečanih potresnih obremenitev.

Mehanske analize cevovoda in penetracije so izdelane z metodo končnih elementov. Najprej je bil izdelan model cevovoda (globalni) iz linijskih končnih elementov, ki pa ne omogočajo analizo vbočenja stene. Zato je izdelan še lokalni model dela cevovoda na mestu preboja, pri katerem z lupinskimi končnimi elementi zasledujemo vse načine deformiranja stene cevovoda. Globalni in lokalni model sta medsebojno povezana, saj premiki točk osi cevovoda na mestu preboja, dobljeni z globalnim modelom, služijo kot vhodni podatek za lokalni model. Obratno pa z lokalnim modelom izračunane lateralne togosti cevovoda na mestih podprtja in tesnenja cevovoda služijo kot vhodni podatek v globalnem modelu.

Vbočenje stene nastane na preboju na mestu tesnila med betonsko steno in cevovodom. Tesnilo omogoča omejene premike cevovoda glede na steno stavbe, ni pa sposobno prevzeti vsa relativna gibanja cevovoda pri velikem potresu. Tesnilo vsebuje poleg polimernih tesnilnih elementov še jeklene dele, ki v primeru večjih premikov cevovoda nasedejo na steno cevovoda in v steni povzročijo niz vboklin. Te vbokline pomenijo nevarnost za nastanek nedopustnih razpok v cevovodu. Kot podpora pri ugotavljanju nevarnosti niza vboklin nam služijo rezultati študij drugih avtorjev. Naš primer je poseben v tem, da so vdrtine v nizu in ne ena sama, kot v omenjenih študijah.

Formalno dokazovanje ustreznosti cevovoda na povečane obremenitve je izvedeno s kontrolo napetostnega stanja. Težava je v tem, da izračunano napetostno stanje v steni cevi na mestu lokalnega vbočenja presega dopustno stanje napetosti iz ASME standarda. Kot rešitev smo uporabili teste sploščevanja obročev, izrezanih iz cevi (flattening test). V teh testih je bil izrezan po en preizkušanec-obroč iz vsake cevi, ki je bila namenjena vgradnji v cevovod. Preizkušanec je bil med dvema togima ploščama sploščen do zahtevane razdalje; pri tem noben del obroča ni smel kazati znake porušitve, t.j. razpoke. Izvedli smo numerično simulacijo testa sploščevanja in ugotovili napetostno stanje v obroču, ki je v nadaljevanju analiz služilo kot maksimalno dopustno napetostno stanje. Ker je napetostno stanje na mestu lokalnega vbočenja bolj blago od stanja pri testu sploščevanja, sklepamo, da do nastanka razpok pri lokalnem vbočenju ne bo prišlo in s tem kvalificiramo cevovod za povečane potresne obremenitve.

Praktična vrednost prispevka je v prikazu rešitve problema, kjer klasične analize odpovejo in je z nekoliko drugačnimi analizami moč dokazati ustreznost cevovoda brez fizičnega posega vanj.

Ključne besede: cev, preboj, vboklina, potres, ASME B&PV, NEK

*Naslov avtorja za dopisovanje: Univerza v Ljubljani, Fakulteta za matematiko in fiziko, Slovenija, pino.koc@fmf.uni-lj.si

Information for Authors

All manuscripts must be in English. Pages should be numbered sequentially. The manuscript should be composed in accordance with the Article Template given above. The maximum length of contributions is 10 pages. Longer contributions will only be accepted if authors provide juastification in a cover letter. For full instructions see the Information for Authors section on the journal's website: http://en.sv-jme.eu .

SUBMISSION:

Submission to SV-JME is made with the implicit understanding that neither the manuscript nor the essence of its content has been published previously either in whole or in part and that it is not being considered for publication elsewhere. All the listed authors should have agreed on the content and the corresponding (submitting) author is responsible for having ensured that this agreement has been reached. The acceptance of an article is based entirely on its scientific merit, as judged by peer review. Scientific articles comprising simulations only will not be accepted for publication; simulations must be accompanied by experimental results carried out to confirm or deny the accuracy of the simulation. Every manuscript submitted to the SV-JME undergoes a peer-review process.

The authors are kindly invited to submit the paper through our web site: http://ojs.sv-jme.eu. The Author is able to track the submission through the editorial process - as well as participate in the copyediting and proofreading of submissions accepted for publication - by logging in, and using the username and password provided.

SUBMISSION CONTENT:

The typical submission material consists of:

- A **manuscript** (A PDF file, with title, all authors with affiliations, abstract, keywords, highlights, inserted figures and tables and references),
- Supplementary files:
  - a **manuscript** in a WORD file format
  - a **cover letter** (please see instructions for composing the cover letter)
  - a ZIP file containing **figures** in high resolution in one of the graphical formats (please see instructions for preparing the figure files)
  - possible **appendicies** (optional), cover materials, video materials, etc.

Incomplete or improperly prepared submissions will be rejected with explanatory comments provided. In this case we will kindly ask the authors to carefully read the Information for Authors and to resubmit their manuscripts taking into consideration our comments.

COVER LETTER INSTRUCTIONS:

Please add a **cover letter** stating the following information about the submitted paper:

1. Paper **title**, list of **authors** and their **affiliations**.
2. **Type of paper**: original scientific paper (1.01), review scientific paper (1.02) or short scientific paper (1.03).
3. A **declaration** that neither the manuscript nor the essence of its content has been published in whole or in part previously and that it is not being considered for publication elsewhere.
4. State the **value of the paper** or its practical, theoretical and scientific implications. What is new in the paper with respect to the state-of-the-art in the published papers? Do not repeat the content of your abstract for this purpose.
5. We kindly ask you to suggest at least two **reviewers** for your paper and give us their names, their full affiliation and contact information, and their scientific research interest. The suggested reviewers should have at least two relevant references (with an impact factor) to the scientific field concerned; they should not be from the same country as the authors and should have no close connection with the authors.

FORMAT OF THE MANUSCRIPT:

The manuscript should be composed in accordance with the Article Template. The manuscript should be written in the following format:

- A **Title** that adequately describes the content of the manuscript.
- A list of **Authors** and their **affiliations**.
- An **Abstract** that should not exceed 250 words. The Abstract should state the principal objectives and the scope of the investigation, as well as the methodology employed. It should summarize the results and state the principal conclusions.
- 4 to 6 significant **key words** should follow the abstract to aid indexing.
- 4 to 6 **highlights;** a short collection of bullet points that convey the core findings and provide readers with a quick textual overview of the article. These four to six bullet points should describe the essence of the research (e.g. results or conclusions) and highlight what is distinctive about it.
- An **Introduction** that should provide a review of recent literature and sufficient background information to allow the results of the article to be understood and evaluated.
- A **Methods** section detailing the theoretical or experimental methods used.
- An **Experimental section** that should provide details of the experimental set-up and the methods used to obtain the results.
- A **Results** section that should clearly and concisely present the data, using figures and tables where appropriate.
- A **Discussion** section that should describe the relationships and generalizations shown by the results and discuss the significance of the results, making comparisons with previously published work. (It may be appropriate to combine the Results and Discussion sections into a single section to improve clarity.)
- A **Conclusions** section that should present one or more conclusions drawn from the results and subsequent discussion and should not duplicate the Abstract.
- **Acknowledgement** (optional) of collaboration or preparation assistance may be included. Please note the source of funding for the research.
- **Nomenclature** (optional). Papers with many symbols should have a nomenclature that defines all symbols with units, inserted above the references. If one is used, it must contain all the symbols used in the manuscript and the definitions should not be repeated in the text. In all cases, identify the symbols used if they are not widely recognized in the profession. Define acronyms in the text, not in the nomenclature.
- **References** must be cited consecutively in the text using square brackets [1] and collected together in a reference list at the end of the manuscript.
- **Appendix(-icies)** if any.

SPECIAL NOTES

Units: The SI system of units for nomenclature, symbols and abbreviations should be followed closely. Symbols for physical quantities in the text should be written in italics (e.g. *v*, *T*, *n*, etc.). Symbols for units that consist of letters should be in plain text (e.g. ms^{-1}, K, min, mm, etc.). Please also see: http://physics.nist.gov/cuu/pdf/sp811.pdf .

Abbreviations should be spelt out in full on first appearance followed by the abbreviation in parentheses, e.g. variable time geometry (VTG). The meaning of symbols and units belonging to symbols should be explained in each case or cited in a **nomenclature** section at the end of the manuscript before the References.

Figures (figures, graphs, illustrations digital images, photographs) must be cited in consecutive numerical order in the text and referred to in both the text and the captions as Fig. 1, Fig. 2, etc. Figures should be prepared without borders and on white grounding and should be sent separately in their original formats. If a figure is composed of several parts, please mark each part with a), b), c), etc. and provide an explanation for each part in Figure caption. The caption should be self-explanatory. Letters and numbers should be readable (Arial or Times New Roman, min 6 pt with equal sizes and fonts in all figures). Graphics (submitted as supplementary files) may be exported in resolution good enough for printing (min. 300 dpi) in any common format, e.g. TIFF, BMP or JPG, PDF and should be named Fig1.jpg, Fig2.tif, etc. However, graphs and line drawings should be prepared as vector images, e.g. CDR, AI. Multi-curve graphs should have individual curves marked with a symbol or otherwise provide distinguishing differences using, for example, different thicknesses or dashing.

Tables should carry separate titles and must be numbered in consecutive numerical order in the text and referred to in both the text and the captions as Table 1, Table 2, etc. In addition to the physical quantities, such as *t* (in italics), the units [s] (normal text) should be added in square brackets. Tables should not duplicate data found elsewhere in the manuscript. Tables should be prepared using a table editor and not inserted as a graphic.

REFERENCES:

A reference list must be included using the following information as a guide. Only cited text references are to be included. Each reference is to be referred to in the text by a number enclosed in a square bracket (i.e. [3] or [2] to [4] for more references; do not combine more than 3 references, explain each). No reference to the author is necessary.

References must be numbered and ordered according to where they are first mentioned in the paper, not alphabetically. All references must be complete and accurate. Please add DOI code when available. Examples follow.

Journal Papers:

Surname 1, Initials, Surname 2, Initials (year). Title. Journal, volume, number, pages, DOI code.

[1] Hackenschmidt, R., Alber-Laukant, B., Rieg, F. (2010). Simulating nonlinear materials under centrifugal forces by using intelligent cross-linked simulations. *Strojniški vestnik - Journal of Mechanical Engineering,* vol. 57, no. 7-8, p. 531-538, DOI:10.5545/sv-jme.2011.013.

Journal titles should not be abbreviated. Note that journal title is set in italics.

Books:

Surname 1, Initials, Surname 2, Initials (year). Title. Publisher, place of publication.

[2] Groover, M.P. (2007). *Fundamentals of Modern Manufacturing*. John Wiley & Sons, Hoboken.

Note that the title of the book is italicized.

Chapters in Books:

Surname 1, Initials, Surname 2, Initials (year). Chapter title. Editor(s) of book, book title. Publisher, place of publication, pages.

[3] Carbone, G., Ceccarelli, M. (2005). Legged robotic systems. Kordić, V., Lazinica, A., Merdan, M. (Eds.), Cutting Edge Robotics. Pro literatur Verlag, Mammendorf, p. 553-576.

Proceedings Papers:

Surname 1, Initials, Surname 2, Initials (year). Paper title. Proceedings title, pages.

[4] Štefanić, N., Martinčević-Mikić, S., Tošanović, N. (2009). Applied lean system in process industry. *MOTSP Conference Proceedings*, p. 422-427.

Standards:

Standard-Code (year). Title. Organisation. Place.

[5] ISO/DIS 16000-6.2:2002. *Indoor Air – Part 6: Determination of Volatile Organic Compounds in Indoor and Chamber Air by Active Sampling on TENAX TA Sorbent, Thermal Desorption and Gas Chromatography using MSD/FID.* International Organization for Standardization. Geneva.

WWW pages:

Surname, Initials or Company name. Title, from http://address, date of access.

[6] Rockwell Automation. Arena, from *http://www.arenasimulation.com,* accessed on 2009-09-07.

EXTENDED ABSTRACT:

When the paper is accepted for publishing, the authors will be requested to send an **extended abstract** (approx. one A4 page or 3500 to 4000 characters). The instruction for composing the extended abstract are published on-line: http://www.sv-jme.eu/information-for-authors/ .

COPYRIGHT:

Authors submitting a manuscript do so on the understanding that the work has not been published before, is not being considered for publication elsewhere and has been read and approved by all authors. The submission of the manuscript by the authors means that the authors automatically agree to transfer copyright to SV-JME when the manuscript is accepted for publication. All accepted manuscripts must be accompanied by a Copyright Transfer Agreement, which should be sent to the editor. The work should be original work by the authors and not be published elsewhere in any language without the written consent of the publisher. The proof will be sent to the author showing the final layout of the article. Proof correction must be minimal and executed quickly. Thus it is essential that manuscripts are accurate when submitted. Authors can track the status of their accepted articles on http://en.sv-jme.eu/.

PUBLICATION FEE:

Authors will be asked to pay a publication fee for each article prior to the article appearing in the journal. However, this fee only needs to be paid after the article has been accepted for publishing. The fee is 380 EUR (for articles with maximum of 6 pages), 470 EUR (for articles with maximum of 10 pages), plus 50 EUR for each additional page. The additional cost for a color page is 90.00 EUR. These fees do not include tax.

Strojniški vestnik -Journal of Mechanical Engineering
Aškerčeva 6, 1000 Ljubljana, Slovenia,
e-mail: info@sv-jme.eu

9 770039 248001
ISSN 0039-2480

http://www.sv-jme.eu

Contents

Papers